

UCGE Reports  
Number 20211

Department of Geomatics Engineering

**Analysis of NGS CORS Network for GPS RTK  
Performance Using External NOAA Tropospheric  
Corrections Integrated with a Multiple  
Reference Station Approach**

(URL: <http://www.geomatics.ucalgary.ca/links/GradTheses.html>)

by

**Yong Won Ahn**

January 2005



UNIVERSITY OF  
CALGARY

THE UNIVERSITY OF CALGARY

Analysis of NGS CORS Network for GPS RTK Performance Using External NOAA  
Tropospheric Corrections Integrated with a Multiple Reference Station Approach

by

Yong Won Ahn

A THESIS

SUBMITTED TO THE FACULTY OF GRADUATE STUDIES  
IN PARTIAL FULFILLMENT OF THE REQUIREMENTS FOR THE  
DEGREE OF MASTER OF SCIENCE

DEPARTMENT OF GEOMATICS ENGINEERING

CALGARY, ALBERTA

JANUARY, 2005

© Yong Won Ahn 2005

## ABSTRACT

For high-accuracy GPS geodetic applications, the time-variable tropospheric propagation delay errors remain as a major factor limiting GPS RTK positioning accuracy. This thesis evaluates the additional improvement in position accuracy achieved by using the National Oceanic & Atmospheric Administration (NOAA) real-time tropospheric corrections within a multiple reference station network approach; this was compared with results from using a Modified Hopfield tropospheric model, for six scenarios in three geographical regions covered by the U.S. National Geodetic Survey (NGS) Continuous Reference Stations (CORS) network, for baseline lengths of 60~150km.

Testing was done on relatively humid days, and for each frequency (L1 & L2) and linear combination (wide-lane, ionospheric-free, geometry-free); the results demonstrated the effectiveness of the network approach in reducing the measurement errors for all observations. Overall test performances showed average 15% and 19% improvement, with the Modified Hopfield model, and with the NOAA corrections, respectively. The ionospheric-free linear combination, a measure of tropospheric and orbital errors, showed an additional 3% improvement with the NOAA corrections, relative to the Modified Hopfield model. This work also demonstrated using a ray-tracing technique along with the numerical weather model, to further improve the performance by 1%.

## ACKNOWLEDGEMENTS

I would like to express my gratitude to those who have had significant positive impact on my life over the past few years, as follows:

- To my lovely wife, Heeyun Yeom, who encouraged me whenever I faced many difficulties during my studies. I deeply appreciate all the support, encouragement, and love that were freely given to me, mostly from my wife, and also from my parents, Soonho Lee & Jongsu Ahn, and my mother-in-law, Soonkeum Moon as well as my brother, Dongwon, and my sisters. Needless to say, words cannot express the deep gratitude and thanks that I have for my lovely little daughter, Chaeyeon, who waited countless times for me to return home and play with her.
- To my supervisor, Dr. Gerard Lachapelle. Without his help, I may not have been able to effectively continue my research and studies. He gave me constant guidance, assistance, and support, during my graduate studies in the University of Calgary Geomatics Department
- To my co-supervisor, Dr. Susan Skone. Whenever I discussed with her about my research, she raised many very good questions, and constantly tried her best to encourage me, and guide me towards the right direction.

- To Dr. Kyle O’Keefe for providing materials and many advices and Dr. Richard Tay for spending his time in reading and commenting my thesis.
- To Dr. Seth Gutman and Dr. Susan Sahn, for their useful comments and advice. I would also like to thank the organizations that have provided the data used in this thesis: NGS and the NOAA/FSL. Special thanks are due to the NOAA/FSL, which I acknowledge for giving me invaluable guidance, and for providing the grid data sets to retrieve the necessary GPS corrections.
- To Dr. Elizabeth Cannon. I appreciate very much her efforts in reading through this thesis, and her useful feedback.
- To Dr. Paul Alves, for his very significant help, discussions, and concern about my research progress; and to Dr. Anna O. Jensen for giving me some very good ideas.
- To the Atmospheric Radiation Measurement (ARM) Program, sponsored by the U.S. Department of Energy (DOE), for providing the raw GRIB data.
- To Dr. Andre B. Fletcher, now at the Shanghai Astronomical Observatory (SHAO), for detailed help with proof-reading initial drafts of this thesis. Without his continuous encouragement and his immediate assistance, I may not have been able to finish this thesis on time.

- To Dr. Phi-Ho Park and Jong-Uk Park at GPS research group at Korea Astronomical Observatory in South Korea, for constant advices.
- To my colleagues throughout my graduate studies, especially: Wentao Zhang, Haitao Zhang, Salman Syed Qutub, Diep Thi Hong Dao, Eunhwan Shin, Minha Park, Bo Zheng, Nyunook Kim, Junjie Liu, Ping Lian, Oliver Julien, Sanjeet Singh, Oleg Mezentsev, Ning Liu, Lance de Groot, Natalya Nicholson, Ruben Yousuf, and Sudhir Man Shrestha, for interesting and useful discussions, and friendly advice and companionship.

Though I sincerely apologize to those whose names I must have inadvertently omitted from the above acknowledgements, I nevertheless hope that all concerned will enjoy bright futures and great successes in their lives.

## TABLE OF CONTENTS

	<b>Page</b>
APPROVAL PAGE .....	ii
ABSTRACT .....	iii
ACKNOWLEDGEMENTS .....	iv
TABLE OF CONTENTS .....	vii
LIST OF TABLES .....	x
LIST OF FIGURES .....	xii
LIST OF SYMBOLS .....	xv
LIST OF ABBREVIATIONS .....	xx
CHAPTER 1: INTRODUCTION .....	1
1.1 Background .....	1
1.2 Objectives .....	7
1.3 Thesis Outline .....	8
CHAPTER 2: GPS FUNDAMENTALS .....	11
2.1 GPS Observables and Measurement Equations .....	11
2.2 GPS Error Sources .....	18
2.2.1 Clock Errors .....	20
2.2.2 Orbit Errors .....	22
2.2.3 Ionospheric Errors .....	26
CHAPTER 3: GPS SIGNAL DELAY BY TROPOSPHERE .....	30
3.1 Introduction .....	30
3.2 Principles of GPS Signal Delay .....	31
3.3 Models for the Troposphere .....	39

3.3.1 Saastamoinen Model.....	39
3.3.2 Hopfield Model.....	42
3.3.3 Modified Hopfield Model.....	44
3.4 Mapping Functions.....	48
3.5 Ray-tracing.....	54
CHAPTER 4: THE MULTIPLE REFERENCE STATION APPROACH.....	59
4.1 Background.....	59
4.2 Network GPS RTK Approach.....	64
4.3 Limitations in the Multiple Reference Station Network Approach.....	66
CHAPTER 5: NOAA REAL-TIME TROPOSPHERIC CORRECTIONS.....	71
5.1 NOAA GPS-Met Network.....	71
5.2 NOAA RUC20 Numerical Weather Prediction Model.....	73
5.3 Retrieval of the NOAA Tropospheric Corrections.....	75
5.4 Comparison between the Modified Hopfield Model and NOAA Real-Time Tropospheric Corrections.....	80
CHAPTER 6: SCENARIOS AND DATA DESCRIPTION.....	82
6.1 NGS CORS Network.....	82
6.2 Description of Scenarios.....	85
6.2.1 Florida Region.....	86
6.2.2 North Carolina Region.....	88
6.2.3 North Eastern Region.....	91
6.3 Data Description.....	93
6.4 Processing Method.....	101
CHAPTER 7: PERFORMANCE ANALYSIS FOR EACH SCENARIO.....	112
7.1 Results of the Multiple Reference Station Network Approach using the NOAA Real- Time Tropospheric Corrections.....	115

7.1.1 Florida Region .....	117
7.1.2 North Carolina Region.....	133
7.1.3 North Eastern Region.....	138
7.2 Results of the Multiple Reference Station Approach using Ray-tracing.....	147
CHAPTER 8: CONCLUSIONS AND RECOMMENDATIONS.....	151
8.1 Conclusions.....	151
8.2 Recommendations.....	153
REFERENCES .....	155

## LIST OF TABLES

2.1	Accuracy of IGS Orbits (from IGS 2004) .....	24
3.1	The coefficients for Neill hydrostatic mapping function .....	53
3.2	The coefficients for Neill wet mapping function .....	53
5.1	Example of contents of a grid file (0407520.GRID, hourly data) .....	79
5.2	Example of retrieved values .....	80
6.1	Dates for the data in each network.....	100
6.2	RUC data availability (from ARM 2004).....	105
6.3	A GrADS script to extract the desired parameters from GRIB data into text format .....	107
6.4	Options used in MultiRef™, for each network, and each scenario .....	110
7.1	Percentage of improvement (%) relative to the single baseline approach by the modified Hopfield model for scenario FL1, 3 September 2003 .....	120
7.2	Percentage of improvement (%) relative to the single baseline approach by the modified Hopfield model for scenario FL1, 4 September 2003 .....	122
7.3	Statistics of the overall performance in the level of improvement (%) for scenario FL1, over the five days .....	124
7.4	The level of improvement (%) of scenario FL2, on September 3, 2003 .....	127
7.5	Percentage of improvement (%) relative to the single baseline approach by the modified Hopfield model for scenario FL2, 4 September 2003 .....	130
7.6	Statistics of the overall performance in the level of improvement (%) for scenario FL2, over the five days .....	132
7.7	Statistics of the overall performance in the level of improvement (%) for scenario NC1, over the five days .....	136
7.8	Statistics of the overall performance in the level of improvement (%) for scenario NC2, over the five days .....	138

7.9	Statistics of the overall performance in the level of improvement (%) for scenario NE1, over the six days .....	140
7.10	Statistics of the overall performance in the level of improvement (%) for scenario NE2, over the six days .....	142
7.11	Statistics of the overall performance in the level of improvement (%) of the observation domain results for all scenarios, for both the Modified Hopfield and the NOAA model .....	144
7.12	Overall performance in the level of improvement (%) in the ray-tracing test for scenario FL1 on 3 September 2003 with respect to the network approach by the NOAA model .....	150

## LIST OF FIGURES

2.1	Effect of GPS errors on baseline length .....	19
2.2	Effect of GPS errors on station height .....	20
2.3	Illustration of four different kinds of GPS orbit .....	23
2.4	IGS Tracking Network (from IGS 2004) .....	24
3.1	Geometry of the Modified Hopfield model .....	45
3.2	A ray-tracing scheme .....	56
4.1	Comparison of performance between the single baseline approach and a network RTK approach .....	64
4.2	Double difference misclosures of a single baseline before network corrections are applied .....	68
4.3	Double difference misclosures of multiple reference stations approach when network corrections are applied .....	68
4.4	Probability density function of double difference misclosures of multiple reference station network approach and uncorrected double difference misclosures .....	69
4.5	Double difference misclosures of multiple reference station network approach...	70
5.1	NOAA GPS-Met Network (from NOAA 2004) .....	72
5.2	A process diagram for the retrieval of the NOAA real-time tropospheric corrections (Gutman et al 2003) .....	78
5.3	Total slant delays from the Modified Hopfield model and NOAA model .....	81
6.1	NGS CORS network (from NGS 2004) .....	83
6.2	Network configuration for the first scenario (FL1). The ZEFR station is treated as a rover, and the data rate is 30 seconds.....	86
6.3	Network configuration for the second scenario (FL2). The ZEFR station is again treated as a rover, and the data rate is 30 seconds. The MCD1 station has been added to the FL1 scenario to form the new FL2 network.....	88

6.4	Network configuration for the third scenario (NC1). The RALR station is treated as a rover, and the data rate is 30 seconds .....	89
6.5	Network configuration for the fourth scenario (NC2). Instead of using RALR as the rover, the SNFD station is used as the rover in this scenario and data rate is 30 seconds .....	90
6.6	Network configuration for the fifth scenario (NE1). The GODE station is treated as a rover, and the data rate is 30 seconds. ....	92
6.7	Network configuration for the sixth scenario (NE2). The SOL1 station is treated as a rover, and the data rate is 30 seconds .....	93
6.8	Kp index for September 2, 3, 4, and 5, 2003 (from NOAA 2005) .....	95
6.9	Interactive NOAA real-time water vapor data interface (from NOAA 2001).....	96
6.10	IPW during the 2003 Summer in Florida retrieved by the interface.....	96
6.11	Pressure (hPa) during the 2003 Summer in Florida retrieved by the interface .....	97
6.12	Zenith wet delays during the 2003 Summer in Florida retrieved by the interface	98
6.13	IPW during the 2003 Summer, in the North Carolina region retrieved by the interface.....	99
6.14	Pressure during the 2003 Summer, in the North Carolina region retrieved by the interface.....	99
6.15	Zenith wet delay during the 2003 Summer, in the North Carolina region retrieved by the interface.....	100
6.16	Flow diagram for the performance comparison between the NOAA real-time tropospheric corrections, and the Modified Hopfield model. ....	103
6.17	Relative humidity of each pressure level, at the ZEFR station.....	108
7.1	Raw data DD misclosures.....	116
7.2	The DD misclosures of the data corrected by the NOAA model, when combined with the network approach.....	117
7.3	DD misclosures for FL1 scenario, 3 September 2003 .....	119
7.4	DD misclosures for FL1 scenario, 4 September 2003 .....	121
7.5	Levels of improvement in the observation domain results for scenario FL1, for five different observables, over 5 days in 2003 summer, and 2004 winter. ....	123

7.6	The RINEX SNR flag values for FL2 on 3 September 2003 .....	126
7.7	DD misclosures for FL2 scenario, 4 September 2003 .....	128
7.8	The RINEX SNR flag values for FL2 on 4 September 2003 .....	128
7.9	Retrieved NOAA zenith wet delay for 3 and 4 September 2003 in the Florida region .....	129
7.10	Levels of improvement in the observation domain results for scenario FL2, for five different observables, over 5 days in 2003 summer, and 2004 winter .....	131
7.11	Levels of improvement in the observation domain results for scenario NC1, for five different observables, over 5 days in 2003 summer, and 2004 winter .....	135
7.12	Kp index for 15~17 June 2003 (from NOAA 2005).....	136
7.13	Levels of improvement in the observation domain results for scenario NC2, for five different observables, over 5 days in 2003 summer, and 2004 winter .....	137
7.14	Levels of improvement in the observation domain results for scenario NE1, for four different cases and five different observables, over 6 days in 2003 summer and spring .....	139
7.15	Levels of improvements in the observation domain results for scenario NE2, for four different cases and five different observables, over the 6 days in 2003 summer and spring.....	141
7.16	Summary of the levels of overall improvement for all scenarios, when using the Modified Hopfield tropospheric model .....	143
7.17	Summary of the levels of overall improvement for all scenarios, when using the NOAA tropospheric model.....	143
7.18	Zenith delays for the two tropospheric models.....	145
7.19	Slant delays for the two tropospheric models.....	146
7.20	Refractivity and refractivity index for the ray-tracing at ZEFR location on 3 September 2003 .....	148
7.21	Slant wet delay of the ray-tracing at ZEFR location on 3 September 2003 .....	149

## LIST OF SYMBOLS

$\rho_r^s$	geometrical distance between satellite and receiver
$c$	speed of light in vacuum
$\delta t_r$	station clock correction due to receiver clocks errors
$\delta t_{r,sys}$	delays in receiver and its antenna
$\delta t^s$	satellite clock correction
$\delta t_{sys}^s$	delays in satellite and its antenna
$\delta \rho_{trp}$	tropospheric delay
$\delta \rho_{ion}$	ionospheric delay
$\delta \rho_{rel}$	relativistic corrections
$\delta \rho_{mul}$	multipath
$\lambda$	wavelength of the GPS signal (L1 or L2)
$N_r^s$	phase ambiguity
$\varepsilon_{err}$	measurement error
$\vec{r}_i^s(t^s)$	satellite position at emission time $t^s = t_r - \tau_r^s$ in inertial system
$\tau_r^s$	light travel time ( $\rho_r^s / c$ )
$\vec{r}_{r,i}(t_r)$	receiver position at reception time $t_r$ in inertial system
$\vec{r}_{r,e}(t_r)$	receiver position at time $t_r$ in Earth-fixed system
$\vec{R}(t_r)$	transformation matrix from Earth-fixed to inertial system
$\vec{X}$	coordinates (x) due to the polar motion
$\vec{Y}$	coordinates (y) due to the polar motion
$\vec{U}$	sidereal rotation matrix
$\Delta \varepsilon$	obliquity parameter
$\Delta \lambda$	longitude parameter

$\bar{N}$	nututation parameter
$\bar{r}_{i,0}^s$	position vector at the center of mass
$\delta r_{\text{ant}}^s$	satellite antenna phase center offset and variations
$a$	semi-major axis
$e$	eccentricity
$\Omega$	longitude of ascending node
$\omega$	argument of perigee
$t_p$	time of perigee passage
$\bar{r}_{r,e}(t_0)$	coordinates of the station
$\bar{v}_{r,e}$	velocities of the station,
$\delta \bar{r}_{r,\text{sol}}$	solid Earth tides
$\delta \bar{r}_{r,\text{pol}}$	pole tides
$\delta \bar{r}_{r,\text{ocn}}$	ocean loading
$\delta \bar{r}_{r,\text{atm}}$	atmospheric loading
$\delta \bar{r}_{r,\text{ant}}$	antenna phase center offset and variations.
$\dot{\rho}_r^s$	radial velocity of a GPS satellite
$\Delta r$	error of a baseline length $\ell$
$\Delta R$	orbit errors
$\varphi$	geodetic latitude
$\Phi_{\text{IF}}$	ionospheric-free linear combination
$f_1$	GPS L1 frequency
$f_2$	GPS L1 frequency
$\Phi_{L1}$	L1 carrier phase measurement
$\Phi_{L2}$	L1 carrier phase measurement
$S_{\text{ion}}^{2\text{nd}}$	error of the second order effects of the ionosphere
$\alpha_M$	geomagnetic azimuth

$\theta'_M$	pole distance
$\theta_M$	geomagnetic pole distance
$\varepsilon_M$	geomagnetic elevation angle
$L_e$	path length by the atmosphere
$n(s)$	index of refraction
$p_d$	partial pressure of dry air (mbar)
$p$	total pressure
$e$	partial pressure of water vapor (mbar)
$k_1, k_2, k_3$	refraction constants (K/mbar, K/mbar, K / mbar <sup>2</sup> )
$Z_d^{-1}$	inverse compressibility for dry air
$Z_w^{-1}$	inverse compressibility for wet air
$T_c$	temperature in degrees centigrade
$T$	temperature in Kelvin
$H_{rh}$	relative humidity in percentage
$H$	height above sea level
$N_{ds}$	surface dry refractivity given by Essen and Froome (1951)
$P_{ds}$	partial pressure for dry air at surface
$T_s$	surface temperature
$H_d^e$	effective height for the hydrostatic component
$N_{ws}$	surface wet refractivity given by Essen and Froome (1951)
$P_{ws}$	partial pressure for wet air at surface
$H_w^e$	effective height for the wet component (11000~12000 m)
$g$	normal gravity field
$r$	altitude from the Earth's center to the troposphere
$r_0$	altitude from the Earth's center to surface (or antenna)
$\beta$	temperature lapse rate

$T_s$	temperature at surface (or antenna) height
$R$	constant (universal gas constant divided by molar weight of dry air)
$M$	molar weight of dry air
$p_T$	pressure at the altitude of the tropopause
$T_T$	temperature of the tropopause
$h_T$	altitude of the tropopause
$z$	zenith angle
$R_E$	radius of the Earth
$h$	altitude
$h_w$	height of the wet part
$h_d$	height of the hydrostatic part
$r$	radius from the center of the Earth
$z_0$	zenith angle of the station
$z$	arbitrary zenith angle
$a$	mapping function coefficient
$t$	time (day of year)
$T_0$	day of year for “maximum winter”
$m_{niell}$	Niell mapping function
$ds_h$	hydrostatic slant delay
$ds_w$	wet slant delay
$\delta\mathbf{\bar{I}}$	vector of corrections (metres)
$C_{\delta I_r, \delta I}$	covariance matrix between the corrected and network observations,
$B$	double difference matrix
$C_{\delta I}$	variance-covariance matrix of the network observations
$\bar{\Phi}$	vector of the network observations (metres)
$\lambda\Delta\nabla N$	vector of the double difference ambiguities (metres)
$P_{sfc}$	surface pressure

$g(m)$	gravitational acceleration at the center of mass of the vertical atmospheric column directly above the station
$M_w$	specific gas constant of wet air
$M_d$	specific gas constant of dry air
$N_d$	refractivity of the hydrostatic component
$N_w$	refractivity of the wet component
$T_m$	mean temperature
$T_s$	surface temperature
$\rho$	total density
$\rho_w$	density of the wet component
$\rho_h$	density of the hydrostatic component
$\lambda$	wavelength for each L1 and L2 frequency

## LIST OF ABBREVIATIONS

ACARS	Aircraft Communications, Addressing, and Reporting System
ACs	Analysis Centers
Alt	Altimeter setting
ARM	Atmospheric Radiation Measurement
CONUS	Continental United States
CORS	Continuously Operating Reference Stations
DEM	Digital Elevation Model
DGPS	Differential GPS
DMI	Danish Meteorological Institute of
DOY	Day Of Year
Dst	Disturbed storm time
GOES	Geostationary Operational Environmental Satellite
GPS-Met	Ground-Based GPS Meteorology
GPS	Global Positioning System
GrADS	Grid Analysis and Display System
GRIB	Gridded Binary
HIRLAM-E	High Resolution Limited Areas Model – E
IERS	International Earth Rotation and Reference System Service
IGS	International GPS Service
IPW	Integrated Precipitable Water vapor
ITRF	International Terrestrial Reference Frame
NetCDF	Network Common Data Form
NGS	National Geodetic Survey
NOAA	National Oceanic and Atmospheric Administration
NOAA/FSL	National Oceanic and Atmospheric Administration's Forecast Systems Laboratory
NWP	Numerical Weather Prediction
NWS	National Weather Service

PDF	Probability Density Function
PRN	Pseudorandom Noise
RASS	Radio Acoustic Sounding System
RINEX	Receiver Independent Exchange
RMS	Root Mean Square
RTK	Real-Time Kinematic
RUC	Rapid Update Cycle
SED	Storm-Enhanced Density
SIPs	Stochastic Ionosphere Parameters
SHD	Slant Hydrostatic Delay
SLR	Satellite Laser Ranging
SNR	Signal to Noise Ratio
SP3	Standard Product #3 ASCII
SSM/I	Special Sensor Microwave Imager
STD	Slant Total Delay
SWD	Slant Wet Delay
TEC	Total Electron Content
TEC	Total Electron Content
TIDs	Traveling Ionospheric Disturbances
USCG	United States Coast Guard
VAD	Velocity-Azimuth Display
VLBI	Very Long Baseline Interferometry
VTEC	Vertical TEC
WGS84	World Geodetic Survey 84
WVR	Water Vapor Radiometer
Wx	Weather
ZHD	Zenith Hydrostatic Delay
ZTD	Zenith Total Delay
ZWD	Zenith Wet Delay

## **CHAPTER 1**

### **INTRODUCTION**

#### **1.1 Background**

The use of Global Positioning System (GPS) technology is expanding rapidly, and is playing an increasingly important role in many areas, including transportation, navigation, agriculture and geographical information systems as well as in the scientific community. GPS sensing is, especially, one of the most valuable tools in the atmospheric research community, because GPS provides relatively accurate atmospheric signal delays under all weather conditions. Since this sensing provides more information on the spatial distribution of the water vapor near the receiver, more accurate zenith hydrostatic and wet delays can be retrieved from individual reference stations, when combined with the results from the most advanced and accurate numerical weather prediction models. However, such applications also have a need for increasingly accurate, reliable, and timely GPS data and products from existing and specialized networks.

In order to get the most reliable GPS real-time kinematic (RTK) positioning results, many techniques for reducing or eliminating the inherent errors in GPS observables have been developed. One such method is the double differencing technique. When this differencing technique is implemented in GPS data processing, and used with the ionospheric-free

linear combination, it is possible to get one of the most accurate and reliable GPS solutions, whenever the ambiguities are correctly resolved. Using ionospheric-free linear combinations, the first-order effect of the ionospheric errors, which are the most prominent error sources in the GPS signals, can be eliminated. The satellite orbital errors are relatively small, and give us sufficiently accurate results when using a precise ephemeris. However, unlike the ionospheric and orbital errors, which can be reduced to sufficient levels, errors in the tropospheric delay can be the largest limiting factor for high accuracy in GPS positioning at the present time. These differential error terms, such as ionospheric, orbital, and tropospheric errors, are also spatially and temporally correlated (Fotopoulos & Cannon 2000). Since these three errors are spatially correlated, they are usually negligible for short baselines in differential carrier phase positioning. However, they are crucial limiting factors for long baselines. The greatest difficulty with these errors, in this case, is from the troposphere, as the highly variable tropospheric water vapor content makes it more difficult to obtain the desired accuracy, assuming that most of the prominent ionospheric errors are eliminated with using the ionospheric-free linear combination.

High-accuracy RTK positioning with GPS is one of the most widely used geodetic techniques today. Due to the effects of the ionosphere and troposphere, as well as of the satellite orbit uncertainties, the RTK solutions are easily corrupted by their decorrelation characteristics, especially when long baselines are used. The endless demand from users for higher accuracy and reliability drives the continuous improvement of accurate positioning techniques, such as a multiple reference station approach, etc. (Raquet 1998,

Luo 2001). During the period 1996-2000, the multiple reference approach, referred to as MultiRef™, was developed at the University of Calgary. In MultiRef™, the NetAdjust method, which uses an optimal linear minimum variance estimator to reduce the correlated code and/or carrier phase errors, is used (Alves 2004c). In addition, the software uses a network ambiguity resolution approach (see Sun et al 1999), and numerous real time components (see Townsend et al 1999).

Even if a multiple reference station approach is proven to eliminate the correlated errors, uncertainties such as moisture fields in the troposphere, which have a highly variable water content in both time and space, constitute the largest limiting factor, and corrupt the RTK corrections in high-accuracy GPS RTK positioning. Therefore, instead of using a standard atmospheric model in high-accuracy GPS, there is a strong demand for improved techniques to mitigate the troposphere delay, and currently this is one of the most important outstanding problems still to be solved. Although the tropospheric errors in GPS are the ultimate limiting factors, the measurement of the atmospheric delay of radio signals from navigation system satellites, such as GPS, also offers an opportunity for the Numerical Weather Prediction (NWP) community to obtain high-quality atmospheric moisture information from already established networks of GPS ground stations. If the surface pressure can be determined independently, e.g., from an NWP model, the delay of the GPS signals can provide information related to the atmospheric moisture content.

Since 2001, the Ground-Based GPS Meteorology (GPS-Met) branch of the National Oceanic and Atmospheric Administration's Forecast Systems Laboratory (NOAA/FSL) has tested real-time tropospheric corrections, and this has offered new opportunities to the GPS community. They have developed and assessed techniques to measure atmospheric water vapor, using ground-based GPS receivers, to make improved weather forecasts. These receivers can make accurate all-weather estimates of atmospheric refractivity at very low cost (Gutman & Benjamin 2001). The GPS-Met branch has been formed in response to the need for improved moisture observations to support weather forecasting, climate monitoring, and research. The primary goals of the branch are to demonstrate the major aspects of an operational GPS integrated precipitable water vapor (IPW) monitoring system, to facilitate assessments of the impact of these data on weather forecasts, to assist in the transition of these techniques to operational use, and to encourage the use of GPS meteorology for atmospheric research, and other applications (Gutman & Benjamin 2001).

By combining GPS data, radiosonde data, and other atmospheric measurements from a large network, GPS-Met is capable of accurately estimating the IPW at each GPS station. With knowledge of the IPW, the wet tropospheric delay can be computed accurately. The dry tropospheric delay can be computed based on barometer data, which is relatively easy to obtain. Thus, the total tropospheric delay can be computed. The GPS stations can then produce correction data, and transmit them to users, based on this computed tropospheric delay. The GPS-Met network currently has more than 300 GPS stations covering the continental United States (CONUS), Alaska, and Hawaii. It is expected that, once

operational in 2008, there will be a total of 1000 GPS stations covering North America. With augmentations from local government agencies and universities, the distance between the GPS stations can be as short as 50 km. It is expected that in 2010, the GPS-Met-generated atmospheric delay corrections will enable high-precision positioning and navigation (<20 cm) covering the entire CONUS (Gutman & Benjamin 2001).

A few studies, such as Pany et al (2001), Tsujii et al (2001), Behrend et al (2001), Jensen (2002), and Alves et al (2004a), introduced a NWP model as the tropospheric delay on GPS processing, such as the NOAA real-time tropospheric correction by the NOAA/FSL. Alves et al (2004a) evaluated the effectiveness of the multiple reference station approach, for users of the United States Coast Guard (USCG) network, in relation to the single-baseline RTK performance. In addition to the network approach, i.e. using multiple reference stations, real-time zenith tropospheric corrections supplied by the NOAA/FSL were used in this preliminary research. It was shown that these corrections assist with reducing the level of unmodeled, baseline-length-dependent errors, ultimately improving network and rover performance. The single reference station and network approaches were compared in terms of measurement error reduction and position accuracy, but in this case the NOAA tropospheric corrections were applied to the GPS measurements. The research evaluated methods that could be used to improve the current USCG network, by integrating the USCG network reference stations together into a network-based approach, and by applying external, NOAA atmospheric corrections.

In a similar approach, Jensen (2002) introduced NWP zenith delays for GPS data processing from the Danish Meteorological Institute of High Resolution Limited Areas Model - E (DMI HIRLAM-E) system. This system uses a 3D grid-point model derived from a rotated grid of latitude and longitude, with 0.15 deg in horizontal resolution, and 31 vertical levels, and it makes predictions every six hours up to an altitude of about 30 km. Jensen (2002) evaluated the expected accuracy of tropospheric zenith delays determined using the NWP model, the radiosonde, and the GPS, respectively, and independently applied the NWP tropospheric corrections to the Receiver Independent Exchange (RINEX) format data directly. In this case, Jensen used a linear interpolation to determine the delays every 15 seconds, calculated the slant delays for each of the satellite elevation angles, and subtracted these values from raw code and phase observations since the source code of the processing software was unavailable to her. However, there was a cycle slip detection problem when the raw data were manipulated, causing an increased level of falsely detected cycle slips for lower elevation angles (Jensen 2004). This work involved 10 stations in a network larger than 200 km when it is difficult to resolve ambiguities, with a total of six hours of data due to the limited access to the NWP.

This thesis expands on the previous research mentioned above, and describes some of the issues associated with the improvement of GPS RTK performance using the NOAA tropospheric corrections, rather than a standard tropospheric model, as a means for determining and improving real-time positioning accuracy. This thesis also addresses a potential improvement for lower elevation angles, using a ray-tracing technique.

## 1.2 Objectives

There are two major objectives in this thesis:

The first objective is to evaluate the impact of using real-time tropospheric corrections, which are generated by NOAA using the Rapid Update Cycle (RUC) 20 NWP model, on GPS RTK positioning. Three geographic regions, Florida, North Carolina, and the North Eastern regions in the National Geodetic Survey (NGS) Continuously Operating Reference Stations (CORS) network in the USA, are selected and evaluated for a maximum of three consecutive days for each season during the year. In addition, when it is relatively humid, data were carefully chosen based on the IPW, wet delay, pressure, and temperature calculated by NOAA. In total, this work involves 146 24-hour network data streams, in which the data rate was every 30 seconds; 16 stations are involved, and 3504 tropospheric corrections are to be retrieved. A prior study has been done in this area, relating to the reduction of marginal tropospheric errors by the NOAA real-time tropospheric model (Alves et al 2004a). However, the objective of this thesis is a more thorough investigation of the effect of these atmospheric characteristics on GPS RTK performance.

In order to investigate this, this research firstly evaluates the effectiveness of the multiple reference station approach for users of the NGS CORS network, in relation to the single-baseline RTK performance. This is achieved by using first the single-baseline approach, and then the network approach. In addition to the network approach, zenith real-time

tropospheric corrections from NOAA are used. These corrections assist with reducing the level of unmodeled, baseline-length-dependent errors, ultimately improving the network and rover performance. All the test results which cover the observation domain results are compared with that of a standard tropospheric model for GPS processing, i.e. the Modified Hopfield model, and with the NOAA real-time tropospheric model.

The second thesis objective is to assess and compare the results of ray-tracing techniques with respect to the network approach based on the NOAA model for the troposphere. This approach is only applied for satellite with elevation angles is below 10 degrees.

### **1.3 Thesis outline**

The next two chapters will present basic fundamentals relevant to this thesis. In Chapter 2, GPS theory, and the different error sources that affect GPS observations, will be discussed.

The principles of GPS signal delays in the troposphere, and some of the fundamental models for mitigating the tropospheric errors, will be described in Chapter 3. The mathematical background of the ray-tracing method used in this thesis will be introduced in the last section of this chapter.

Chapter 4 will describe the multiple reference stations approach. The algorithm used in this approach will be briefly described, as well as the comparison between the traditional

single-station and the network-based GPS RTK approach. Chapter 4 also addresses the limitations of the multiple reference station approach.

Chapter 5 will introduce some background information relevant to the NOAA real-time tropospheric corrections (NOAA model) used in this thesis. This chapter will include some details on the NOAA RUC20 numerical weather prediction models, and briefly describe how to retrieve the corrections.

Chapter 6 will define the scenarios selected for this research. There are six different scenarios for three geographical regions in the United States, and up to three consecutive days of the data sets which are relatively humid compared to the other days. The details of these data are given in this chapter.

Chapter 7 will discuss the performance analysis for each scenario defined previously. The temporal behavior of the errors, in addition to an analysis of the observation domain, will be given. Including various linear combinations such as the ionospheric-free linear combination, the wide-lane linear combination, and the geometry-free linear combination, a total of five performance measures will be given. All the analysis will be discussed, with an emphasis on the differences in the performance when reducing the errors with the multiple reference stations approach -- with or without the NOAA model -- instead of the Modified Hopfield model. This chapter will present investigations into the possibility of combining the NOAA model with ray-tracing techniques, when elevation angles lower than 10 degrees are used. Here, the ray integration will be performed using raw data

which are encoded in a GRIdded Binary (GRIB) format from the NOAA RUC20 NWP model.

Chapter 8 will give some conclusions of this research, and recommend possible avenues for future work in this area.

## **CHAPTER 2**

### **GPS FUNDAMENTALS**

This chapter addresses the GPS measurement equations, and describes some of the GPS error sources, including clock errors, orbit errors, and ionospheric errors. The tropospheric errors are described in Chapter 3.

#### **2.1 GPS Observables and Measurement Equations**

There are two basic types of GPS measurements: pseudoranges and carrier phase measurements which are biased ranges.

The pseudorange is a measure of the apparent propagation time from the satellite to the receiver antenna. This apparent propagation time is determined from the time shift required to align a replica of the GPS code generated in the receiver with the received GPS code. This time shift is the difference between the time of signal reception measured in the receiver time frame, and the time of emission measured in the satellite time frame.

The pseudorange is obtained by multiplying the apparent signal-propagation time by the speed of light, and differs from the actual range by the amount that the satellite and receiver clocks are offset, by propagation delays, and other errors including those in cables, electronics, etc. Since this measurement is not a true range measurement, it is referred to as the pseudorange (Wells et al 1987).

The carrier phase refers to an accumulated or integrated measurement, which consists of a fractional part, plus the integer number of wavelengths since signal lock-on. Since a GPS receiver cannot distinguish one cycle from another, the carrier phase measurement is ambiguous.

There is another GPS observable, called the Doppler measurement, which tracks the line of sight velocity between the satellite and antenna. Since Doppler measurements do not have an integer ambiguity, and are in the range of  $\pm 5$  kHz, this method is typically used to detect cycle slips in the carrier phase measurement, or to determine the GPS velocity in space.

Currently, GPS satellites transmit on the L1 and L2 frequencies. The L1 frequency is 1575.42 MHz, and L2 is 1227.60 MHz. Since the P code on the L2 frequency is encrypted, measurements are not directly available to civilian users, unless a special so-called 'code-less' technique is used. For this reason, the signal strength is decreased by 14 to 31 dB, and L2 measurements cannot be made with the same quality as those of the L1 frequency. However, if the new L5 frequency of 1176.45 MHz becomes available on satellites launched from 2005 onwards, the L2 signal will also be available to civilian users, and these will allow one to get more accurate dual-frequency measurements, which will be much more resistant to ionospheric errors. The main advantages that would arise from L5 availability may include: robustness, improved interference resistance, more power, improved data message quality, higher chipping rate, which would improve the multipath performance, and so on. For carrier-phase-based differential GPS (DGPS) users,

over long baselines, this modernization will further compensate for ionospheric errors, minimize the time required for ambiguity resolution and reacquisition, maximize the probability of correct ambiguity resolution over short time spans, etc., and help to achieve centimetre-level accuracies, or better, in the future.

The GPS observation equation for phase measurement, in units of metres between the receiver and satellite, can be written as follows in a general form (Rothacher & Beutler 2002):

$$\begin{aligned} \Phi_r^s = & \rho_r^s + c \cdot \delta t_r + c \cdot \delta t_{r,\text{sys}} - c \cdot \delta t^s - c \cdot \delta t_{\text{sys}}^s + \delta \rho_{\text{trp}} - \delta \rho_{\text{ion}} + \delta \rho_{\text{rel}} + \delta \rho_{\text{mul}} \\ & + \lambda \cdot N_r^s + \dots + \varepsilon_{\text{err}} \end{aligned} \quad (2.1)$$

where

$\rho_r^s$  : geometrical distance between satellite and receiver

$c$  : speed of light in vacuum

$\delta t_r$  : station clock correction

$\delta t_{r,\text{sys}}$  : delays in receiver and its antenna

$\delta t^s$  : satellite clock correction due to satellite clock error

$\delta t_{\text{sys}}^s$  : delays in satellite and its antenna

$\delta \rho_{\text{trp}}$  : tropospheric delay

$\delta \rho_{\text{ion}}$  : ionospheric delay

$\delta \rho_{\text{rel}}$  : relativistic corrections due to special and general relativity

$\delta\rho_{\text{mul}}$  : multipath

$\lambda$  : wavelength of the GPS signal (L1 or L2)

$N_r^s$  : phase ambiguity

$\varepsilon_{\text{err}}$  : measurement error

The corresponding observation equation for pseudoranges only differs in two ways. The ionospheric refraction correction  $\delta\rho_{\text{ion}}$  has the opposite sign for pseudoranges. The speed of the carrier wave (the "phase velocity") is actually increased, or "advanced", hence the phase refractive index is less than unity. However, the speed of the pseudorange is decreased (the so-called "group velocity"), and therefore the pseudo-range is considered "delayed", and hence the range (or group) refractive index is greater than unity (Hofmann-Wellenhof et al 1998). In addition, there is no ambiguity term  $\lambda \cdot N_r^s$  for pseudoranges.

In equation (2.1), the geometric distance term  $\rho_r^s$  can be written as follows (Rothacher & Beutler 2002):

$$\rho_r^s = |\vec{r}_i^s(t^s) - \vec{r}_{r,i}(t_r)| = |\vec{r}_i^s(t_r - \tau_r^s) - \vec{R}(t_r) \cdot \vec{r}_{r,e}(t_r)| \quad (2.2)$$

where

$\vec{r}_i^s(t^s)$  : satellite position at emission time  $t^s = t_r - \tau_r^s$  in inertial system  
(e.g. J2000.0)

$\tau_r^s = \rho_r^s / c$  : light travel time

$\vec{r}_{r,i}(t_r)$  : receiver position at reception time  $t_r$  in inertial system

$\vec{r}_{r,e}(t_r)$  : receiver position at time  $t_r$  in Earth-fixed system (e.g., International Earth Rotation and Reference System Service (IERS) International Terrestrial Reference Frame (ITRF)) with

$$\vec{r}_{r,i}(t_r) = \vec{R}(t_r) \cdot \vec{r}_{r,e}(t_r) \quad (2.3)$$

which refers the relation between inertial frame and Earth-fixed frame.

$\vec{R}(t_r)$  : transformation matrix from Earth-fixed to inertial system with

$$\vec{R}(t_r) = \vec{P}\vec{N}\vec{U}\vec{X}\vec{Y} \quad (2.4)$$

Equation (2.4) contains the Earth rotation parameters such as polar coordinates  $x_p$  and  $y_p$  in  $\vec{X}$  and  $\vec{Y}$  due to the polar motion, UT1-UTC in the sidereal rotation matrix  $\vec{U}$  and nutation parameter in obliquity  $\Delta\epsilon$  and longitude  $\Delta\lambda$  in  $\vec{N}$ . More details of the transformation matrix can be also found at Capellari (1976) or Leick (1995).

In an inertial reference frame, the satellite position  $\vec{r}_i^s(t^s)$  can be written as follows:

$$\vec{r}_i^s(t^s) = \vec{r}_{i,0}^s(t^s; a_{sat}, e_{sat}, i_{sat}, \Omega_{sat}, \omega_{sat}, t_p; p_1, p_2, p_3, \dots, p_d) + \delta r_{ant}^s(t^s) \quad (2.5)$$

where

$\vec{r}_{i,0}^s$  : position vector at the center of mass

$\delta r_{\text{ant}}^s$  : antenna phase center offset and variations

$a_{\text{sat}}, e_{\text{sat}}, i_{\text{sat}}, \Omega_{\text{sat}}, \omega_{\text{sat}}, t_p$  : six orbital elements

$p_1, p_2, p_3, \dots, p_d$  : gravity field coefficients, air drag and radiation pressure parameter, etc.

In equation (2.5), the semi-major axis  $a$  is used to define the size of the (elliptical or hyperbolic) orbit, and the eccentricity  $e$  defines the shape of this orbit. The inclination angle  $i$  is that between the  $z$ -axis and the angular momentum vector, which is perpendicular to the orbit plane. If  $i < 90$  deg, the orbital motion is counterclockwise when viewed from the north side of the fundamental plane (i.e. direct motion). If  $i > 90$  deg, the satellite is in retrograde motion. The longitude of the ascending node  $\Omega$  is the angle between the  $x$ -axis and a line from the dynamical centre to the point where the satellite crosses through the fundamental plane, from south to north, measured counterclockwise from 0 deg to 360 deg. If  $i = 0$  deg, then  $\Omega$  cannot be defined. The argument of the perigee  $\omega$  is the angle between the line of the ascending node and the line from the dynamical center to the perigee. If  $e = 0$ ,  $i = 0$  deg, the argument of perigee cannot be defined. The time of perigee passage  $t_p$  is normally used to relate position along the orbit to the elapsed time, by means of the Kepler equations. If  $e = 0$ ,  $t_p$  cannot be defined (Escobal 1976, Taff 1985, Capellari et al 1976, Montenbruck & Gill 2000).

In a similar way, the station position  $\bar{r}_{r,e}(t_r)$  can be written in Earth-fixed frame as follows:

$$\bar{\mathbf{r}}_{r,e}(t_r) = \bar{\mathbf{r}}_{r,e}(t_0) + \bar{\mathbf{v}}_{r,e} \cdot (t_r - t_0) + \delta\bar{\mathbf{r}}_{r,\text{sol}} + \delta\bar{\mathbf{r}}_{r,\text{pol}} + \delta\bar{\mathbf{r}}_{r,\text{ocn}} + \delta\bar{\mathbf{r}}_{r,\text{atm}} + \delta\bar{\mathbf{r}}_{r,\text{ant}} \quad (2.6)$$

where

$\bar{\mathbf{r}}_{r,e}(t_0)$  : coordinates of the station

$\bar{\mathbf{v}}_{r,e}$  : velocities of the station,

$\delta\bar{\mathbf{r}}_{r,\text{sol}}$  : solid Earth tides which are caused by the gravitational forces by Sun and Moon, and,

$\delta\bar{\mathbf{r}}_{r,\text{pol}}$  : pole tides which are caused by the reaction of the elastic Earth to the change of the rotation axis due to polar motion

$\delta\bar{\mathbf{r}}_{r,\text{ocn}}$  : ocean loading which is due to the weight of the water on the continental plate during high tide

$\delta\bar{\mathbf{r}}_{r,\text{atm}}$  : atmospheric loading which is due to the weight of the atmosphere on the continental plate

$\delta\bar{\mathbf{r}}_{r,\text{ant}}$  : antenna phase center offset and variations.

Since all these errors are combined together in the measurement, they should be modeled for applications requiring sub-centimetre precision in high-accuracy global reference or high-accuracy geodetic surveys.

Generally, the data processing procedure is as follows: the pseudorange or carrier phase measurements made simultaneously by two GPS receivers are combined so that, for any measurement epoch, the observations from one receiver to two satellites are subtracted

from each other to remove the receiver's clock error or bias. Then, the two single-differences are subtracted so as to eliminate the satellite clock errors, as well as to reduce significantly the effect of unmodeled atmospheric biases and orbit errors. The resulting set of double-differenced observables, which are independent combinations of two-satellite-two-receiver combinations, can be processed to solve for the baseline components, and, in the case of ambiguous carrier phase measurements, for the integer ambiguity parameters. All high-precision positioning techniques use some form of double-difference processing: pseudorange, unambiguous carrier phase after the double-differenced ambiguity values have been estimated and applied to the original carrier measurements, or ambiguous carrier phase data.

## **2.2 GPS Error Sources**

The carrier phase measurements and pseudoranges are affected by the systematic and random errors previously mentioned in Section 2.1. Again, there are many sources of systematic errors, such as: satellite orbits, clocks, the propagation medium, receiver clocks, relativistic effects, antenna phase center variations, etc. However, using the double difference technique, most of these systematic errors can be eliminated or reduced. For high-accuracy GPS RTK positioning, the double difference technique is a common approach for dramatically reducing the error in GPS-derived positions.

When looking at GPS error sources, two classes of biases are found: those mainly influencing the height, and those influencing the scale, of a baseline or a network, in

terms of precision positioning (Rothacher & Beutler 2002). The effect on baseline length can occur due to a bias in the absolute tropospheric delay, to neglecting the ionospheric delay, or to incorrect heights of fixed reference stations, etc.

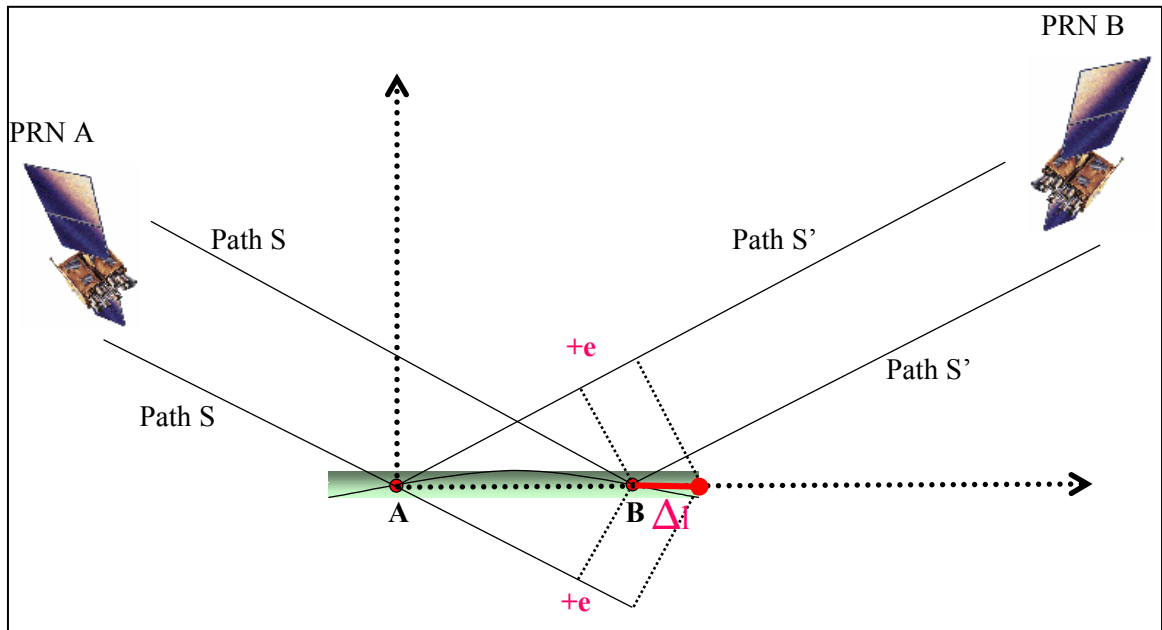


Figure 2.1: Effect of GPS errors on baseline length

For example, if there is a bias in the absolute tropospheric delay, the baseline length can be affected by an amount of the same magnitude as  $e$  as shown in Figure 2.1, for the signals transmitted on Pseudorandom Noise (PRN) A and PRN B satellite. Consequently, this error can be reflected in the baseline length.

However, the second class of GPS errors can affect the relative station heights. This can occur due to a different bias at each endpoint of a baseline. Such cases happen when there is a bias in the relative tropospheric delay, in the horizontal positions for fixed reference

stations, in the satellite orbit, in the antenna phase center differences, and in the multipath, etc.

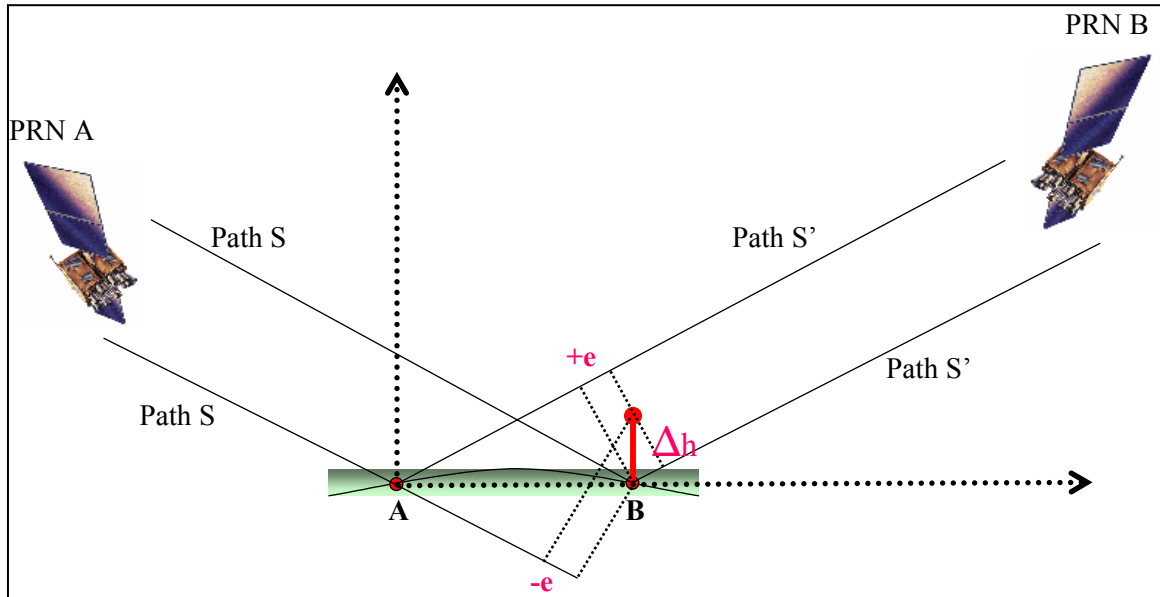


Figure 2.2: Effect of GPS errors on station height

Similarly, if there is a bias in relative tropospheric delay, it can have an effect of the same magnitude, but in a different direction, on the signals transmitted on PRN A and PRN B. Consequently, this error can be reflected in the station height, as shown in Figure 2.2.

### 2.2.1 Clock Errors

Let  $c \cdot \delta_r \equiv c \cdot \delta t_r + c \cdot \delta t_{r,\text{sys}}$  in Equation 2.1 so that  $\delta_r = \delta t_r + \delta t_{r,\text{sys}}$  which is the error of the receiver clock at time  $t$  with respect to GPS time. Similarly,  $\delta^i = \delta t^s + \delta t_{\text{sys}}^s$  is for the satellite. If so, the signal reception time can be written as  $t = t_r - \delta_r$  where  $t$  is the signal

reception time and  $t_r$  is the reading of the receiver clock at the signal reception time. The term,  $c \cdot \delta_r - c \cdot \delta^i$  or  $c \cdot \delta t_r + c \cdot \delta t_{r,\text{sys}} - c \cdot \delta t^s - c \cdot \delta t_{\text{sys}}^s$  in Equation 2.1, can be eliminated by implementing the double difference of the measurements.

However, this does not mean that the receiver clock error  $\delta_r$  is completely eliminated in the differencing technique. In order to compute the geometric distance  $\rho_r^s$  between the satellite and the receiver at time  $t$ , we still need to linearize the measurements correctly, so the receiver clock error  $\delta_r$  must be known in order to correct the reading of the receiver clock  $t_r$ . Now, the geometric distance  $\rho_r^s$  can be written in a simpler way, and its derivative can be obtained as follows:

$$\rho_r^s(t) = \rho_r^s(t_r - \delta_r) \quad \text{or} \quad d\rho_r^s(t) = -\dot{\rho}_r^s d\delta_r \quad (2.7)$$

where  $\dot{\rho}_r^s$  can be interpreted as the radial velocity of a GPS satellite with respect to the receiver. Obviously, this radial velocity can be minimized when the satellite just passes the zenith direction; however, the velocity can reach up to 900 m/s (~10 deg. elevation angle) at the near horizon (Hugentobler et al 2001).

Hugentobler et al (2001) mentioned that if the  $|d\delta_r|$  is smaller than 1  $\mu\text{s}$ , the error  $|d\rho_r^s(t)|$  due to the  $|-d\delta_r|$ , which can be interpreted as the receiver clock synchronization error, can be as small as 1 mm.

### 2.2.2 Orbit Errors

Figure 2.3 roughly illustrates four different kinds of GPS orbits. In this figure, the dashed line represents the two-body Kepler orbit, which is a perturbation-free orbit; the green line is the actual orbit, and the blue line is IGS predicted final orbit. The broadcast orbit represented by the red line in Figure 2.3 is based on pseudoranges, which have uncertainties of 3 m, while the final precise orbit is based on phase observables that have uncertainties of 0.05 m. For the broadcast orbit, the latency of the broadcast orbit is two hours, which means that the satellite moves about 30,000 km during this time. Therefore, the predicted orbit based on the broadcast coefficients can be very different from the actual orbit. However, the orbit errors are spatially correlated, so that we can eliminate most of them using differential techniques for low precision applications. Especially for long baselines, the orbital residual error can be important.

Currently, there are three different types of precise orbit products produced by the International GPS Service (IGS), which are generated based on estimates of orbits at seven different IGS analysis centres (ACs), with individual weights used in a sum, to get a weighted combination, resulting in: the ultra-rapid, rapid, and final orbit products. The seven different ACs use six different software packages which are all batch-type processor, not real-time kinematic purpose: GIPSY-OASIS, Bernese GPS S/W, GAMIT, etc., and apply different strategies, parameterizations, and models.

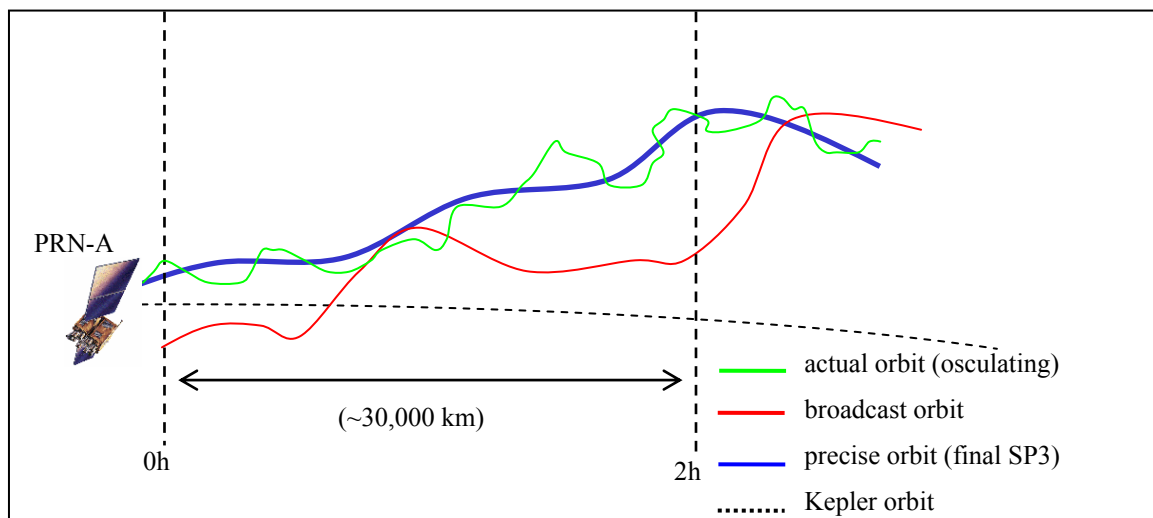


Figure 2.3: Illustration of four different kinds of GPS orbit

The Root Mean Square (RMS) of the combined solution, a good indicator for the consistency in the quality of the orbits, is about 3 cm with respect to the best centres, and the IGS orbits agree well with the SLR measurements, except for a radial offset between the two systems, of approximately 5 cm, which cannot be explained yet (Rothacher & Beutler 2002). Table 2.1 shows each of the orbit qualities.

These are based on phase measurements using the data from a global GPS network, and the orbit information is available in the Standard Product #3 ASCII (SP3) format, which is a geocentric earth-fixed satellite position in ITRF, reported at intervals of every 15 minutes.

Table 2.1: Accuracy of IGS Orbits (from IGS 2004)

IGS Precise Orbit Product		Latency	Orbit accuracy	Satellite clocks and/or stations
Ultra-Rapid	predicted	real-time	~10 cm	~ 5 ns
	observed	3 hours	< 5 cm	~ 0.2 ns
Rapid		17 hours	< 5 cm	0.1 ns
Final		~ 13 days	< 5 cm	< 0.1 ns

Figure 2.4 illustrates the distribution of the global GPS network. The ITRF coordinates are positioned relative to the geo-centre using a variety of space geodetic techniques, such as Satellite Laser Ranging (SLR), Very Long Baseline Interferometry (VLBI), and GPS. Therefore, ITRF is considered to be a more reliable datum than World Geodetic System 84 (WGS84), and their difference is approximately 10 cm.

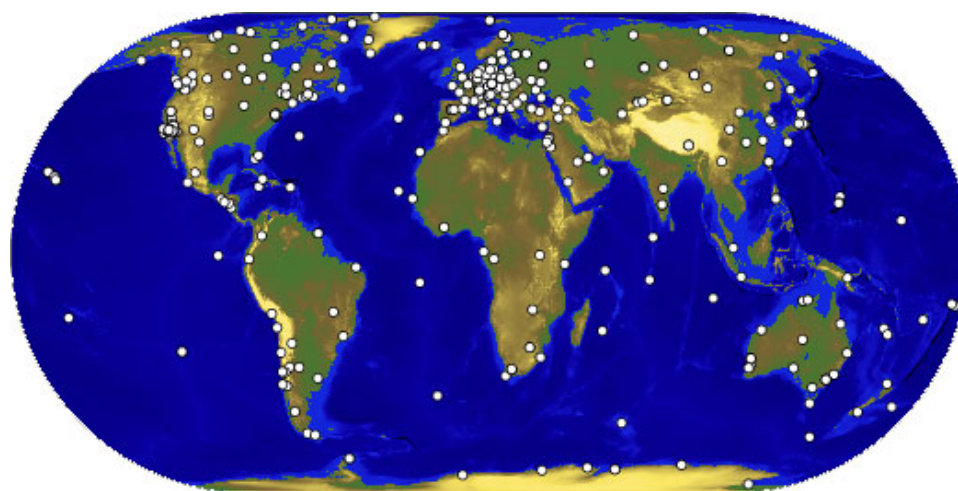


Figure 2.4: IGS Tracking Network (from IGS 2004)

With respect to the influence of the orbit errors on station coordinates, for different baseline lengths, Bauserisma (1983) estimates and quantifies the baseline errors as a function of orbit errors, as follows:

$$|\Delta r| = \frac{\ell}{\rho} \cdot |\Delta R| \approx \frac{\ell(\text{km})}{25,000\text{km}} \cdot |\Delta R| \quad (2.8)$$

where

$\Delta r$  : error of a baseline length  $\ell$

$\Delta R$  : orbit errors

Equation 2.8 means that broadcast orbits may be sufficient to achieve an accuracy of 1 mm in the baseline, for a 10 km baseline length. Due to the unexpectedly high orbit quality provided by the IGS, orbit errors are usually ignored in the post-processing. However, this does not mean that this quality is sufficiently good for all applications, such as GPS RTK positioning for long baselines, or for use by the atmospheric community.

Especially in the case of retrieving the IPW, or slant wet delay of the troposphere, Rocken et al (1997), Dousa (2001), and Kruse et al (1999) address the importance of the orbit quality, since accurate near-real-time GPS IPW estimation depends on the accuracy of the satellite orbits. Baltink et al (2002), Rocken et al (1997), and Kruse et al (1999) tested whether orbit relaxation, i.e., the simultaneous adjustment of orbit parameters during the processing of GPS data, could increase the accuracy of the IPW estimates.

They compared their results by orbit relaxation to the IPW estimates based on the final IGS orbits, and found an improvement of 20% in the RMS error, compared with other methods which use the quality index to remove bad satellites, or wrongly predicted satellites. However, Baltink et al (2002) suggested that an orbit improvement procedure, using an ultra-rapid orbit, would still be necessary for securing better IPW estimates.

### **2.2.3 Ionospheric Errors**

The effect of the dispersive ionosphere on GPS signals still remains as the major contributor in the GPS error budget. The ionosphere consists of ionized particles associated with free electrons, which delay the signals coming from space, and it extends from about 60 km to beyond 1000 km (Klobuchar 1996). This delay can be modeled by estimating the Total Electron Content (TEC) in a column of the atmosphere, or else eliminated as a first order effect, based on its dispersive characteristic, by using dual frequency measurements. Ionospheric disturbances mainly show up close to the equator, due to the high TEC there, and over the Polar Regions, due to short-term variations. The ionosphere is, however, quiet in mid-latitude regions, except in areas where Traveling Ionospheric Disturbances (TIDs) and storm enhanced density (SED) exist. In addition, there are ionospheric storms, with enormous variations, which are correlated with solar flares.

Due to the dispersive nature of the ionosphere, i.e. the frequency dependence of the signal delays, two different indexes of refraction can be derived: the phase refractive

index, and the group refractive index. Using the L1 and L2 phase measurements, it is possible to derive the ionospheric-free ('IF') linear combination, which can be used to eliminate the first order ionospheric effects, as follows:

$$\Phi_{\text{IF}} = \frac{f_1^2}{f_1^2 - f_2^2} \Phi_{\text{L1}} - \frac{f_2^2}{f_1^2 - f_2^2} \Phi_{\text{L2}} \quad (\text{metres}) \quad (2.9)$$

However, the IF linear combination cannot completely remove the ionospheric errors, as it neglects the higher-order terms which remain in the series expansion of the refractive index, which represent the effect of the geomagnetic field, and the bending effect of the wave paths. Bassari & Hajj (1993) developed an approximate method to describe these effects, for average conditions, and showed that the level of the error of the second order effects  $S_{\text{ion}}^{2\text{nd}}$  is in the range of 1 cm, with a maximum of less than 3 cm, using the IF combination.

$$S_{\text{ion}}^{2\text{nd}} \cong \left( 1.377 \times 10^{-6} \varphi \frac{r_E}{r_E + h_{\text{ion}}} \right)^3 \left| \sin \theta'_M \cos \varepsilon_M \cos \alpha_M - 2 \cos \theta'_M \sin \varepsilon_M \right| \\ \times m_{\text{ion}}(z_{\text{IP}}^i) \text{VTEC} \quad (2.10)$$

$$\theta'_M \approx \theta_M - \frac{h_{\text{ion}} \cos \alpha_M}{r_E \tan \varepsilon_M}$$

where

$\varphi$  : geodetic latitude

$\alpha_M$  : geomagnetic azimuth

$\theta'_M$  : pole distance

$\theta_M$  : geomagnetic pole distance

$\varepsilon_M$  : geomagnetic elevation angle

VTEC : vertical TEC

Although the IF combination eliminates the ionospheric effects to a considerable degree, this does not mean that this combination can give us the best solution for all networks. For example, in a small network, even if the combination reduces the ionospheric errors, the noise of the combination is almost three times higher, resulting in accuracies that are three times worse for the stations' coordinates. This is one of the limitations in using this combination in a small network.

Except in the case of IF linear combination, ionospheric refraction represents the largest of the error sources for all other linear combinations, including: wide-lane, narrow-lane, geometry-free, and Melbourne-Wubben (see Hugentobler 2001), as well as for the original L1 and L2 measurements. In differential positioning, the ionosphere can cause delays in excess of 20 ppm, in the code measurements, and also the signals may be advanced by about the same amounts, in the phase measurements. Therefore, the code minus phase measurement is a good indicator in estimating the ionospheric effects.

Since the ionosphere changes very fast, especially during scintillation at high or low latitudes, and trough phenomena below the auroral oval, which has 10~15 ppm gradients at 35~45 deg latitudes, to storm-enhanced density (SED) generated when the plasma goes

into the sub-auroral region, which has up to 75 ppm gradients (Skone 2003), it would be better to estimate these ionospheric effects using stochastic ionosphere parameters (SIPs). Unlike the deterministic component of the ionosphere, which may be modeled by mathematical functions, the stochastic part of the TEC represents the residuals of the modeling that are due to the magnitude of short term fluctuations in the TEC. Using fixed double difference ambiguities, these SIPs for the ionosphere can be computed at the double difference level, either by analyzing the L1-L2 linear combinations, or by simultaneously analyzing the original L1 and L2 measurements (Schaer 1999). The main procedure for the stochastic ionospheric estimation is that, at the beginning, the L1 and L2 observations are processed simultaneously, and for each satellite and each epoch, one ionosphere parameter is set up, and then the ionosphere parameters are constrained with a priori weights, or a process noise in a filter. Stochastic ionosphere modeling and parameterization is necessary in many cases, because short-period variations cannot be taken into account in global, regional, or even local ionosphere models (Hugentobler et al. 2001). In addition, Skone (1998) showed that the temporal stability of the ionospheric error was degraded under active ionospheric conditions.

The data used in this research, however, are carefully chosen based on the Kp index, which is an indicator of storm activity using 13 sub-auroral stations distributed around the world. Most of the data in this research does not have Kp values exceeding 5, which means relatively quiet to moderate ionospheric activity. This is an important selection step to make, as any decrease in accuracy from using NOAA tropospheric corrections would be masked by the much larger effects from the variable ionospheric conditions.

## CHAPTER 3

### GPS SIGNAL DELAY BY THE TROPOSPHERE

#### 3.1 Introduction

The troposphere is part of the neutral atmosphere, ranging from sea level to a height of about 12 km. The tropopause is a small boundary region between 12 km and 16 km where the temperature remains approximately constant at a level of -60 to -80 °C (Schuler 2001). The upper part above the tropopause is referred to as the stratosphere, up to an altitude of 40 km with a slow temperature increase. In GPS, the “troposphere” generally refers to the neutral atmosphere at altitudes 0 to 40 km (Skone 2003). For GPS signal frequencies, the troposphere is a non-dispersive medium (i.e., no frequency dependence in signal transmissions), and hence it affects the L1 and L2 signals by the same amount, unlike the effect of the ionosphere.

The tropospheric effect on GPS signals can be divided into two different components: the hydrostatic part, and the wet part. The hydrostatic and wet refractivity of the troposphere cause delays in the signals. Most of the total delay is due to the hydrostatic component, while the wet component is responsible for approximately 10% of the total delay. Various tropospheric delay models have been developed to estimate these delays, as a function of the satellite elevation angle, receiver height, and meteorological parameters, such as temperature, pressure, and humidity. The range delay in the zenith direction is

approximately 2.5m which corresponds to about 8 ns; however, for an elevation of 5 degrees, it increases to about 25 meters. This dependence on elevation angle is described by a mapping function, so that the delay near the horizon is three to five times higher than in the zenith direction. Most of the delay is mitigated in differential positioning; however the residual tropospheric delay increases as the baseline length increases.

Unlike the ionospheric errors and orbital errors, which can be reduced to sufficiently low manageable levels, errors in the tropospheric delay, which mostly contribute to errors in the height component in the station's coordinate estimates, are known to be one of the largest limiting factors for high accuracy GPS positioning, at the current time.

### 3.2 Principles of GPS Signal Delay

The neutral atmosphere can be divided into the actual troposphere, the tropopause and the stratosphere. The tropospheric delay of GPS signals depends on the index of refraction  $n$  along the signal path. For radio waves up to 15 GHz propagating through the atmosphere along a path  $s$ , the length  $L_e$  of the signal path can be calculated by Fermat's principle:

$$L_e = \int_{\text{path}} n(s) ds \quad (3.1)$$

where

$n(s)$  : index of refraction as function of the distance  $s$

The geometrical distance is different from the actual path due to the difference between the path delays in the troposphere versus a vacuum, and in reality is given as follows:

$$\delta\rho_{\text{tp}} = \int_{\text{path}} n(s)ds - \int_{\text{vacuum}} ds = \int_{\text{path}} (n(s) - 1)ds + \text{bending effect} \quad (3.2)$$

which is also called total or neutral slant path delay (Schuler 2001).

For elevations above 15 degrees, the bending effect is less than 1 cm; however, for smaller elevations, the effect can be as larger as 2-3 cm. This total delay can be divided into a hydrostatic component ( $\delta\rho_h$ ) and a wet component ( $\delta\rho_w$ ) as follows:

$$\delta\rho_{\text{tp}} = \delta\rho_h + \delta\rho_w \quad (3.3)$$

However, this can be expanded to further distinguish between the azimuthally symmetric delay and asymmetric parts (Schuler 2001).

$$\delta\rho_{\text{tp}} = \delta\rho_{h,\text{sym}} + \delta\rho_{h,\text{asym}} + \delta\rho_{w,\text{sym}} + \delta\rho_{w,\text{asym}} \quad (3.4)$$

where

$\delta\rho_{h,\text{sym}}$  : hydrostatic delay term under the assumption of symmetry in azimuth

$\delta\rho_{w,\text{sym}}$  : wet delay term under the assumption of symmetry in azimuth

$\delta\rho_{h,\text{asym}}$  : hydrostatic correction term taking asymmetry into account

$\delta\rho_{w,\text{asym}}$  : wet correction term taking asymmetry into account

Equation (3.4) can be further expanded when the horizontal tropospheric gradient model is applied to the above asymmetric components as follows:

$$\delta\rho_{\text{tp}} = m(\varepsilon)_h \cdot \text{ZHD} + m(\varepsilon)_w \cdot \text{ZWD} + m(\varepsilon)_{\text{azi}} \cdot [\text{G}_{\text{north}} \cdot \cos \alpha + \text{G}_{\text{east}} \cdot \sin \alpha] \quad (3.5)$$

where

$m(\varepsilon)$  : mapping function

ZHD : zenith hydrostatic delay

ZWD : zenith wet delay

$\text{G}_{\text{north}}$  : gradient in northward direction

$\text{G}_{\text{east}}$  : gradient in eastward direction

$\alpha$  : azimuth

h, w : subscript for hydrostatic or wet component

The practical type of the tropospheric delay model is the one without the gradient components. The zenith delay model as well as the mapping function is further defined in section 3.3.

In Equation (3.1), the index of the refractivity, ratio of the speed of the propagation of electromagnetic wave in vacuum to the speed of the propagation of the medium, can be expressed in term of the refractivity N as follows:

$$N=10^6(n-1) \quad (3.6)$$

The refractivity of humid air in the frequency band between 100 MHz and 20 GHz is given by (Thayer 1974) as follows:

$$N = k_1 \frac{p_d}{T} Z_d^{-1} + k_2 \frac{e}{T} Z_w^{-1} + k_3 \frac{e}{T^2} Z_w^{-1} \quad (3.7)$$

where

$p_d$  : partial pressure of dry air (mbar);  $p_d = p - e$  with  $p$  being the total pressure

$e$  : partial pressure of water vapor (mbar)

$T$  : temperature (K)

$k_1, k_2, k_3$  : refraction constants (K/mbar, K/mbar, K/mbar<sup>2</sup>)

$Z_d^{-1}, Z_w^{-1}$  : inverse compressibility factors for dry and wet air which are empirical factors

Atmospheric refractivity relies on pressure and compressibility of the gases, but also depends on the electric properties of the molecules. The molecules act like tiny dipoles and cause a dipole moment affecting the radio wave. In case of O<sub>2</sub> or N<sub>2</sub>, there exists only an induced dipole moment, but there is a permanent dipole moment in water vapor.

The first term in Equation (3.7) is the hydrostatic component and represents the effect of the induced dipole moment of the dry component, while the second term is related to the dipole moment of water vapor and the last term represents the dipole orientation effects

of the permanent dipole moment of water vapor molecules. The last two terms in Equation (3.7) constitutes to the wet component of the refractivity. The refraction constants  $k_1, k_2, k_3$  are determined empirically. The inverse compressibility accounts for the difference between ideal gas assumptions and non-ideal gas behavior. These values, and the pressure of water vapor, are given by (Schuler 2001, Thayer 1974, Hugentobler et al 2001):

$$\begin{aligned}
 Z_d^{-1} &= 1 + p_d \cdot \left( 57.97 \cdot 10^{-8} \cdot \left( 1 + \frac{0.52}{T} \right) - 9.4611 \cdot 10^{-4} \cdot \frac{T_c}{T^2} \right) \\
 Z_w^{-1} &= 1 + 1650 \frac{e}{T^3} \cdot \left( 1 - 0.01317T_c + 1.75 \cdot 10^{-4} T_c^2 + 1.44 \cdot 10^{-6} T_c^3 \right) \\
 e &= \frac{H_{th}}{100} e^{-37.2465 + 0.213166T - 0.000256908T^2}
 \end{aligned} \tag{3.8}$$

where

$T_c$  : temperature in ( $^{\circ}$  C)

$T$  : temperature (K)

$H_{th}$  : relative humidity (%)

These inverse compressibility factors, i.e.  $Z_d^{-1}$  and  $Z_w^{-1}$ , for dry and wet air are empirical factors and can be modeled as a function of pressure and temperature as shown in Equation (3.8).

In order to define the zenith delay, it is necessary to express the refractivity in Equation (3.7) in terms of its hydrostatic and wet components. With the assumption of the hydrostatic equilibrium, the following relationship can be made:

$$k_1 \frac{p_d}{T} Z_d^{-1} = k_1 \frac{\rho_d R_d T Z_d}{T} Z_d^{-1} = k_1 \rho_d R_d = k_1 \frac{\rho_d R_o}{M_d} = k_1 \left( \frac{\rho R_o}{M_d} - \frac{e}{T} Z_w^{-1} \frac{M_w}{M_d} \right) \quad (3.9)$$

where

$R_o$  : universal gas constant ( $\text{J mol}^{-1} \text{K}^{-1}$ )

$R_d$  : specific gas constant for dry air

$M_w$  : molar weight of wet air ( $\text{kg kmol}^{-1}$ )

$M_d$  : molar weight of dry air ( $\text{kg kmol}^{-1}$ )

$\rho_d$  : density of dry air ( $\text{kg m}^{-3}$ )

$\rho$  : total density for dry and wet air ( $\text{kg m}^{-3}$ )

Substituting Equation (3.9) into Equation (3.7), the refractivity can be rewritten as follows:

$$N = k_1 \left( \frac{\rho R_o}{M_d} - \frac{e}{T} Z_w^{-1} \frac{M_w}{M_d} \right) + k_2 \frac{e}{T} Z_w^{-1} + k_3 \frac{e}{T^2} Z_w^{-1} = k_1 \frac{\rho R_o}{M_d} + k_2' \frac{e}{T} Z_w^{-1} + k_3 \frac{e}{T^2} Z_w^{-1} \quad (3.10)$$

and

$$k'_2 = \left( k_2 - k_1 \frac{M_w}{M_d} \right) \quad (3.11)$$

where

$$k_2 = 70.4 \pm 2.2 \text{ K / hPa}$$

$$k_1 = 77.6 \pm 0.05 \text{ K / hPa}$$

$$k_3 = (3.739 \pm 0.02) 10^5 \text{ K}^2 / \text{hPa}$$

Equation (3.10) is useful, as it allows a strict separation between the hydrostatic and wet components. The hydrostatic component, from Equation (3.10), is

$$N_d = k_1 \frac{\rho R_o}{M_d} \quad (3.12)$$

and the wet component is

$$N_w = \left( k'_2 \frac{e}{T} + k_3 \frac{e}{T^2} \right) Z_w^{-1} \quad (3.13)$$

The zenith hydrostatic delay and the zenith wet delay can be defined as follows:

$$\text{ZHD} = 10^{-6} \int_{h_s}^{\infty} N_d dh \quad (3.14)$$

$$\text{ZWD} = 10^{-6} \int_{h_s}^{\infty} N_w dh \quad (3.15)$$

where

$h_s$  : surface height

$dh$  : differential increment in height

Almost 90% of the total delay occurs in the hydrostatic part, which varies slowly with time. This hydrostatic delay can be easily modeled by the assumption of hydrostatic equilibrium with an accuracy of the millimetre level (Mendes & Langley 1995). However, unlike the hydrostatic part, the wet part, which amounts to approximately 10-40 cm of range delay, is much more difficult to model than the hydrostatic part, due to its strong spatial and temporal variations. The assumption of hydrostatic equilibrium does not hold for this portion of the air and relative errors of empirical/theoretical models are on the order of 10%. This uncertainty in the modeling (which leaves large residual errors) can cause significant errors in high-precision GPS RTK applications. Since these variations can generate relative and absolute tropospheric errors, the error in the estimation of tropospheric corrections for one station with respect to another in a network can cause relative tropospheric errors, which mostly results in incorrect estimates of station's height coordinates. To reduce or minimize these errors arising from poor modeling of the wet troposphere, one possibility is to model the tropospheric refraction without the benefit of GPS observations using independent data set and the other is to estimate the tropospheric parameters directly using available GPS data. Existing theoretical models are described in the next section.

### 3.3 Models for the Troposphere

To model the troposphere, many models use information about the surface pressure, temperature, and relative humidity to derive zenith or slant delay estimates. However, almost all models require certain conditions in, or make assumptions about, the atmosphere above the station. Some commonly-used models for the tropospheric delay are, e.g., Modified Hopfield (Goad & Goodman 1974), Saastamoinen (1972), Hopfield (1969), Essen & Froome (1972), Lanyi (1984), Davis (1985), Herring (1992), and Neill (1996). In this chapter, only the first three models (Saastamoinen, Hopfield, and Modified Hopfield) are discussed in detail.

#### 3.3.1 Saastamoinen Model

This model also assumes that the atmosphere is in hydrostatic equilibrium which follows from the ideal gas law. While the Hopfield model assumes the gravity acceleration as a constant value with height, it is treated as a function of height in the Saastamoinen model. In more detail here, under hydrostatic equilibrium, the local pressure, which is assumed to be isotropic, provides the balancing force against the atmospheric weight per unit area. The equation of the state of the hydrostatic equilibrium can be written as follows:

$$dp = -g(h) \cdot \rho(H) \cdot dH \quad (3.16)$$

where

$dp$  : differential change in pressure (mbar)

$g$  : gravity with height ( $\text{m s}^{-2}$ )

$dH$  : differential change in height (m)

With the introduction of the weighted mean gravity acceleration,  $g_m$ , the above equation can be rewritten as follows:

$$\rho = -\frac{1}{g_m} \frac{dp}{dH} \quad (3.17)$$

Now, the Equation (3.12) can be rewritten using the introduction of the mean gravity acceleration as follows:

$$N_d = k_1 \frac{\rho R_o}{M_d} = k_1 R_d \rho = -k_1 R_d \frac{1}{g_m} \frac{dp}{dH} \quad (3.18)$$

The above equation is substituted to the Equation (3.14) and leads to:

$$ZHD = 10^{-6} \int_{H_s}^{\infty} N_d dH = -10^{-6} k_1 R_d \frac{1}{g_m} \int_{p_s}^{\infty} dp = -10^{-6} k_1 R_d \frac{p_o}{g_m} \quad (3.19)$$

$g_m$ , which is the weighted mean gravity acceleration, is defined as the gravitational acceleration at the center of mass of the vertical atmospheric column directly above the

station and can be approximated by the Saastamoinen equation as follows (Davis et al 1985):

$$g_m = 9.784 \cdot (1 - 0.00266 \cos 2\varphi - 0.00028H) = 9.784 \cdot f(\varphi, H) \quad (3.20)$$

where  $\varphi$  and  $H$  (km) are the latitude and height of the station, respectively.

Therefore, the zenith hydrostatic delay can be written as follows:

$$\text{ZHD} = \frac{0.0022767 p_0}{1 - 0.00266 \cos 2\varphi - 0.00028H} \quad (3.21)$$

For the zenith wet delay, Saastamoinen (1972) assumed that the water vapor pressure and temperature decrease linearly with height as follows:

$$e = e_s \left( \frac{T}{T_s} \right)^{\frac{vg}{R_d \alpha}} \quad (3.22)$$

where

$e_s$  : water vapor pressure at the surface (mbar)

$v$  : numerical coefficient to be determined from local observations

$\alpha$  : temperature lapse rate (K/km)

$T_s$  : temperature at surface (or antenna) height (K)

Final expression for the zenith wet delay by Saastamoinen (1972) is:

$$ZWD = 0.002277 \left( \frac{1255}{T_s} + 0.05 \right) e_s \quad (3.23)$$

The Saastamoinen model is generally used for the tropospheric delay model due to its model accuracy. Mendes (1994a, 1995) showed that the RMS of the hydrostatic zenith delay of this model is less than 1 millimetre and that of the zenith wet delay reaches from 8 to 46 millimetres with respect to the ray-tracing value using radiosonde data for selected areas.

### 3.3.2 Hopfield Model

This model assumes that the atmosphere is in hydrostatic equilibrium, which follows from the ideal gas law, and assumes that the acceleration due to gravity is constant with height. This model expresses the total delay in terms of up to the fourth power of the refractive index. This quartic approximation is given by:

$$N_d = N_{ds} \cdot \frac{(H_d^e - H)^4}{(H_d^e)^4} \quad (3.24)$$

$$N_{ds} = 77.624 \cdot \frac{P_{ds}}{T_s}$$

where

H : height above sea level (m)

$N_{ds}$  : surface dry refractivity

$P_{ds}$  : partial pressure for dry air at surface (mbar)

$T_s$  : surface temperature (K)

$H_d^e$  : effective height for the hydrostatic component (m)

An expression for  $H_d^e$  was obtained by using global radiosonde data:

$$H_d^e = 40136 + 148.72 \cdot (T_s - 273.16) \quad (3.25)$$

Similarly, the wet refractivity is derived under assumptions of hydrostatic equilibrium (which is not entirely valid – due to the dynamic and unpredictable behaviour of water vapor). The model can be written as

$$N_w = N_{ws} \cdot \frac{(H_w^e - H)^4}{(H_w^e)^4} \quad (3.26)$$

$$N_{ws} = -12.96 \cdot \frac{P_{ws}}{T_s} + (3.718 \cdot 10^5) \cdot \frac{P_{ws}}{T_s^2}$$

where

$N_{ws}$  : surface wet refractivity

$P_{ws}$  : partial pressure for wet air at surface (mbar)

$H_w^e$  : effective height for the wet component (11000~12000 m) (m)

Using Equations (3.24) and (3.26), the total tropospheric delay can be expressed by:

$$\begin{aligned}
 \delta\rho_{\text{tp}} &= \text{ZHD} + \text{ZWD} \\
 &= 10^{-6} N_{\text{ds}} \frac{1}{(H_{\text{d}}^{\text{e}})^4} \int_0^{H_{\text{d}}^{\text{e}}} (H_{\text{d}}^{\text{e}} - H)^4 dH + 10^{-6} N_{\text{ws}} \frac{1}{(H_{\text{w}}^{\text{e}})^4} \int_0^{H_{\text{w}}^{\text{e}}} (H_{\text{w}}^{\text{e}} - H)^4 dH \\
 &= 10^{-6} \frac{N_{\text{ds}} H_{\text{d}}^{\text{e}} + N_{\text{ws}} H_{\text{w}}^{\text{e}}}{5}
 \end{aligned} \tag{3.27}$$

The hydrostatic zenith delay model, typically, shows millimetre-level accuracies (Mendes 1994). Schuler (2001) showed that the standard deviation of the Hopfield model with respect to the Saastamoinen model revealed overall very small difference of about 0.2 mm for the hydrostatic component; for the wet component, 12.4 mm. Based on the ray-tracing using radiosonde data, Mendes (1994a) showed that the RMS of the hydrostatic zenith delay of this model reaches about over 2 mm.

### 3.3.3 Modified Hopfield Model

The Modified Hopfield model for zenith delays introduces position vectors. It is assumed that  $R_{\text{E}}$  represents radius of the Earth,  $h$  is the altitude,  $r$  is the radius from the center of the Earth to the station ( $h=0$ ),  $h_{\text{w}}$  ( $\sim 11$  km) is the equivalent height of the wet part,  $h_{\text{d}}$  ( $\sim 40$  km) is the equivalent height of the hydrostatic part, and the distance from the center of the Earth to the troposphere is given as  $h_{\text{d}} = R_{\text{E}} + h_{\text{d}}$  and  $h_{\text{w}} = R_{\text{E}} + h_{\text{w}}$ , as shown in the Figure 3.1 (Hofmann-Wellenhof 1998).

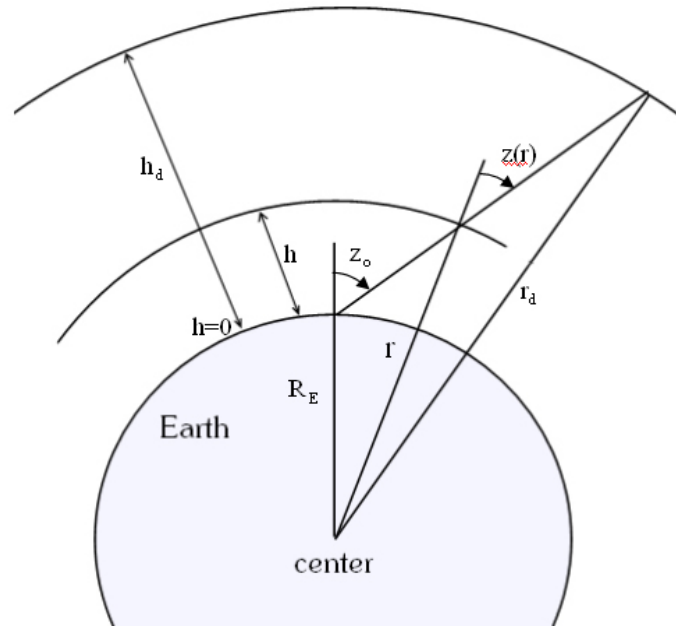


Figure 3.1: Geometry of the Modified Hopfield model

Then the refractivity and the delays for the hydrostatic and wet components can be written as follows

$$N_i(r) = N_{is} \left( \frac{r_i - r}{r_i - R_E} \right)^4, \quad d_i(z) = 10^{-6} \int_{R_E}^{r_i} N_i(r) \frac{1}{\cos z(r)} dr \quad (3.28)$$

$$\sin z(r) = \frac{R_E}{r} \sin z_0, \quad \cos z(r) = \frac{1}{r} \sqrt{r^2 - (R_E \sin z_0)^2}$$

where

$i$  : subscript, d for hydrostatic and w for wet component

$z_0$  : zenith angle of the station

$z$  : arbitrary zenith angle

Again, the delay for the hydrostatic and wet part can be rewritten as follows (Hofmann-Wellenhof 1998):

$$d_i(z) = \frac{10^{-6} N_{is}}{(r_i - R_E)^4} \int_{R_E}^{r_i} \frac{r(r_i - r)^4}{\sqrt{r^2 - (R_E \sin z_0)^2}} dr \quad (3.29)$$

Remondi (1984) introduced elevation angle instead of zenith angle such that

$$d_i(\varepsilon) = 10^{-6} N_{is} \left( \sum_{k=1}^9 \frac{\alpha_{k,i}}{k} r_i^k \right) \quad (3.30)$$

where

$$r_i = \sqrt{(R_E + h_i)^2 + (R_E \cos \varepsilon)^2} - R_E \sin \varepsilon$$

$$\alpha_{1,i} = 1$$

$$\alpha_{2,i} = 4a_i$$

$$\alpha_{3,i} = 6a_i^2 + 4b_i$$

$$\alpha_{4,i} = 4a_i(a_i^2 + 3b_i)$$

$$\alpha_{5,i} = a_i^4 + 12a_i b_i + 6b_i^2$$

$$\alpha_{6,i} = 4a_i b_i(a_i^2 + 3b_i)$$

$$\alpha_{7,i} = b_i^2(6a_i^2 + 4b_i)$$

$$\alpha_{8,i} = 4a_i b_i^3$$

$$\alpha_{9,i} = b_i^4$$

$$a_i = -\frac{\sin \varepsilon}{h_i}, b_i = -\frac{\cos^2 \varepsilon}{2h_i R_E}$$

Note that unlike the Hopfield model and Saastamoinen model described earlier for the zenith delay, the Modified Hopfield model is already introduced for slant delays.

Starting from the surface values for tropospheric pressure, temperature, and relative humidity, one usually can derive the zenith or slant delay. This requires certain assumptions for the atmosphere above the station such as hydrostatic equilibrium, and for the mapping function, which often uses empirical results based on radiosonde data. Therefore, a standard model approach does not meet the true metrological conditions, due to high temporal and spatial variations. Surface values obtained using ground-based remote sensing instruments are also not accurate enough, due to calibration errors, etc. Surface values for pressure, temperature, and relative humidity can be biased by several ground effects, and thus do not truly represent the whole atmosphere above the station.

In this research, the Modified Hopfield model is used for the tropospheric delay model as a reference model since this model is easy to implement and many of the commercial receivers still using this model as a basic tropospheric delay model. The overall cut-off angle throughout this research is applied 15 degrees elevation angle, except a ray-tracing, which suggests that all the tropospheric model accuracies may not show significant differences. Since the primary purpose of this thesis is to extensively evaluate the effect of GPS RTK performance for the Modified Hopfield model and the NOAA model for three geographical regions in USA, the mapping function should be used because the NOAA model has only the zenith delay. In the following section, some mapping functions are discussed.

### 3.4 Mapping Functions

The tropospheric delay is the shortest in the zenith direction, and becomes larger with increasing zenith angle. Using a mapping function, the zenith path delay can be projected onto a slant direction. Similar to the tropospheric models, there are many mapping functions that have been proposed, such as: cosecant, Hopfield (1969), Chao (1972), Black (1978), Davis et al (1985), Baby et al (1988), Herring (1992), Neill (1996).

The mapping functions are approximately equal to the cosecant of elevation, but there are significant deviations from this "cosecant law" due both to the curvature of the earth and the curvature of the path of the GPS signal propagating through the atmosphere. The cosecant mapping function is  $1/\sin(\epsilon)$ . Due to the large deviations for lower elevation angles, however, this function is limited to use below about 60 degrees elevation.

The Hopfield mapping function is based on the quartic refractivity profiles (Hopfield 1969). While a constant temperature lapse rate is used to derive the Hopfield mapping function, the Chao (1972) model, which is an expansion of the Marini (1972) model, uses the elevation angle in his mapping function, and defines the coefficients as global constants within a fractional expansion truncated to the second order terms as follow:

$$m_{\text{chao}}(\epsilon) = \frac{1}{\sin(\epsilon) + \frac{a}{\tan(\epsilon) + b}} \quad (3.31)$$

where

a, b : constants

$\varepsilon$  : elevation angle

From empirical data, the Chao mapping functions for the hydrostatic and wet components are expressed as follows:

$$m_{\text{chao}}(\varepsilon)_h = \frac{1}{\sin(\varepsilon) + \frac{0.00143}{\tan(\varepsilon) + 0.00035}} \quad (3.32)$$

$$m_{\text{chao}}(\varepsilon)_w = \frac{1}{\sin(\varepsilon) + \frac{0.00035}{\tan(\varepsilon) + 0.017}} \quad (3.33)$$

Despite its simplicity, the Chao mapping function proved to be unexpectedly precise (Schuler 2001).

The Black model (1978) depends slightly on the surface temperature and is based on the quartic profiles by Hopfield (1969) as follows:

$$m_{\text{be}}(\varepsilon)_i = \left( 1 - \left( \frac{\cos(\varepsilon)}{1 + (1 - 0.85) \left( \frac{H_i^e}{r_s} \right)} \right)^2 \right)^{-1/2} \quad (3.32)$$

where

$i$  : subscript for either the hydrostatic or wet component

$H_i^e$  : effective height for the hydrostatic or wet component

Davis et al (1985) requires surface meteorological data, e.g. temperature, pressure and water vapor pressure. This mapping function depends on the surface pressure, temperature, temperature lapse rate, and tropopause height.

$$m_{\text{davis}}(\varepsilon) = \frac{1}{\sin(\varepsilon) + \frac{a}{\tan(\varepsilon) + \frac{b}{\sin(\varepsilon) + c}}} \quad (3.33)$$

Herring (1992) calculates the coefficients of his function based on ray-tracing of radiosonde data for 10 sites in North America from 27° N to 65° N for elevation angles down to 3° and these coefficients are dependent on the surface pressure, site latitude and height above sea level. The Herring mapping function can be written as follows:

$$m_{\text{herring}}(\varepsilon)_i = \frac{\frac{1}{1 + \frac{a_i}{1 + \frac{b_i}{1 + c_i}}}}{\sin(\varepsilon) + \frac{a_i}{\sin(\varepsilon) + \frac{b_i}{\sin(\varepsilon) + c_i}}} \quad (3.34)$$

Typical accuracies of the existing mapping functions are similar for higher elevation angles. At about 15 degrees elevation, most of the mapping functions show sub-centimetre accuracies (Mendes 1994b). However, they start to exhibit very important differences for lower elevation angles, due to the drastic increase in tropospheric model errors as the atmospheric depth increases. Therefore, the user should select the mapping function very carefully. Even if a mapping function is performing very well at the polar regions, it should not be used in the same way in the equatorial regions, or near coastal regions, due to the uncertainties of the model in these regions.

Today, the mapping functions of Arthur Neill, derived from VLBI observations, are the most widely used, and are known to be the most accurate and easily-implemented functions. In this section, only the Neill mapping function is described in detail.

Neill(1996) uses the continued fraction form as follows:

$$m_{\text{niell}}(\varepsilon) = \frac{\frac{1}{1 + \frac{a}{1 + \frac{b}{1 + c}}}}{\sin(\varepsilon) + \frac{a}{\sin(\varepsilon) + \frac{b}{\sin \varepsilon + (c)}}} \quad (3.35)$$

The coefficients, a, b, and c are modeled by using standard meteorological data which is dependent on the latitude and takes seasonal variations into account. Therefore, this model takes into account the temporal and spatial behavior. For the hydrostatic part, these coefficients are determined based on the height, latitude and DOY (day of year). However, for the wet mapping function, they depend only on the latitude. The coefficients are calculated by the equation:

$$a(\varphi_i, t) = a_{\text{avg}}(\varphi_i) - a_{\text{amp}}(\varphi_i) \cos\left(2\pi \frac{t - T_0}{365.25}\right) \quad (3.36)$$

where

$\varphi_i$  : site latitude

a : mapping function coefficient, separated into average value and amplitude

t : time (day of year)

$T_0$  : day of year for “maximum winter” which is set to 28 days for the northern hemisphere and 211 for the southern hemisphere.

Coefficients for latitude are calculated by linear interpolation for both the hydrostatic part and wet part; however, the seasonal variations are subtracted from the average values.

The coefficients for Neill hydrostatic and wet mapping functions are given in Tables 3.1 and Table 3.2.

Table 3.1: The coefficients for Neill hydrostatic mapping function

	$\varphi_i = 15^\circ$	$\varphi_i = 30^\circ$	$\varphi_i = 45^\circ$	$\varphi_i = 60^\circ$	$\varphi_i = 75^\circ$
$a_{\text{avg}}$	$1.2769934 \cdot 10^{-3}$	$1.2683230 \cdot 10^{-3}$	$1.2465397 \cdot 10^{-3}$	$1.2196049 \cdot 10^{-3}$	$1.2045996 \cdot 10^{-3}$
$b_{\text{avg}}$	$2.9153695 \cdot 10^{-3}$	$2.9152299 \cdot 10^{-3}$	$2.9288445 \cdot 10^{-3}$	$2.9022565 \cdot 10^{-3}$	$2.9024912 \cdot 10^{-3}$
$c_{\text{avg}}$	$62.610505 \cdot 10^{-3}$	$62.837393 \cdot 10^{-3}$	$63.721774 \cdot 10^{-3}$	$63.824265 \cdot 10^{-3}$	$62.258455 \cdot 10^{-3}$
$a_{\text{amp}}$	0.0	$1.2709626 \cdot 10^{-5}$	$2.6523662 \cdot 10^{-5}$	$3.4000452 \cdot 10^{-5}$	$4.1202191 \cdot 10^{-5}$
$b_{\text{amp}}$	0.0	$2.1414979 \cdot 10^{-5}$	$3.0160779 \cdot 10^{-5}$	$7.2562722 \cdot 10^{-5}$	$11.723375 \cdot 10^{-5}$
$c_{\text{amp}}$	0.0	$9.0128400 \cdot 10^{-5}$	$4.3497037 \cdot 10^{-5}$	$84.795348 \cdot 10^{-5}$	$170.37206 \cdot 10^{-5}$
$a_{\text{height}}$	$2.53 \cdot 10^{-5}$				
$b_{\text{height}}$	$5.49 \cdot 10^{-3}$				
$c_{\text{height}}$	$1.14 \cdot 10^{-3}$				

Table 3.2: The coefficients for Neill wet mapping function

coefficient	$\varphi_i = 15^\circ$	$\varphi_i = 30^\circ$	$\varphi_i = 45^\circ$	$\varphi_i = 60^\circ$	$\varphi_i = 75^\circ$
$a_{\text{avg}}$	$5.8021897 \cdot 10^{-4}$	$5.6794847 \cdot 10^{-4}$	$5.8118019 \cdot 10^{-4}$	$5.9727542 \cdot 10^{-4}$	$6.1641693 \cdot 10^{-4}$
$b_{\text{avg}}$	$1.4275268 \cdot 10^{-3}$	$1.5138625 \cdot 10^{-3}$	$1.4572752 \cdot 10^{-3}$	$1.5007428 \cdot 10^{-3}$	$1.7599082 \cdot 10^{-3}$
$c_{\text{avg}}$	$4.3472961 \cdot 10^{-2}$	$4.6729510 \cdot 10^{-2}$	$4.3908931 \cdot 10^{-2}$	$4.4626982 \cdot 10^{-2}$	$5.4736038 \cdot 10^{-2}$

Generally, for low elevations, the errors in the GPS range observations arise mainly due to multipath and troposphere delays, and these unmodeled systematic errors decrease the quality of results. However, Hugentobler et al (2001) mentioned that these effects are marginally reduced by choosing a elevation-dependent weighting scheme.

Most of the global water vapor usually exists near the equatorial or coastal regions. Therefore, even if a mapping function performs very well at polar or mid-latitude regions, it should not be used in a similar manner in the equatorial region or near coastal regions, since the uncertainties of the model at this region increase. Range delays for the wet delay can be as low as centimetres near the pole, but up to 40 cm in the tropics (Skone

2003). In this case, a ray-tracing technique may be a promising approach to further reduce the uncertainties of the model.

### **3.5 Ray-Tracing**

Ray-tracing techniques are often used in computer graphics to make more realistic 3-D scenes. From the geometrical point of view, ray-tracing for the atmosphere gives much more realistic results than the empirical or mathematical models for the troposphere. This is because large vertical and horizontal gradients exist in the atmosphere, and these are much more significant for the lowest elevations, due to the irregularity in the water vapor content, or due to other uncertainties. Ray-tracing is known as one of the most reliable and realistic approaches for calculating the tropospheric delay (Boehm & Schuh 2003).

When both GPS information and 3-D numerical weather fields are made available, the path of a satellite signal can be calculated by using a ray-tracing technique, which will give more reliable estimates of the tropospheric delay for low elevation angles. However, in order to maximize its usage, tropospheric delays for all incoming signals from a given satellite should be respectively calculated in real-time for the given sampling rate. This would take much more time than using the mathematical models mentioned in the previous sections. Therefore, the direct application of the ray-tracer, using 3-D numerical weather fields, to GPS real-time applications has some limitations; but, if the 3-D numerical weather fields are available, then ray-tracing techniques (with a few

simplifying approximations) can be used to directly integrate slant path refractivity profiles and derive slant delay estimates.

One of these ray-tracing techniques uses the topocentric coordinates of virtual satellites, in terms of the azimuth and zenith angle to each satellite, and all necessary information regarding the total pressure, temperature, and partial water vapor pressure or relative humidity (Schuler 2001).

Another method uses Snell's law (Boehm & Schuh 2003). Figure 3.2 illustrates a ray-tracing technique, which is the one used in this research, based on the geometrical viewpoint of the method.

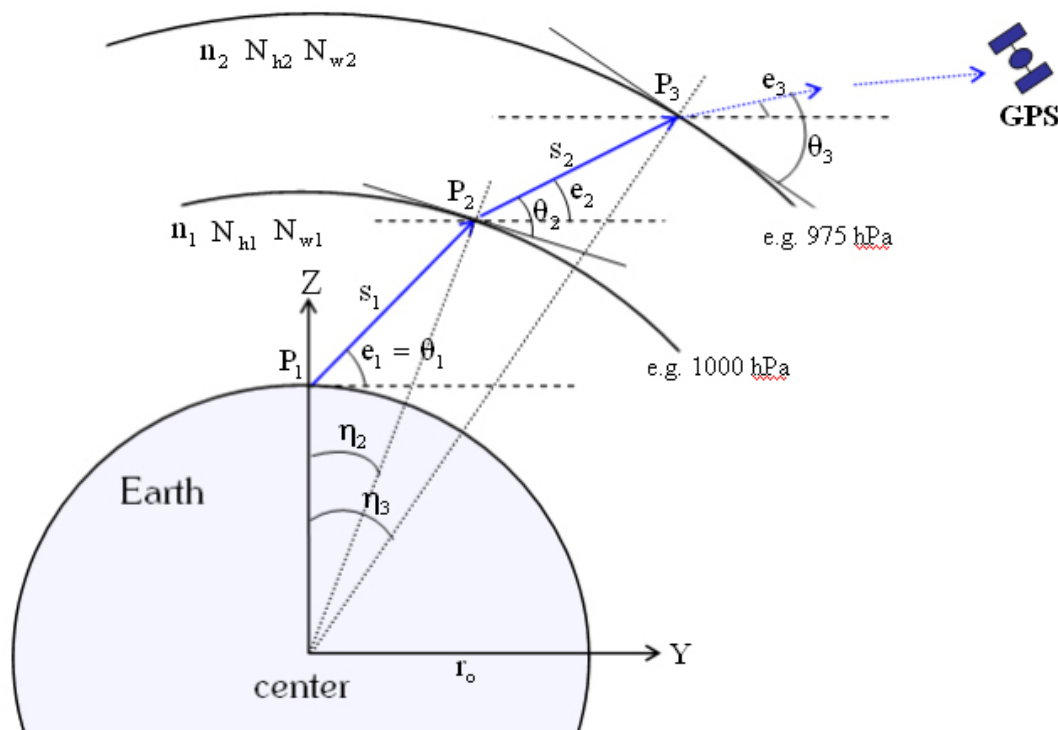


Figure 3.2: A ray-tracing scheme

At  $k$  (~1000) levels, the hydrostatic and wet refractivity can be calculated, and then the refractivity index can be estimated in this approach; these values are used to determine the  $(k-1)$  refractivity for both the hydrostatic and wet component, as well as for the refractivity index between the levels.

Using the following relationship between the height of the levels and the distance to the center of the Earth, the corresponding distance is calculated:

$$r_i = r_o + h_i \quad (3.37)$$

where subscript  $i$  represents the corresponding level. When the initial angle is given, the point  $P_1$  can be determined by using the relation,  $\theta_1 = e_1$ . After this calculation, the second point  $P_2$  and geocentric coordinates of  $P_1$  and  $P_2$  can be determined by the following equations (Boehm & Schuh 2003):

$$s_1 = -r_1 \sin \theta_1 + \sqrt{r_2^2 - r_1^2 \cos^2 \theta_1} \quad (3.38)$$

$$\begin{aligned} z_1 &= r_1 & y_1 &= 0 \\ z_2 &= z_1 + s_1 \sin e_1 & y_2 &= y_1 + s_1 \cos e_1 \end{aligned}$$

The corresponding angles at the center of the Earth can be determined by the following:

$$\begin{aligned}\eta_1 &= 0 \\ \eta_2 &= \arctan(y_2 / z_2)\end{aligned}\tag{3.39}$$

Now, the angles  $\theta_2$  and  $e_2$  at the point  $P_2$  can be determined based on Snell's law, as follows:

$$\begin{aligned}e_2 &= \theta_2 - \eta_2 \\ \theta_2 &= \arccos\left(\frac{n_1}{n_2} \cos(\theta_1 + \eta_2)\right)\end{aligned}\tag{3.40}$$

Therefore, the same strategies are performed to integrate all other shells from 2 to (k-1) levels as follows:

$$\begin{aligned}s_i &= -r_i \sin \theta_i + \sqrt{r_{i+1}^2 - r_i^2 \cos^2 \theta_i} \\ z_{i+1} &= z_i + s_i \sin e_i \\ y_{i+1} &= y_i + s_i \cos e_i \\ \eta_{i+1} &= \arctan(y_{i+1} / z_{i+1}) \\ \theta_{i+1} &= \arccos\left(\frac{n_i}{n_{i+1}} \cos(\theta_i + (\eta_{i+1} - \eta_i))\right) \\ e_{i+1} &= \theta_{i+1} - \eta_{i+1}\end{aligned}\tag{3.41}$$

Finally, one can estimate the hydrostatic slant delay  $ds_h$  and the wet slant delays  $ds_w$  using the discrete ray-tracing technique as follows:

$$ds_h = \sum_{i=1}^{k-1} s_i N_{h_i} \quad ds_w = \sum_{i=1}^{k-1} s_i N_{w_i} \quad (3.42)$$

## CHAPTER 4

### THE MULTIPLE REFERENCE STATION APPROACH

This chapter describes some background for the multiple reference station approach, and briefly discusses the network GPS RTK approach given in Section 4.2. Finally, Section 4.3 addresses the limitations in the current multiple reference station approach.

#### 4.1 Background

In order to provide reliable cm-level accuracy for GPS RTK positioning, the most important aspect is to correctly resolve the carrier phase ambiguity in terms of integer values, even in the case where short observation time is being used. Obviously, integer ambiguities are expected to yield a higher level of performance than float ambiguities, since the fixing of the ambiguities noticeably reduces the number of unknown parameters. As the use of fixed ambiguities increases the degrees of freedom, without any other changes, the resulting (or a posteriori) RMS of the observations for the fixed solution is always better than that of the float solution.

Many conditions should be satisfied, in order to correctly resolve the ambiguities: good satellite geometry, relatively short inter-receiver distances to minimize the effect of the correlated errors, such as the orbital, ionospheric, and tropospheric differential errors, and relatively clear spaces around stations to avoid multipath effects, which are dependent on

the antenna and its neighborhood. The orbital, ionospheric, and tropospheric differential error terms grow as the distance between two receivers increases. For short inter-receiver distances, the differential errors are small and, given that carrier phase multipath and noise are also small, the integer ambiguities can be correctly recovered. All non-modeled errors affect the estimated coordinates, as well as the ambiguities (Rothacher & Beutler 2002).

However, resolving ambiguities can be more difficult to achieve if the distance between the user and the reference station increases due to the decorrelation of the atmospheric and orbital errors. Therefore, to ensure a suitable level of positioning accuracy, reference stations must be placed in such a way as to limit the maximum distance to the nearest reference station. Since this traditional, single reference station, RTK positioning technique is greatly affected by the atmospheric and residual orbital errors, a more advanced method, called the multiple reference station approach, has been developed to reduce these errors, even for long baselines.

When more than one reference station is established, the reference stations can be used interactively to model the correlated errors, namely the residual troposphere, ionosphere, and orbit errors, at the location of the user. This allows the user or the reference to achieve a better position accuracy than could have been achieved using any of the reference stations independently. Fotopoulos & Cannon (2000) also showed that these differential error terms are spatially and temporally correlated. Because of this correlation, the effective inter-receiver distance can be considerably increased when the reference

stations are used interactively to model the spatially correlated errors. The advantage of the multiple reference station approach is obviously due to the spatial geometry and locations of the reference stations with respect to the user. During the period 1996-2000, the multiple reference approach referred to as MultiRef<sup>TM</sup>, was developed at the University of Calgary. In MultiRef<sup>TM</sup>, the NetAdjust method, which uses an optimal linear minimum variance estimator to reduce the correlated code and/or carrier phase errors, is used (Raquet & Lachapelle 2000), as well as other advances such as network ambiguity resolution and numerous real time components (Lachapelle et al 2000).

The MultiRef<sup>TM</sup> method estimates the differential code and carrier phase errors in the region covered by the network of reference stations, as follows (Raquet & Lachapelle 2000):

$$\begin{aligned}\delta\hat{\mathbf{I}} &= \mathbf{C}_{\delta\mathbf{I}}\mathbf{B}^T(\mathbf{B}\mathbf{C}_{\delta\mathbf{I}}\mathbf{B}^T)^{-1}(\mathbf{B}\overline{\Phi} - \lambda\Delta\nabla\mathbf{N}) \\ \delta\hat{\mathbf{I}}_r &= \mathbf{C}_{\delta\mathbf{I}_r,\delta\mathbf{I}}\mathbf{B}^T(\mathbf{B}\mathbf{C}_{\delta\mathbf{I}}\mathbf{B}^T)^{-1}(\mathbf{B}\overline{\Phi} - \lambda\Delta\nabla\mathbf{N})\end{aligned}\quad (4.1)$$

where

$\delta\hat{\mathbf{I}}$  : vector of corrections (metres)

$\mathbf{C}_{\delta\mathbf{I}_r,\delta\mathbf{I}}$  : covariance matrix between the corrected and network observations,

$\mathbf{B}$  : double differencing matrix

$\mathbf{C}_{\delta\mathbf{I}}$  : variance-covariance matrix of the network observations

$\overline{\Phi}$  : vector of the network observations (metres)

$\lambda\Delta\nabla\mathbf{N}$  : vector of the double difference ambiguities (metres).

Equation 4.1 shows that the corrections are a function of the mathematical relationship between the baselines ( $B$ ), the stochastic relationship between the baselines ( $C_{\delta l}$ ), and the stochastic relationship between the baselines and the rover ( $C_{\delta l_r, \delta l}$ ).

When the corrections are applied, this information is combined with the stochastic relationship between the rover and a single reference station, as well as with the mathematical relationship due to the double differencing of the measurements. Equation 4.1 also shows that, when using multiple reference stations for kinematic positioning, the integer (or float) ambiguities should be known at the beginning, between the network stations. Obviously, each time when a new satellite appears above the horizon at a desired mask angle, if cycle slips occur, the process of resolving the ambiguity should be reset. At lower elevation angles where atmospheric errors are prominent, Zhang (1999) mentions that the ambiguity resolution process can be enhanced when their spatial correlations over the network can be used. The multiple reference station approach has been shown to work very well on various networks, and under various conditions (Fortes et al 2000a, 2000b, 2001, Alves et al 2001, 2003, Raquet et al 1998, Raquet 1998, Zhang 1999). With good network geometry, the method achieves over fifty to sixty percent improvement in the phase misclosure at the user, relative to the traditional single reference station approach (Alves et al 2003, 2004, Cannon et al 2001, 2004). Alves et al (2003) even investigated the effects of the network geometry and network configuration

on a user's positioning and navigation performance, in the context of the multiple reference station approach, for GPS RTK positioning. Due to the difficulty in using ideal real network data, they simulated code and carrier phase observations instead. This allows for a wide range of reference position selection; they used SimGNSS2™, which is another software package developed by the University of Calgary. Investigating this phenomenon under various environmental conditions, it was found that a horizontally or vertically distributed network does not assist the network approach, in terms of error reduction and the resulting accuracy of the user's position. However, by adding one more strategically located station to the network, there can be a large improvement in both the user position accuracy and in the ambiguity resolution. There are many papers describing the design, operation, and testing of the GPS RTK system, based on the use of a multiple reference stations approach, such as: Cannon et al (2001), Petrovski et al (2002).

Multiple reference station GPS RTK positioning can be classified into the multiple baseline averaging approach and the network approach. The network approach which is similar to the traditional single point positioning using the carrier phase, means that all the single baseline solutions are combined independently to get the weighted or combined solution. However, the network integrates all the solutions into a filter, to get a theoretically more rigorous and presumably more accurate solution, and to have more options for reducing the correlated errors.

Figure 4.1 represents the same plots for the L1 phase measurement errors for the single baseline approach and for the network approach and the improvement for the network approach is evident.

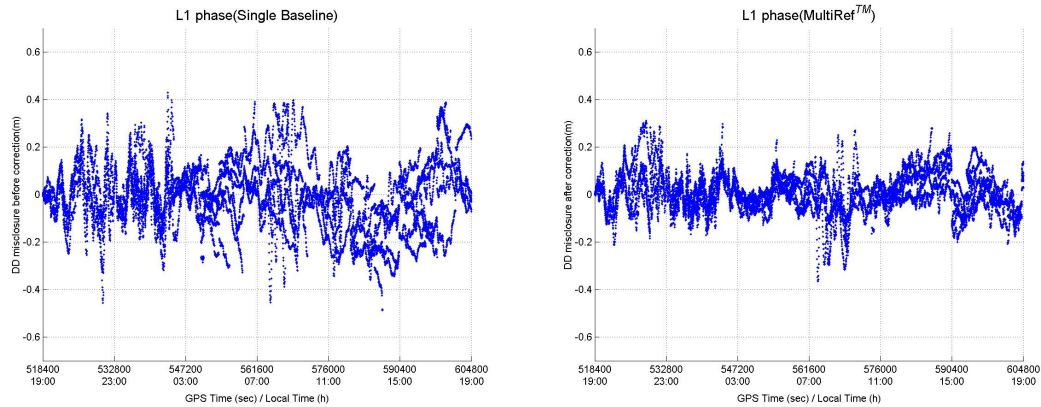


Figure 4.1: Comparison of performance between the single baseline approach and a network RTK approach. Left plot represents the double difference raw misclosures and right plot means misclosures after the network correction.

## 4.2 Network GPS RTK Approach

In the multiple reference station GPS RTK approach, errors can be modeled using measurements at more than one reference station. This allows users to estimate the correlated errors over a region, or to predict them within the network. The approach can be categorized into two different methods; single baseline averaging GPS RTK approach and network-based GPS RTK approach.

The baseline GPS averaging approach, which is easy to implement, processes each baseline independently, and averages them to derive the final position solutions. This trade-off is necessary if one wants to benefit from the simplicity of using existing single baseline software. While this approach is simple, the main disadvantage is that insufficient observations of the reference stations may be involved in the processing and this will consequently corrupt the final solutions. However, to reduce the errors, one can combine all of the observation data in a more rigorous filter to estimate the position of the user.

The network-based GPS RTK approach used herein independently processes the reference network to predict the errors at the user. It first measures the errors at the reference stations and estimates the network ambiguities, ionosphere model, and ambiguity resolution and then predicts the errors at the location of the rover anywhere within or around the reference station network using least squares collocation (Raquet & Lachapelle 2000). These predicted differential errors are then applied to the data of one of the reference stations, typically the closest reference station from the rover, and then sent to the rover. For this purpose, after the prediction of the correlated errors for the rover and the generation of the network corrections, the measurement errors are interpolated to correct the rover using a linear least-squares prediction. The covariance function, which represents the statistically correlated characteristics, should be determined before the network corrections. Raquet models and uses a covariance function which is linearly dependent on the elevation angle of a satellite and the location of the reference stations. Alves (2004c) proposes a more advanced adaptive covariance function.

Due to spatial and temporal correlations, the parameter of this function changes from day to day, and is dependent on the atmospheric conditions and networks. Despite these limitations, this method as compared to the single baseline approach has shown its effectiveness either post-mission or GPS RTK positioning in reducing the magnitudes of the correlated error sources and in improving the rover's positioning performance which allows for the network reference stations to be spaced further apart than the single baseline approach with maintaining the same level of performance (Raquet & Lachapelle 2000, Fortes et al 2000a, 2000b, 2001, Alves et al 2001). Major advantages of this network-based GPS RTK approach over single baseline approach include:

- Reducing the magnitudes of the correlated error sources
- Delivering faster and reliable ambiguity resolutions
- Covering a larger service area than single baseline approach

In this thesis, this network-based GPS RTK approach is used for the NGS CORS network which should provide better positioning accuracy for network users than does the current standard single reference station method.

### **4.3 Limitations in the Multiple Reference Station Network Approach**

Obviously, the presence of orbital, ionospheric, and tropospheric differential errors will affect the available positioning accuracy, whether float or fixed ambiguities are considered. The magnitudes of the orbital, tropospheric, and ionospheric errors will

change as the inter-receiver distance changes; that is, as the baseline distance decreases, these errors will decrease too. However, for longer baselines, the effect of these errors cannot be reduced to negligible levels, with the multiple reference approach.

Figures 4.2 and 4.3 show an example of double difference misclosures of the ionospheric-free ('IF') linear combination before and after network correction. A misclosure can be computed for every observation epoch, and for every satellite observed at the reference station. The misclosure exhibits the measurement error, with fixed ambiguities and fixed station coordinates. If it were not for modelled errors in the troposphere, ionosphere, broadcast ephemeris, satellite clock, receiver clock, and multipath, the misclosure would truly reflect the random measurement errors. In actuality, these misclosures contain the unmodelled errors as well as the unavoidable effects. Figure 4.2 and 4.3 present the plots for the double difference IF phase measurement. Although the IF combination eliminates the first order ionospheric effects, this does not mean that this combination can totally eliminate the ionospheric effect. Using network approach, however, these unmodelled errors can be further reduced and the remaining ionospheric errors can be treated as a negligible level. As shown in the figures, the relatively large errors in the single baseline approach around 1400 local time in Figure 4.2 were further eliminated. Since most of the residual ionospheric errors is further reduced using network approach, the remaining errors in Figure 4.3 may be considered as ones that are from the residual tropospheric or orbital errors. Typically the IF combination is used for a measure of the residual tropospheric or orbital effects.

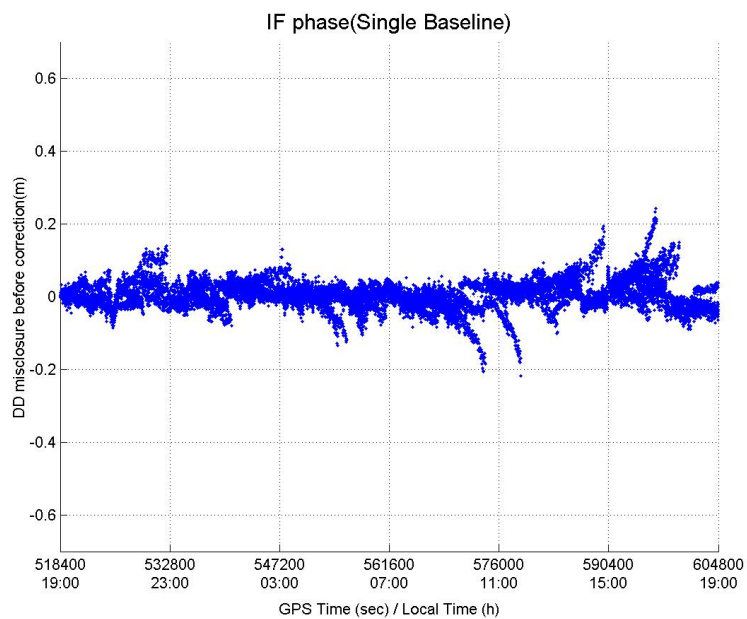


Figure 4.2: Double difference misclosures of a single baseline before network corrections are applied

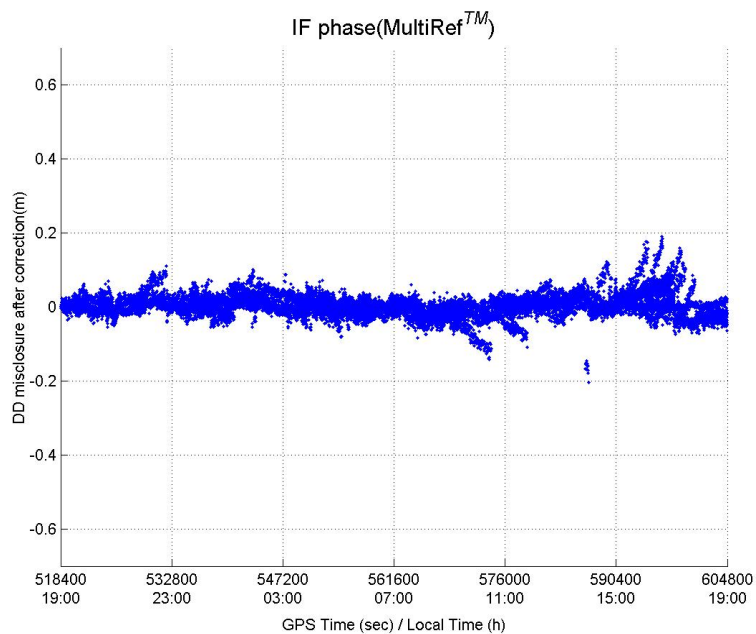


Figure 4.3: Double difference misclosures of multiple reference stations approach when network corrections are applied

However, one can argue that the level of improvement is not significant with the IF combination. Obviously, the multiple reference station approach has proven to minimize the correlated errors, but the final result is still corrupted by uncertainties in the tropospheric modeling. This is one of the limitations of the current network-based RTK approach. One can construct the probability density function (PDF) of the unmodelled error distribution, i.e. the double difference misclosures (see Figure 4.4). The red line represents the double difference misclosures after network adjustment, while the blue-dashed line shows the uncorrected double difference misclosures.

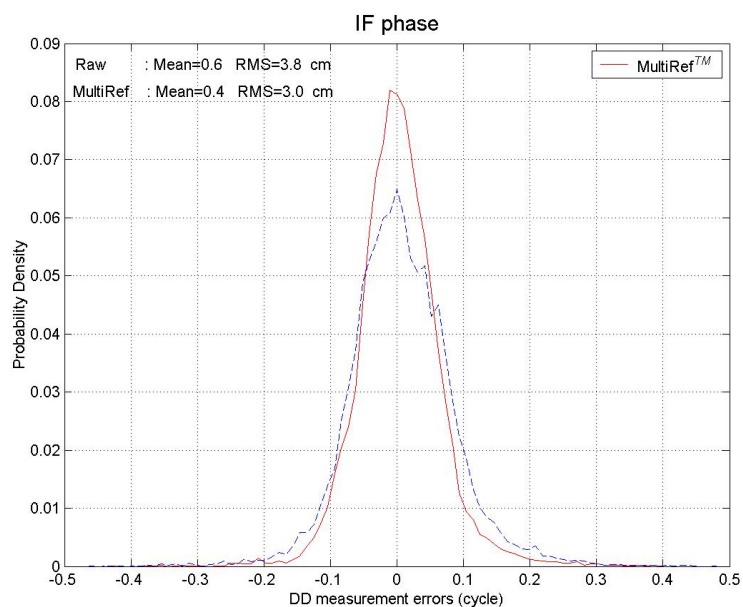


Figure 4.4: Probability density function of double difference misclosures of multiple reference station network approach and uncorrected double difference misclosures

The level of improvement is 30% in this case and shows good performance compared with the single baseline approach (blue-dashed line), even if the average network baseline

length is over 200 km. It should be noted that the remaining errors can be investigated before and after a tropospheric correction. Figure 4.5 represents double difference ionospheric-free linear combination. Unmodelled errors are typically maximized when a satellite goes down to the horizon, e.g. satellites such as PRN 31, PRN 27, or PRN 20 as shown in Figure 4.5. Those unmodelled errors may be caused by the atmosphere errors such as residual ionospheric or tropospheric errors.

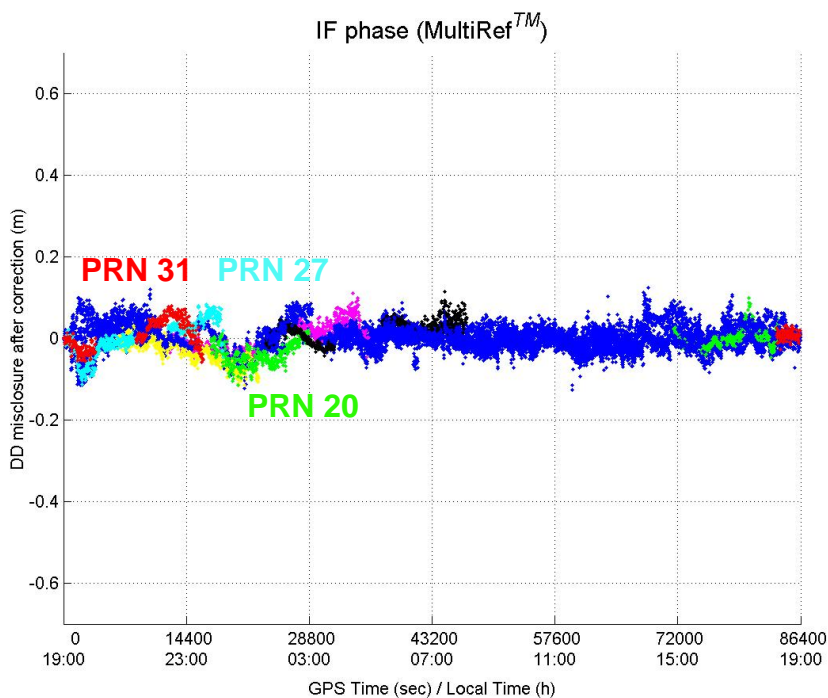


Figure 4.5: Double difference misclosures of multiple reference station network approach

The difference in the results gives an indication of the nature of the tropospheric error. However, the remaining errors after a tropospheric correction still include noise, multipath, higher-order ionospheric effects, and the error in the tropospheric correction model.

## **CHAPTER 5**

### **NOAA REAL-TIME TROPOSPHERIC CORRECTIONS**

This chapter describes the NOAA GPS-Met network in Section 5.1, and a brief overview of the NOAA RUC20 Numerical Weather Prediction model is given in Section 5.2. The last two sections describe how to retrieve the NOAA real-time tropospheric corrections (NOAA model), and shows and comparisons between NOAA predictions and the Modified Hopfield model.

#### **5.1 NOAA GPS-MET Network**

The GPS-Met branch, operated by the NOAA/FSL, was formed in response to the need for improved moisture observations to support weather forecasting, climate monitoring, and research. The primary goals of this branch are to demonstrate the major aspects of an operational GPS IPW monitoring system, assess the impact of these data on weather forecasts, assist in the transition of these techniques to operational use, and encourage the use of GPS meteorology for atmospheric research and other applications.

By assimilating GPS data, radiosonde data, and other atmospheric measurements into a numerical weather model, the GPS-Met branch is able to accurately estimate the IPW at each GPS station. Knowing the IPW, the wet tropospheric delay can be computed

accurately (see Schuler 2001). More detailed derivation of this relationship is presented in Section 5.2.

The GPS-Met network currently has more than 300 GPS stations covering CONUS, Alaska, and Hawaii. Once operational in 2008, a total of 1000 will be expected to cover North America, with inter-station distances as short as 50 km. It is also expected that, in 2010, the GPS-Met-generated atmospheric delay corrections will enable high-precision positioning and navigation (with errors of <20 cm) covering the entire CONUS (www.gpsmet.noaa.gov). Figure 5.1 shows the configuration of the current GPS-Met network. A total of 11 stations are involved for this study, and they are all treated as reference stations for a rover. Detailed scenario definition is described in Chapter 6.

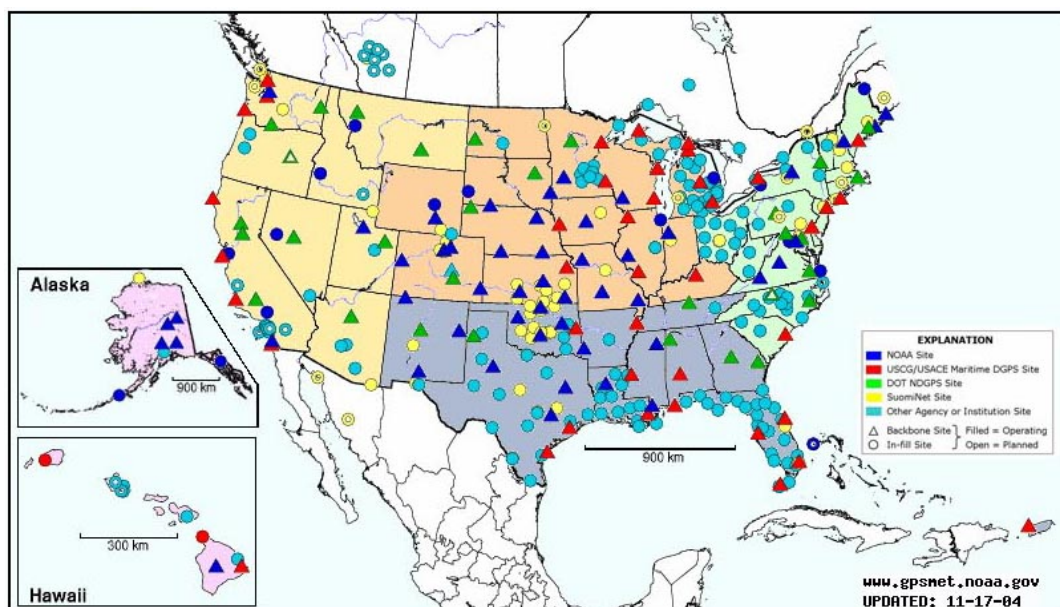


Figure 5.1: NOAA GPS-Met Network (from NOAA 2004)

As shown in Figure 5.1, some of the networks in Canada may contribute to the GPS-Met branch, including the Southern Alberta Network implemented recently by the University of Calgary.

## **5.2 NOAA RUC20 Numerical Weather Prediction Model**

The RUC is an operational atmospheric prediction system comprised primarily of a numerical forecast model, and an analysis system to initialize that model. The RUC has been developed to serve short-range weather forecasts to users (<http://maps.fsl.noaa.gov/>).

The key features are:

- High-frequency (every 1h) 3-d objective analyses over the contiguous United States
- High-frequency (every 1h) short-range weather model forecasts (out to 12 h) in support of aviation and other mesoscale weather forecast users, i.e. in size from several kilometers to around 100 kilometres.
- Assimilation of data from
  - Commercial aircraft (relayed through ACARS - Aircraft Communications, Addressing, and Reporting System)
  - Wind profilers (404 and boundary-layer 915 MHz)
  - Rawinsondes and special dropwindsondes
  - Surface reporting stations and buoys
  - Radio Acoustic Sounding System (RASS) which is experimental

- Velocity-azimuth display (VAD) winds from National Weather Service (NWS) WSR-88D radars
- Geostationary Operational Environmental Satellite (GOES) total precipitable water vapor estimates
- Special Sensor Microwave Imager (SSM/I) total precipitable water vapor estimates
- GPS total precipitable water vapor estimates
- GOES high-density visible and IR cloud drift winds

Currently, as mentioned in Section 5.1, RUC covers the lower 48 states of the U.S.A., and adjacent areas of Canada, Mexico, and oceanic areas. There are three types of RUC models available: RUC60, RUC40, and RUC20. RUC60 is based on a 60-km horizontal grid, which has 81 by 62 points, while RUC40 is based on a 40-km horizontal grid, which has 151 by 113 points.

RUC20 has a horizontal grid of 301 by 225 points, and is based on a 20 km by 20 km grid, which is much denser than the others. This model has up to 50 computational levels, as compared to the 40 levels for RUC40. RUC20 is based on enhanced model improvements, including cloud microphysics, convection, surface weather forecasts, wind/relative humidity/temperature predictions, and other parameters. The detailed output contents of RUC models can be found on the link: <http://maps.fsl.noaa.gov/> or <http://www.xdc.arm.gov/docs/ruc/ruc20gribtable.html>.

### 5.3 Retrieval of the NOAA Real-Time Tropospheric Corrections

Elgered (1993) relates the surface pressure from the Equations (3.17) to the signal delay caused by the mass of the atmosphere, as follows (cf. Gutman et al 2003):

$$\text{ZHD} = (2.2768 \pm 0.0024) \cdot 10^{-3} \frac{P_{\text{sfc}}}{f(\varphi, H)} \quad (5.1)$$

where

ZHD : zenith hydrostatic delay (m)

$P_{\text{sfc}}$  : surface pressure (mbar)

$\varphi$  : latitude

Since the surface elevation (H) at each point in the Weather (Wx) model comes from a Digital Elevation Model (DEM) with finite accuracy (Gutman et al 2003), there should be an error in the surface pressure due to the difference between the model elevation and the actual elevation. A 10 m error in elevation will result in a ~1 hPa error in pressure, or approximately 2.2 mm in zenith hydrostatic delay error (Gutman et al 2003). To solve this problem, NOAA uses a parameter called the altimeter setting (Alt) as an input to the Wx models. The altimeter setting assumes a standard atmosphere and is calculated from  $P_{\text{sfc}}$  and H using the following equation:

$$P_{\text{sfc}} = \left[ \text{Alt}^{0.193} - (1.313 \times 10^{-5}) \cdot H \right]^{5.255} \quad (5.2)$$

Since the altimeter setting (Alt) can be treated as a pressure, as in Equation (5.2), it can then be calculated for a geopotential surface that approximates mean sea level; the remaining consideration in the calculation of the zenith hydrostatic delay is to derive Alt at  $\varphi$  from the Wx model, and to obtain a rough estimate of H derived from the observed ellipsoidal height and a geoid model, such as GEOID 99.

To obtain the mean temperature, the most accurate way is the evaluation of an integral expression with help of numerical weather models or radiosonde profiles. However, it is also possible to determine this quantity with help of surface temperature. NOAA introduces a parameter called the weighted mean temperature of the atmosphere,  $T_m$ , as in Equation (5.3). Bevis et al (1992) empirically derived a linear function to predict the mean temperature for the region between Alaska and Florida which can be used globally with an acceptable level of error:

$$T_m = \frac{\int \frac{e}{T} dh}{\int \frac{e}{T^2} dh} \approx 70.2 + 0.72 \cdot T_s \quad (5.3)$$

where

$T_m$  : weighted mean temperature of the troposphere (K)

$e$  : water vapor pressure (mbar)

$T_s$  : surface pressure (K)

As described earlier, the zenith wet delay (ZWD) can be computed from the IPW estimates from the numerical weather model. The NOAA uses the following equation to retrieve the ZWD as follows:

$$ZWD = 10^{-6} \left( \frac{k_3}{T_m} + k_2' \right) \cdot R_w \cdot IWV \quad (5.4)$$

$$IPW = \frac{IWV}{\rho_{lw}} = \frac{1}{\rho_{lw}} \int_{h_0}^{\infty} \rho_w dh$$

where

$IWV$  : integrated water vapor ( $\text{kg m}^{-2}$ )

$\rho_{lw}$  : density of liquid vapor ( $\text{kg m}^{-3}$ )

$\rho_w$  : density of water vapor ( $\text{kg m}^{-3}$ )

One of the outputs of using the Wx model by the NOAA is IPW and it allows retrieving the zenith delays. When the NOAA compared the Wx model estimates of the zenith total delay with the GPS-derived zenith total delay measurements at 15 sites in the northeast U.S., over 10 days between 30 May and 9 June, 2003, it was concluded that the GPS zenith total delay (ZTD) estimates were accurate to about 1 cm of excess path length (Gutman et al 2003).

The detailed procedure for the retrieval of the NOAA tropospheric corrections is shown in Figure 5.2. When a user inputs the approximate latitude, longitude, ellipsoidal height, and time, the relevant Wx model grid files from the NOAA/FSL are retrieved. Then,

using the GEOID 99 model, the approximate geoidal and orthometric heights are computed at the location. Next, the ZWD and the altimeter settings (Alt) at one hour before and after the requested time are calculated. After performing bi-cubic interpolation, the ZWD and Alt values at the requested time are retrieved. Using known values for the altimeter setting and height information, the surface pressure can be calculated using Equation (5.2), and then the zenith hydrostatic delay (ZHD) can be calculated from Equation (5.1).

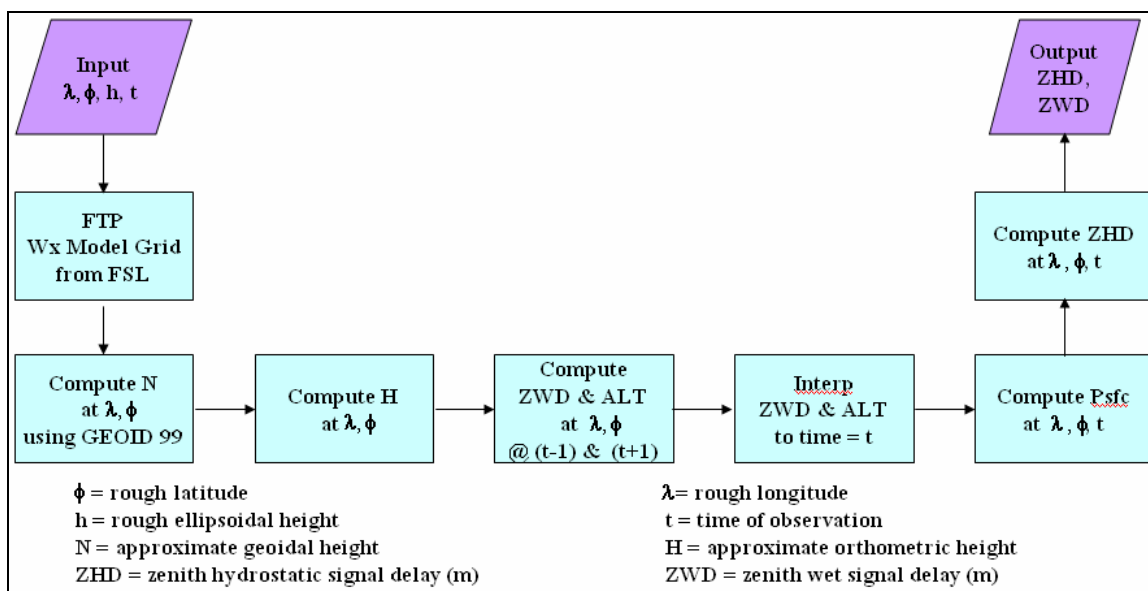


Figure 5.2: A process diagram for the retrieval of the NOAA real-time tropospheric corrections (Gutman et al 2003)

An example of a grid file which can be used to retrieve the NOAA real-time tropospheric corrections is given in Table 5.1. The data were retrieved on UTC 20h, March 15, 2004. The file lists the number of longitudes and latitudes in the first two rows. The third and fourth row contains the lower left longitude and lower left latitude, respectively. The fifth

row gives the longitude, latitude, analysis values for the zenith wet delay and altimeter setting, and 2-hour forecast values. Then, bi-cubic interpolation is performed to obtain each delay at the requested time, and then final zenith delays can be calculated.

Table 5.1: Example of contents of a grid file (0407520.GRID, hourly data)

Number of longitudes	292					
Number of latitudes	201					
lower left longitude	-125.142998					
lower left latitude	17.799000					
	Longitude	Latitude	ZWD of analysis	Alt of analysis	ZWD of 2hr-fcst	Alt of 2hr-fcst
1	-125.142998	17.799000	0.076804	1014.901306	0.079754	1015.041138
2	-124.958000	17.839001	0.076193	1014.921265	0.079156	1015.061138
3	-124.772003	17.879000	0.075583	1014.941223	0.077961	1015.101013
⋮	⋮	⋮	⋮	⋮	⋮	⋮

In detail, the program `intg.exe` from NGS GEOID 99 is used to obtain an approximate geoidal height, and the orthometric height which is the difference between the ellipsoidal and geoidal height. Then, using the program `getSiteDelay.exe`, the delay can be determined.

Table 5.2 shows an example of the retrieved values from the analysis results for the zenith wet and hydrostatic delays. It also contains their prediction values. The first column shows the time in hours; the figure in the second column of the first row is the zenith wet delay between time 0 and 2. Users then need to interpolate these values to the desired epochs, and further implement a mapping function to get the slant wet delay. In

this thesis, the Niell mapping function which is described in Section 3.4 is used for this purpose.

Table 5.2: Example of retrieved values

hours	zwd@analysis	zhd@analysis	zwd@prediction	zhd@prediction
0~2	0.33283700	2.31256000	0.33751800	2.31385000
1~3	0.33618900	2.31450000	0.32117000	2.31201000
2~4	0.33675500	2.31606000	0.32697100	2.31188000
3~5	0.30206300	2.31448000	0.31127400	2.31442000
4~6	0.30620400	2.31528000	0.31879300	2.31245000
⋮	⋮	⋮	⋮	⋮

#### **5.4 Comparison between the Modified Hopfield Model and NOAA Real-Time Tropospheric Corrections**

Unmodeled errors, to a large extent, are increased at lower elevations because the errors in zenith delay model are simply multiplied by a larger mapping function at lower elevations.

The main difference between the Modified Hopfield model and the NOAA model might be caused by that of the wet delay, as the wet delay of the NOAA model is typically larger than that of the Modified Hopfield model in this study. The NOAA model mostly improves the wet delay part, and is sensitive to the satellite elevation angle. Figure 5.3 shows the total slant delay (STD) of ZEFR station of NGS-CORS network for every

satellite, over 24 hours, for the Modified Hopfield model and the NOAA model with Niell mapping function on Sep. 3, 2003 at Florida region.

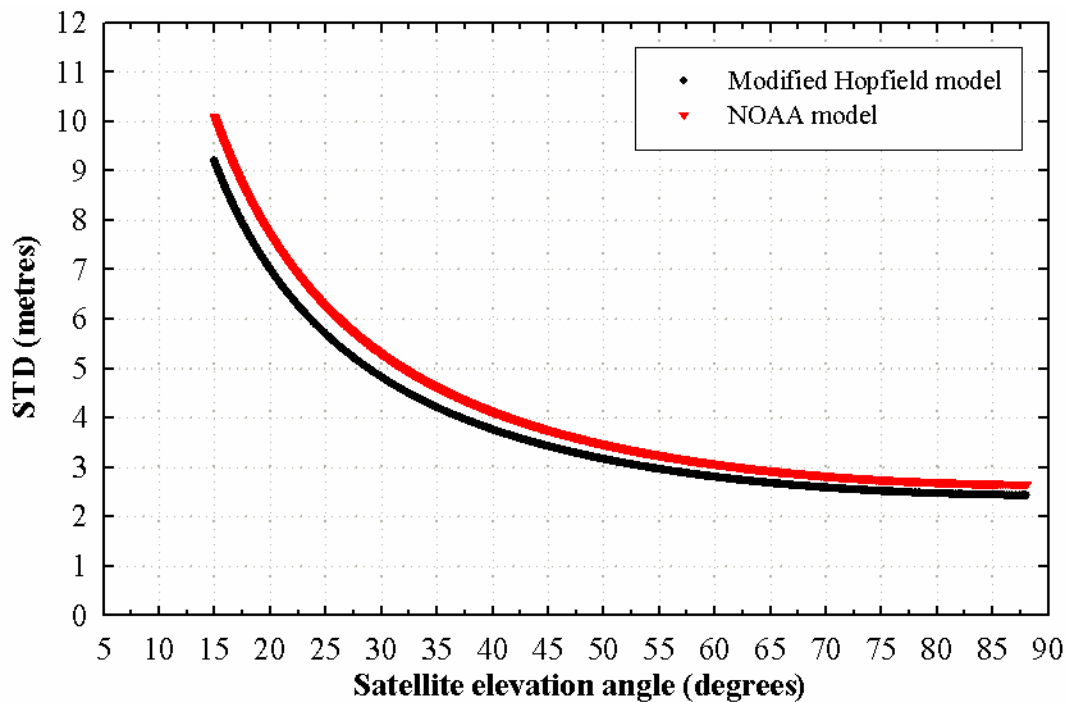


Figure 5.3: Total slant delays from the Modified Hopfield model and NOAA model

Comparing these two plots in Figure 5.3, an obvious difference can be seen. These differences are mainly due to the wet component. In Section 7.1, more detailed analysis is given.

## **CHAPTER 6**

### **SCENARIOS AND DATA DESCRIPTION**

This chapter describes the Continuously Operating Reference Station (CORS) network, operated by the NGS. Detailed descriptions of various scenarios are given in Section 6.2; in each of these, a rover is selected. The network data used for each scenario is described in Section 6.3, and the processing methods and options chosen for this research are described in Section 6.4.

#### **6.1 NGS CORS Network**

NGS, an office of NOAA's National Ocean Service, coordinates two networks of CORS:

- the National CORS network, and
- the Cooperative CORS network.

The primary purpose of these networks has been to provide GPS carrier-phase and code range measurements to support three-dimensional positioning accuracy of up to a few centimetres, relative to the National Spatial Reference System, throughout the United States and its territories. Figure 6.1 shows the current (as of September 3, 2004) CORS coverage (<http://www.ngs.noaa.gov/CORS/>).

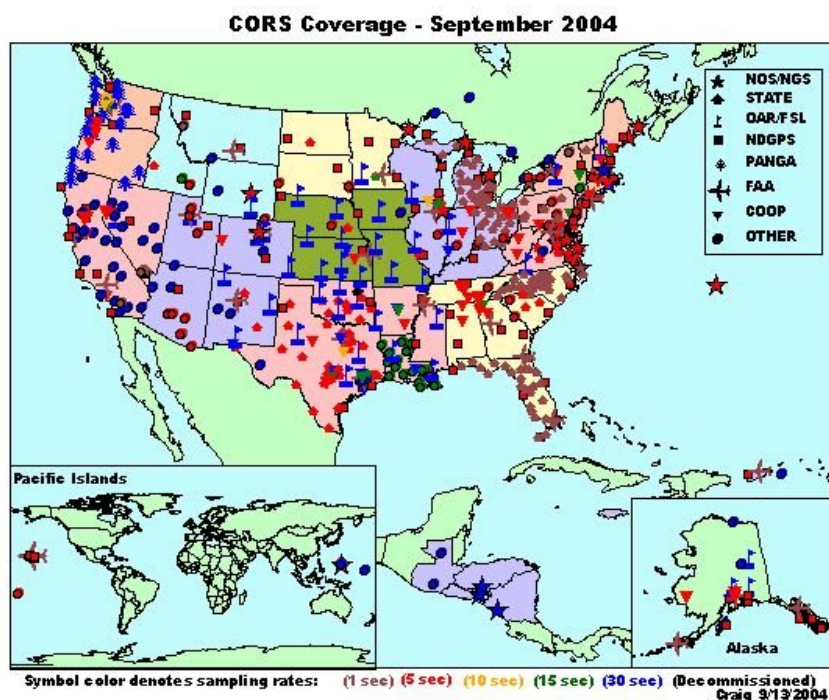


Figure 6.1: NGS CORS network (from NGS 2004)

All CORS GPS measurements can be downloaded from NGS at their original sampling rates, which range from 1 to 30 s. Cooperative CORS data are also available from the participating organizations that operate their respective sites.

Since January 11, 2004, the coordinates of each CORS station have been determined using a new terrestrial reference frame, called IGB 2000. This is based on a new terrestrial reference frame for the GPS satellites, and is produced based on the GPS observations. IGB 2000 coordinates are designed to be consistent 'on the average' with the ITRF2000 (or ITRF00), and are expected to show discrepancies for any particular site with respect to the ITRF2000 frame; however, users can normally treat IGB00 and ITRF00 as equivalent. Therefore, instead of using the IGB00 coordinates which are not

available for the CORS network, the ITRF00 coordinates for all network data chosen for each scenario (defined in Section 6.2) are used in this research. Since many of the networks contribute to the GPS-Met solution, as described in Section 5.1, careful selection is required for the rover selection for each scenario in the NGS CORS network; specifically, it is important to consider whether or not the chosen rover contributes towards the NOAA real-time tropospheric corrections.

Since the current implementation of the NGS CORS network does not support network GPS RTK, each of the reference stations must be used independently from each other. Single reference station GPS RTK is typically limited to less than ten kilometres for fixing the ambiguities as integers, and to tens of kilometres for ionospheric-free float processing. Since fixing ambiguities allows one to obtain one of the most accurate and reliable GPS positioning solutions, whenever these ambiguities are correctly resolved, inter-reference station distances over about 70 km are excluded from the selection in most cases.

As differential errors typically increase with spatial error variation, in order to measure these increased variations, the reference stations should be located at short enough intervals to resolve the spatial frequency of the errors. Consequently, the multiple reference station network approach can perform very efficiently only when the reference station spacing is short enough to measure the spatial variation of the differential atmospheric errors. Therefore, to meet these constraints, the spacing of the network for

each scenario is limited to a range from about 50 km to about 150 km. The following section describes each of the chosen scenarios, with these requirements in mind.

## **6.2 Description of Scenarios**

GPS networks in three different regions: Florida, North Carolina, and the North Eastern region, were selected for this research. Since these chosen regions have relatively dense networks as shown in Figure 6.1, the selection of the different scenarios can be easily made. The other important issue for these selections is that the chosen regions are located near the coast and may be expected to have more humidity than other areas, since the primary purpose of this research is to investigate of the effect of the GPS RTK performance by newly generated NOAA real-time tropospheric corrections as the network geometry is changed. Since the level of GPS RTK performance, which may be translated into RTK positioning results, is a function of the atmospheric errors and the distance between the rover and the closest reference station, the spatial geometry of the reference stations and that with respect to the rover can affect performance. Therefore, this research additionally discusses the effects of network geometry based on the scenarios selected herein.

This section describes each of the chosen scenarios and networks of GPS reference stations. All of the data were collected by Ashtech Z-XII3 receivers, and then downloaded from the following link: <http://www.ngs.noaa.gov/CORS/download2/>.

## 6.2.1 Florida region

### *Scenario FL1*

Figure 6.2 shows the FL1 scenario in the Florida region. Since many of the reference stations in the NGS CORS network contribute to the generation of the NOAA real-time tropospheric corrections, test “rover” stations which do not make any such contribution should be chosen in order to conduct independent analysis.

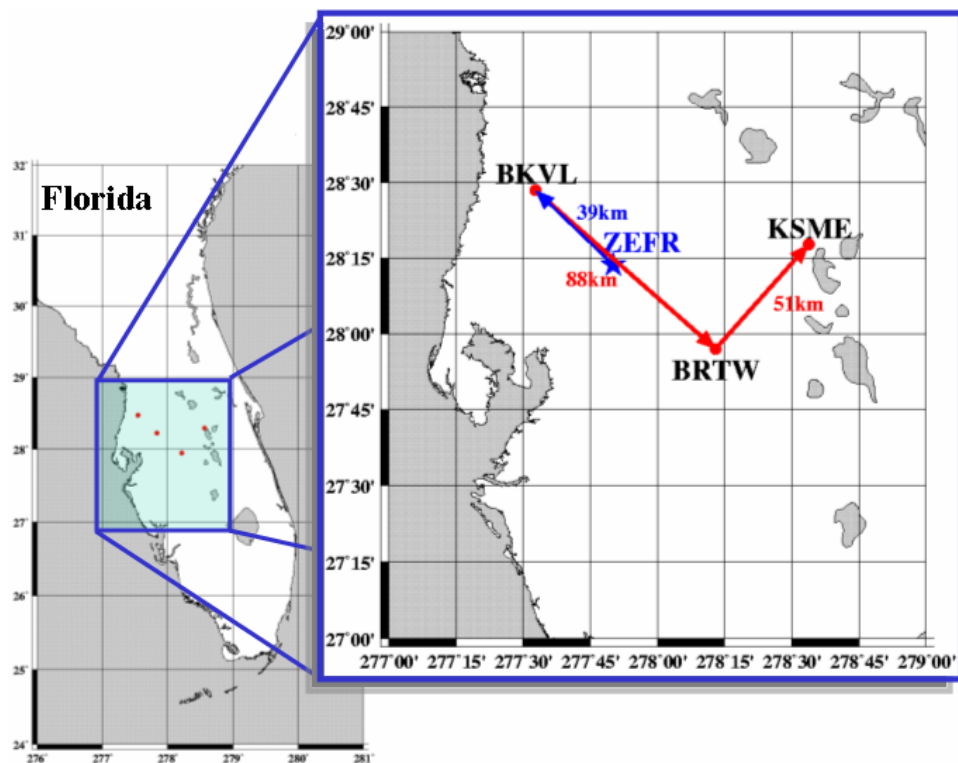


Figure 6.2: Network configuration for the first scenario (FL1). The ZEFR station is treated as a rover, and the data rate is 30 seconds

Thus, in Figure 6.2, three reference stations, BKVL, BRTW, and KSME, form a network which contributes to the generation of the NOAA real-time tropospheric corrections, while ZEFR is an NGS CORS station which can be used as a rover in this research, since it does not contribute to the NOAA GPS-Met model. Based on this general scheme, suitable scenarios may be generated.

The reference, ZEFR, is treated as a rover, which is a prediction point from the multiple reference station network approach described in Chapter 4. The reference stations BKVL, BRTW, and KSME form the network to generate network corrections for the rover. After these network corrections are generated, they are applied to the reference station closest to the rover, BKVL in this scenario. The approximate baseline length from BKVL to BRTW is 88 km; BRTW to KSME is about 51 km. The baseline length from the ZEFR rover to BKVL is about 39 km.

### ***Scenario FL2***

Figure 6.3 shows the second scenario, called FL2. It is the same as the FL1 network, except that an additional reference station, MCD1, is added to the FL1 network in the process of contributing towards the network corrections. As shown in Figure 6.3, the network used for the corrections is configured as BKVL-MCD1-BRTW-KSME; the corresponding three baseline distances are 70 km, 75 km, and 51 km, respectively, in this FL2 scenario.

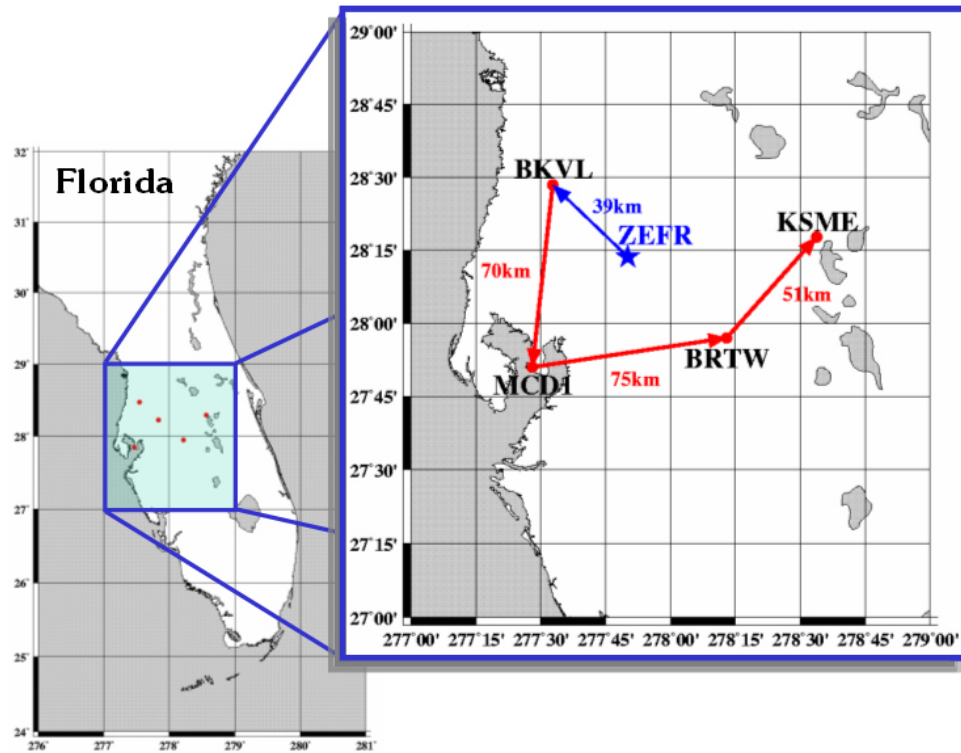


Figure 6.3: Network configuration for the second scenario (FL2). The ZEFR station is again treated as a rover, and the data rate is 30 seconds. The MCD1 station has been added to the FL1 scenario to form the new FL2 network

### 6.2.2 North Carolina region

Scenarios in the North Carolina region are defined in a manner similar to those for the Florida region. After careful comparison between the GPS-Met and NGS CORS networks, selections are made for the network contributing towards generating the NOAA real-time tropospheric corrections, and for the network which does not make any such contribution. Each of the chosen scenarios is formed using this scheme.

### *Scenario NC1*

Figure 6.4 shows the NC1 scenario in the North Carolina region. As shown in Figure 6.4, three reference stations, HILB, HIPT, and FAYR, form the network which contributes towards generating the NOAA real-time tropospheric corrections; NGS CORS station RALR is used as a rover in this research, as it does not contribute to the NOAA GPS-Met model.

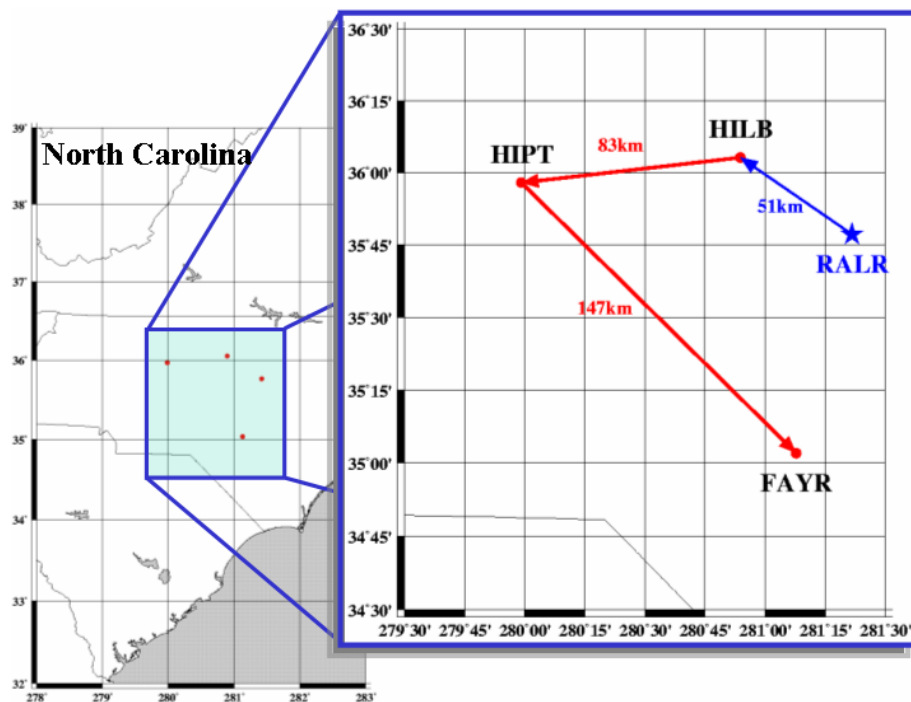


Figure 6.4: Network configuration for the third scenario (NC1). The RALR station is treated as a rover, and the data rate is 30 seconds

In this NC1 scenario, the RALR rover is located outside the network. The reference stations, HILB, HIPT, and FAYR are used together to generate network corrections for

the rover. These corrections are then applied to HILB, the closest reference station to the RALR rover. The approximate baseline length from HILB to HIPT is 83 km; HIPT to FAYR is 147 km. The baseline length from the RALR rover to HILB is about 51 km.

### *Scenario NC2*

The fourth scenario shown in Figure 6.5 is called NC2; the main difference between NC2 and NC1 is that the NC1 rover, RALR, is located outside its correction network, whereas the NC2 rover, SNFD, is located inside its network.

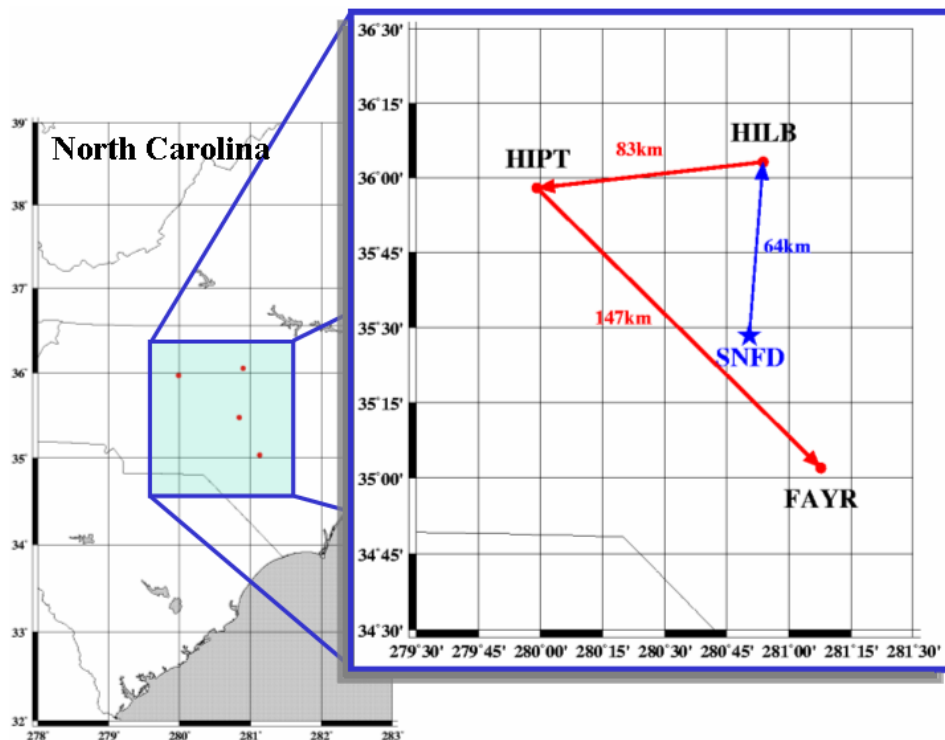


Figure 6.5: Network configuration for the fourth scenario (NC2). Instead of using RALR as the rover, the SNFD station is used as the rover in this scenario and data rate is 30 seconds

This suggests that the correlated errors for NC1 will be spatially and temporally more decorrelated as compared to NC2. As shown in Figure 6.5, the network to be corrected is configured as HILB-HIPT-FAYR. The baseline distances are 83 km, and 147 km, which are longer than in the first two scenarios in the Florida region. The baseline distance between the SNFD rover and HILB is about 64 km.

### **6.2.3 North Eastern region**

In a similar way as in the previous scenarios, scenarios in the North Eastern region are made.

#### ***Scenario NE1***

Figure 6.6 shows the NE1 scenario in the North Eastern region. The GODE station is treated as a rover, and has its prediction point located just inside the network, with a short baseline length of about 19 km to the nearest station in the reference network.

The reference stations GAIT, CORB, HNPT, and ANP1 form a network used to generate corrections for the GODE rover. These corrections are applied to the closest reference station, ANP1, in this scenario. The approximate baseline length from GAIT to CORB is 104 km; CORB to HNPT is 116 km; and HNPT to ANP1 is 63 km. The baseline length from GODE to ANP1 is about 19 km.

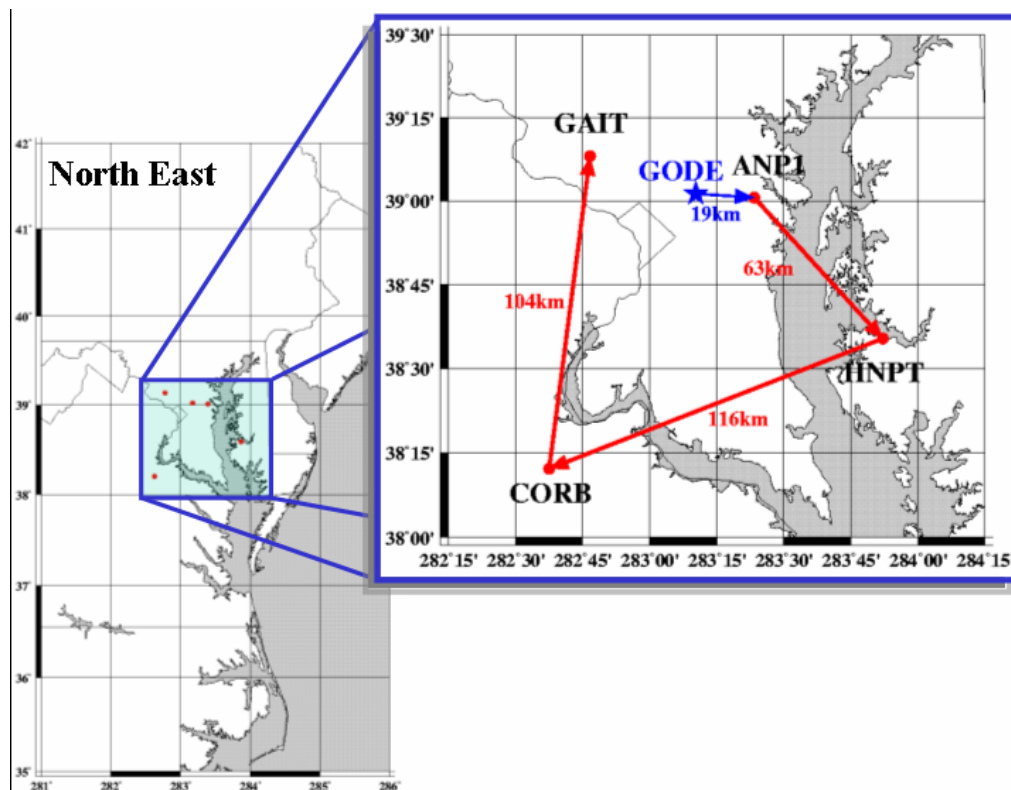


Figure 6.6: Network configuration for the fifth scenario (NE1). The GODE station is treated as a rover, and the data rate is 30 seconds

### *Scenario NE2*

The last of all the scenarios is called NE2; the main difference between NE1 and NE2 is that the NE1 rover, GODE, is located just inside the network, with a short baseline length between it and the closest reference station. However, the NE2 rover, SOL1, is located outside the reference network. As shown in Figure 6.7, the network to be used to generate corrections is configured as HNPT-ANP1-GAIT-CORB. The corresponding baseline

distances are 63 km, 55 km, and 104 km. The baseline length from SOL1 to HNPT is about 41 km.

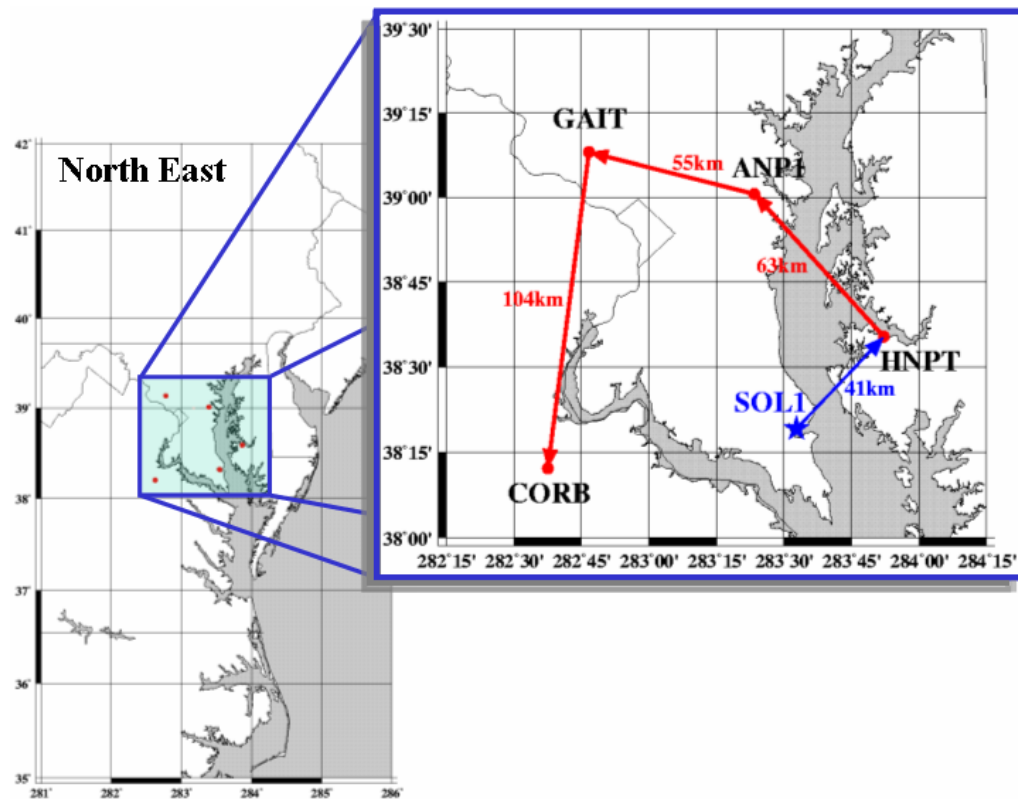


Figure 6.7: Network configuration for the sixth scenario (NE2). The SOL1 station is treated as a rover, and the data rate is 30 seconds

### 6.3 Data Description

A major objective of this thesis is to demonstrate the impact of applying NOAA real-time tropospheric corrections, and how tropospheric errors can be effectively reduced when combined with the multiple reference station approach. Since the ionosphere plays the most prominent role in terms of the error sources in GPS, the data should be carefully

selected, as any improvements in accuracy due to the use of the NOAA tropospheric corrections would be masked by the much larger effects from the ionosphere. Since the latter changes substantially from day to day, especially when there are severe ionospheric storm events, etc., general indicators which reflect ionospheric activity are very helpful in the selection of data sets. Two main indices for the ionosphere, i.e. Kp and Dst, are good indicators of the global geomagnetic activity levels. The Kp values span an allowed range from 0 to 9, and are based on magnetic field signatures at 13 sub-auroral global stations; they are derived from the mean standardized K index from those stations. At each station, the magnetic field variations are measured at 3-hourly time intervals. The Disturbed Storm Time (Dst) index, however, is derived from equatorial magnetometer stations and is used to indicate magnetic storm activity.

Larger values of the Kp index correspond to larger ionosphere changes; Kp values less than 4 mean relatively quiet ionospheric activity, and values over 7 represent a higher ionospheric activity. Therefore, all the data used in this research are carefully chosen to have values less than 5, to minimize the impact of the larger ionospheric changes, since the main concern of this research is to model the tropospheric variations. Figure 6.8 shows a sample of the Kp index, from September 2 through September 5, 2003 (the days processed for this study). In addition, in the event that these tropospheric effects happen to be small, their impact would be more difficult to validate if the situation were confused by ionospheric variations of similar or larger size. So, for the purposes of this research, relatively humid seasons or dates are chosen. Kp values for each scenario are given in Table 6.1

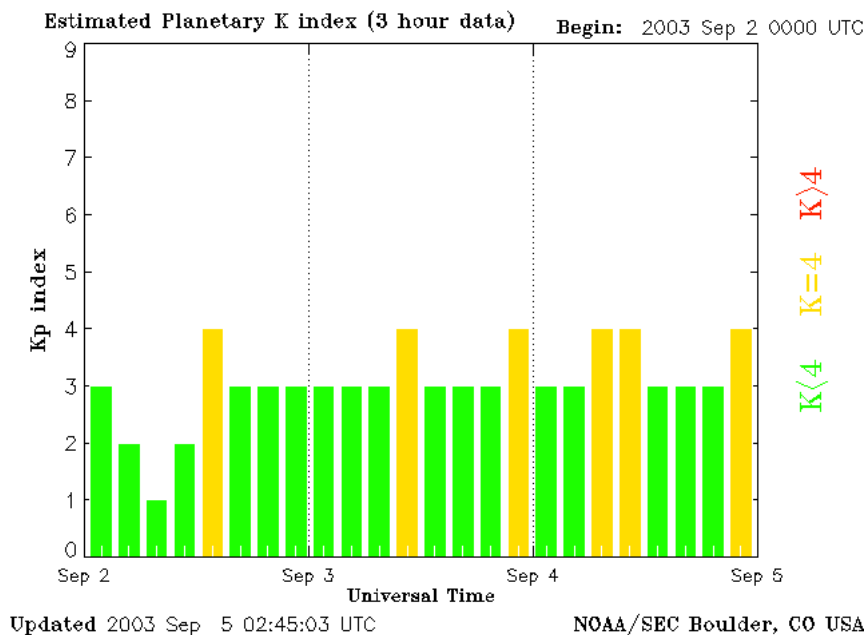


Figure 6.8: Kp index for September 2, 3, 4, and 5, 2003 (from NOAA 2005)

Using an interactive real-time water vapor data interface for retrieving ground-based GPS IPW data as operated by the NOAA/FSL, it is possible to estimate when the tropospheric effects were prominent.

Figure 6.9 shows the interactive real-time water vapor data interface from NOAA/FSL. When the parameters of this data interface are selected, such as the start and end dates, data type, and the reference stations in the FSL GPS-IPW network, the resulting values which can be derived from analysis are the IPW, pressure, temperature, relative humidity, dew point, total delay, hydrostatic delay, wet delay, and the formal errors.

Figure 6.9: Interactive NOAA real-time water vapor data interface (from NOAA 2001)

Figure 6.10 shows the IPW estimate for the near real-time solution in the Florida region, during the summer of 2003. As shown in this figure, the IPW reaches about 50 to 60 mm for most of these days, which indicates very humid weather.

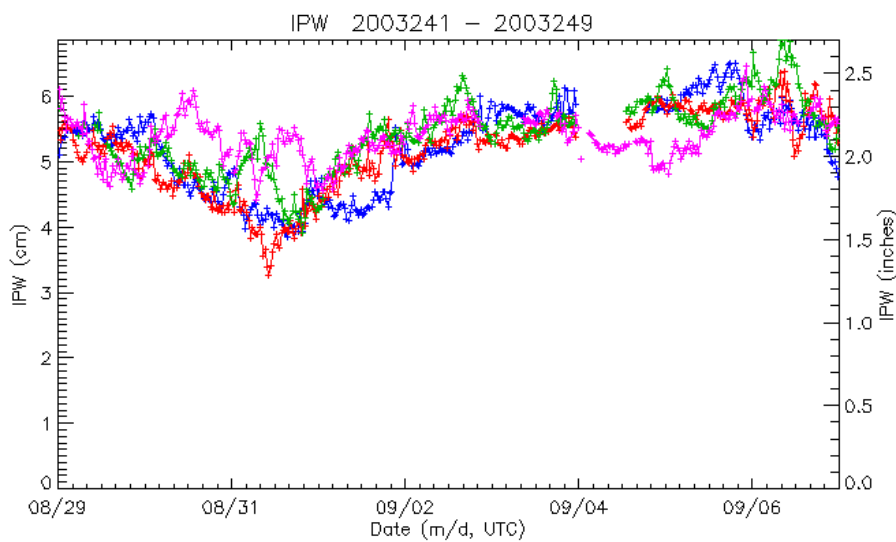


Figure 6.10: IPW during the 2003 Summer in Florida retrieved by the interface. Different colors represent different sites of the region.

Figure 6.11 shows the pressure values generated from the FLS GPS-IPW network. In comparing Figure 6.10 and 6.11, it seems that around September 6, 2003, the pressure was relatively low and this may be related to a small storm event.

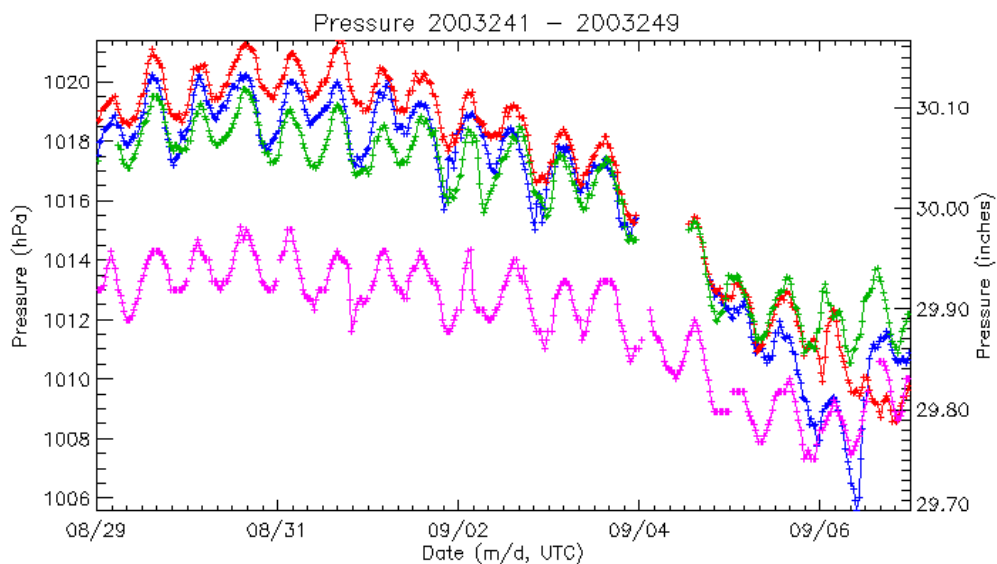


Figure 6.11: Pressure (hPa) during the 2003 Summer in Florida retrieved by the interface. Different colors represent different sites of the region.

Figure 6.12 shows the zenith wet delay (ZWD) for the same 2003 summer period, and demonstrates that the ZWD is strongly correlated with the IPW values plotted in Figure 6.10.

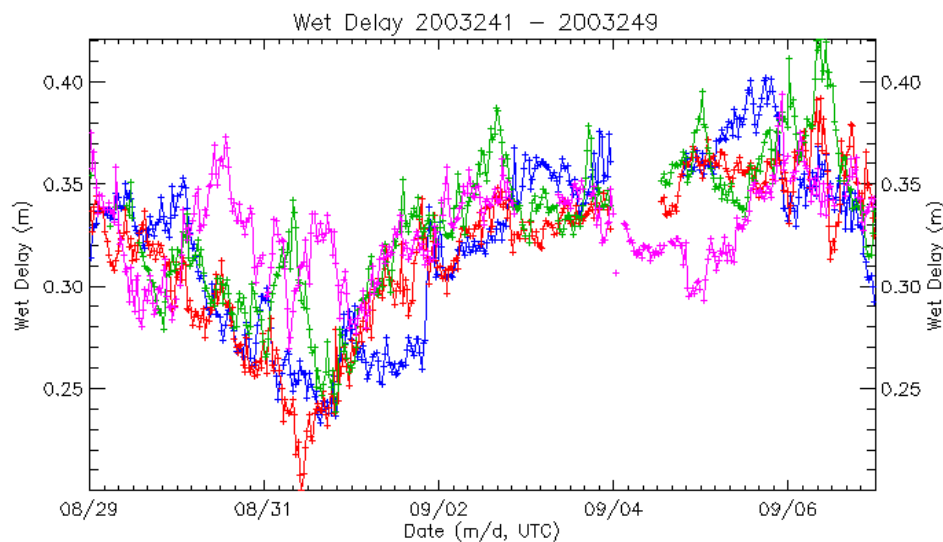


Figure 6.12: Zenith wet delays during the 2003 Summer in Florida retrieved by the interface. Different colors represent different sites of the region.

Another good example to show the value in retrieving the IPW, pressure, and the zenith wet delays, is for the North Carolina region. Since the IPW is typically high before and during the passage of severe weather, then decreases rapidly right after the typhoon center passes, and finally recovers to its nominal or lowest values within a short time, it seems that a small thunderstorm event may have happened around June 20th, 2003, as shown in Figure 6.13, for the selected network. During that time, the pressure parameter is expected to have decreased, with an accompanying increase in the wet delay. Therefore, these parameters can be good indicators of whether or not there has been a strong event in the troposphere.

Figure 6.14 shows the pressure during the 2003 summer, in the North Carolina region. The zenith wet delay for the same period is given in Figure 6.15.

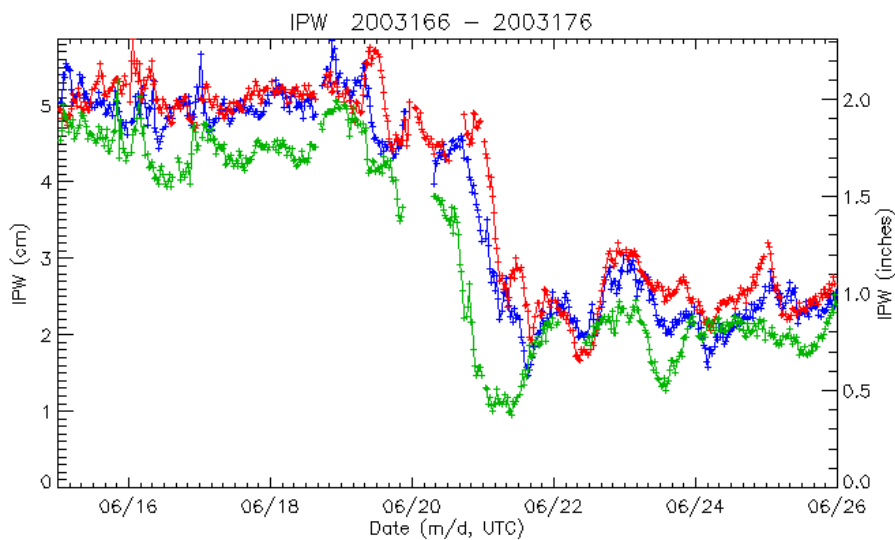


Figure 6.13: IPW during the 2003 Summer, in the North Carolina region retrieved by the interface. Different colors represent different sites of the region.

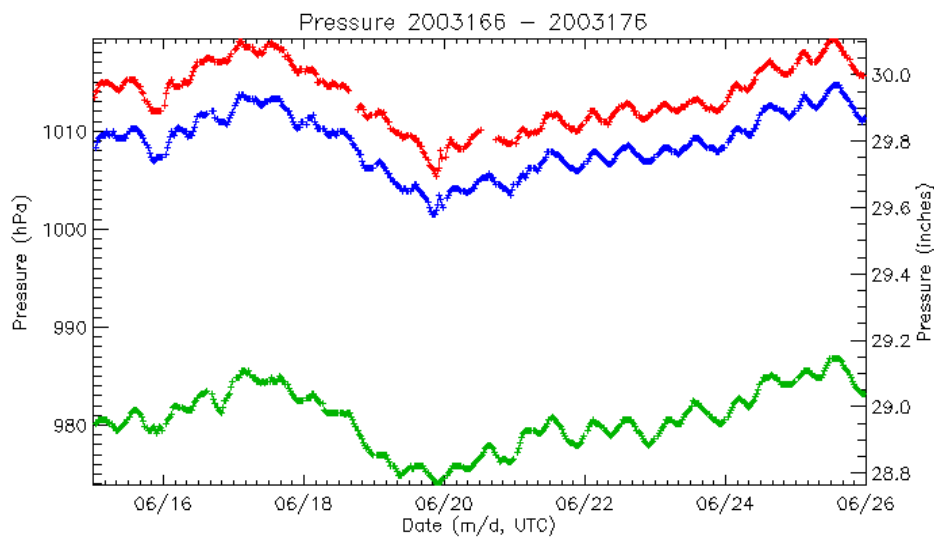


Figure 6.14: Pressure during the 2003 Summer, in the North Carolina region retrieved by the interface. Different colors represent different sites of the region.

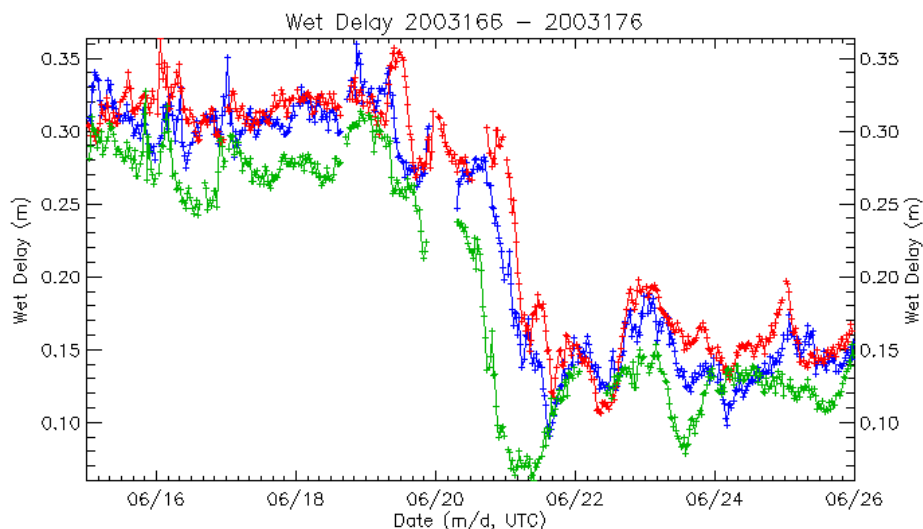


Figure 6.15: Zenith wet delay during the 2003 Summer, in the North Carolina region retrieved by the interface. Different colors represent different sites of the region.

Thus, after carefully analyzing all the parameters, which include pressure, temperature, IPW, dew point, hydrostatic delay, relative humidity, total delay, and wet delay, data for up to three consecutive days for two seasons in 2003 and in 2004 are selected for each network, and in each scenario. All these days are selected based on the calculated values of these parameters. The selected dates and detailed atmospheric conditions for the data in each network are shown in Table 6.1.

Table 6.1: Dates for the data in each network

Region & Season	Summer (2003)	Atmospheric condition	Winter (2004)	Atmospheric condition	Spring (2003)	Atmospheric condition
Florida	Sep. 3-4	Very humid & $3 < Kp < 4$	Jan. 18-20	Humid & $2 < Kp < 4$	-	-
North Carolina	Jun. 16-17	Very humid & $2 < Kp < 6$	Jan. 25-27	Humid to dry & $1 < Kp < 5$	-	-
North Eastern	Aug. 1-3	Very humid & $3 < Kp < 5$	-	-	Jun. 7-9	Humid & $3 < Kp < 5$

## 6.4 Processing method

There are two main objectives in this thesis. The first one is to evaluate the real-time tropospheric corrections based on those from NOAA, and compare these values with those predicted by the Modified Hopfield model. Instead of direct comparison of the slant wet delay values between those two tropospheric models, misclosures for GPS RTK performance are mainly calculated to see the impact of the NOAA tropospheric model in terms of error reduction. The second objective is to assess and compare the results between the Modified Hopfield model and a ray-tracing technique, which is only applied when the mask angle is below 10 degrees. This section describes each of these methods, and the options used.

### *Performance comparison between NOAA real-time tropospheric corrections and the Modified Hopfield model*

MultiRef™ is used to generate network corrections with and without NOAA real-time tropospheric corrections. These corrections are then applied to the raw data. The performance of the multiple reference station approach and the effect of using the NOAA real-time tropospheric model are analyzed in the observation domain. The reduction of the measurement errors, i.e. the DD misclosures, is shown for the raw L1 and L2 observations, the wide-lane linear combination, the ionospheric-free linear combination, and the geometry-free linear combination. The ionospheric-free combination is a good

indicator for demonstrating the error reduction of the tropospheric effects in this research. Ionospheric-free fixed solutions are calculated for each baseline.

For performing this research, the following nine steps are performed for each scenario and each day, i.e.:

- Data input for each scenario
- Synchronization for double differences
- Quality check for cycle slips and misclosures
- Modeling of the troposphere by three methods: the Modified Hopfield model, NOAA model, or ray-tracing
- Kalman Filtering for stochastic modeling for the ionosphere and ambiguity
- Ambiguity resolution using LAMBDA method
- Generation of network correction using least squares collocation
- Applying corrections to the reference station
- Generate corrected or uncorrected double difference misclosures.

The processing should be performed twice to see the effect of two different tropospheric delay models both in the single baseline approach and in the network-based approach. After generation of the network corrections, these corrections are applied to one of the closest reference stations since the errors are estimated at every reference station, the use of any one reference station will yield the same level of accuracy.

Figure 6.16 shows the flow diagram for the performance comparison between the NOAA real-time tropospheric corrections and the Modified Hopfield model as the tropospheric delay model used for both the single baseline approach and the network-based approach.

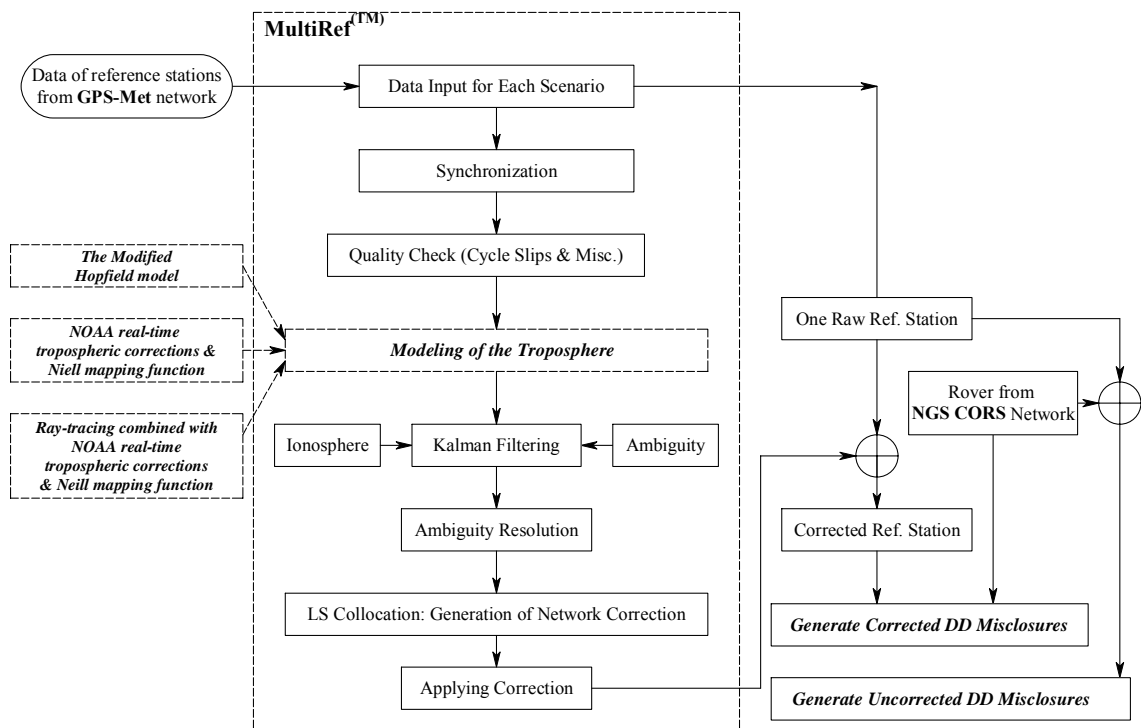


Figure 6.16: Flow diagram for the performance comparison between the NOAA real-time tropospheric corrections and the Modified Hopfield model

### ***Ray Tracing***

The NOAA real-time tropospheric corrections are calculated using only the zenith delay for the hydrostatic and wet components, and then applying the Niell mapping function to convert to slant path. Since the mapping function also has uncertainties, it would be better

if the range delay is directly calculated using a ray-tracing technique. Typically, ray-tracing is performed using radiosonde data to generate an absolute or true value for validating the zenith wet delay. Radiosondes gather data by balloon-borne instruments with radio transmitting capabilities, and these have been one of the most important of the atmospheric devices, containing instruments capable of making direct measurements of air temperature, humidity, and pressure, with height, typically to altitudes of approximately 30 km. Though radiosondes provide a good vertical resolution, they are not typically used due to their poor horizontal resolution and cost. In this research, the ray-tracing technique described in Chapter 3 is used.

In order to use the ray-tracing technique, raw data from the RUC20 numerical model are used. These raw data can be obtained from the Atmospheric Radiation Measurement (ARM) Program sponsored by the U.S. Department of Energy, the Office of Science, the Office of Biological and Environmental Research, Environmental Sciences Division. Once a request is completed, the ARM will save the retrieved files into a specific directory, or the desired data can be directly obtained from the archive. More general information on the procedures by which to get the desired data can be found at the following link: <http://www.arm.gov>.

Table 6.2 shows the current RUC data availability, as provided by the ARM. Current RUC 20 data are available from the ARM Archive approximately 4 days after they are generated. Since the `sgpallruc20*` netCDF files, which cover the entire RUC domain, are no longer available from the ARM archive, a GRIB format is chosen for this research. In

Table 6.3, the files named sgpruc20\* are "cropped" to cover latitudes from 34.21 to 38.93 degrees, and longitudes from -100 to -95 degrees. The files named sgpsynruc20isobX1.c1 have reduced resolution (grid cells are averaged to 40 km resolution), but cover the full RUC domain. More general information for a GRIB format can be found on the following link: <http://www.nco.ncep.noaa.gov>.

Table 6.2: RUC data availability (from ARM 2004)

Data Stream Name	Start Date	End Date
<b>RUC netCDF</b>		
sgpfslruc60X1.c0	10/24/1994	11/16/1994
sgpallruc60X1.c0	05/08/1996	04/23/1998
sgpruc60X1.c1	05/08/1996	04/23/1998
sgpallruc40hybrX1.c1	12/04/1998	4/16/2002
sgpallruc40isobX1.c1	04/20/1998	4/16/2002
sgpallruc20hybrX1.c1	4/18/2002	10/16/2002
sgpallruc20isobX1.c1	4/18/2002	10/16/2002
sgpruc20hybrX1.c1	4/18/2002	current
sgpruc20isobX1.c1	4/18/2002	current
sgpsynruc20isobX1.c1	4/18/2002	current
<b>RUC GRIB Input files from FSL</b>		
sgpallruc40hybrX1.00	12/04/1998	4/16/2002
sgpallruc40isobX1.00	04/20/1998	4/16/2002
sgpallruc20hybrX1.00	4/18/2002	current
sgpallruc20isobX1.00	4/18/2002	current
sgpfnnallruc20isobX1.00	4/18/2002	current

Currently, the raw data of RUC20, which do cover the entire RUC domain, are available only from the ARM archive, in GRIB format, instead of the RUC netCDF format; the latter is easier to handle and easier to arrange for a data interface than the GRIB format. For users of the GRIB format, a special script or interface, such as the Grid Analysis and

Display System (GrADS), is needed to see the contents. GrADS is an interactive desktop tool that is used for easy access, manipulation, and visualization of earth science data. Furthermore, GrADS can be interfaced with data sets in binary, GRIB, Network Common Data Form (NetCDF), or HDF-SDS formats. GrADS uses a 4-Dimensional data environment: longitude, latitude, vertical level, and time. Data sets are placed within this 4-D space by use of a data descriptor file. GrADS interprets station data, as well as gridded data, and the grids may be regular, non-linearly spaced, gaussian, or of variable resolution. More detailed information on GrADS can be found at the following link: <http://grads.iges.org/>.

RUC20 raw data can be retrieved by the ARM archive, and the contents are readable via a GrADS interface. The retrieved raw data of RUC20 is in the archive file:

- `sgpallruc20isobX1.00.20030903.000000.raw.tar.v0`

This file is a bundled ".tar" file containing 24-hourly GRIB files. Each of the files contains the following information:

- 37 isobaric levels from 1000 hPa to 100 hPa, at intervals of 25 hPa,
- 92 variables, including surface convective precipitation, dew point, geopotential height, relative humidity, pressure, temperature in Kelvin, pressure vertical velocity and direction, etc.

In order to use a ray-tracing technique, basic parameters, such as the geopotential height, relative humidity, temperature for each latitude and longitude, as well as each isobaric level of a desired location should be extracted from the file. To extract these parameters, a specific GrADS script is made. Table 6.3 shows the GrADS script used in this research.

Table 6.3: A GrADS script to extract the desired parameters from GRIB data into text format

<pre>'reinit' 'open FLruc20-090300.ctl' x=220 while(x&lt;=240) 'set x 'x y=60 while(y&lt;=73) 'set y 'y z=1 while(z&lt;=37) 'set z 'z ' q dims' lon2=sublin(result,2) lon=subwrld(lon2,6) lat2=sublin(result,3) lat=subwrld(lat2,6) level2=sublin(result,4)</pre>	<pre>'set t 1' 'd HGTprs' hgt=subwrld(result,10) 'd RHprs' rh = subwrld(result,10) 'd TMPprs' temp = subwrld(result,10)  rc = write ("FLruc20-FL090300.txt",lon' 'lat' 'lev' 'hgt' 'rh' 'temp)  z=z+1 endwhile y=y+1 endwhile x=x+1 endwhile</pre>
---	--

Figure 6.14 shows one of the parameters, namely the relative humidity of each pressure level, which is extracted from the RUC20 GRIB data for the ZEFR locations at UTC 0h, September 3, 2003.

The final parameters over the station are determined based on a horizontal interpolation over four nearby grid points. Since the desired parameters are extracted from the raw RUC20 data, the next step is to calculate the density for the hydrostatic and wet components.

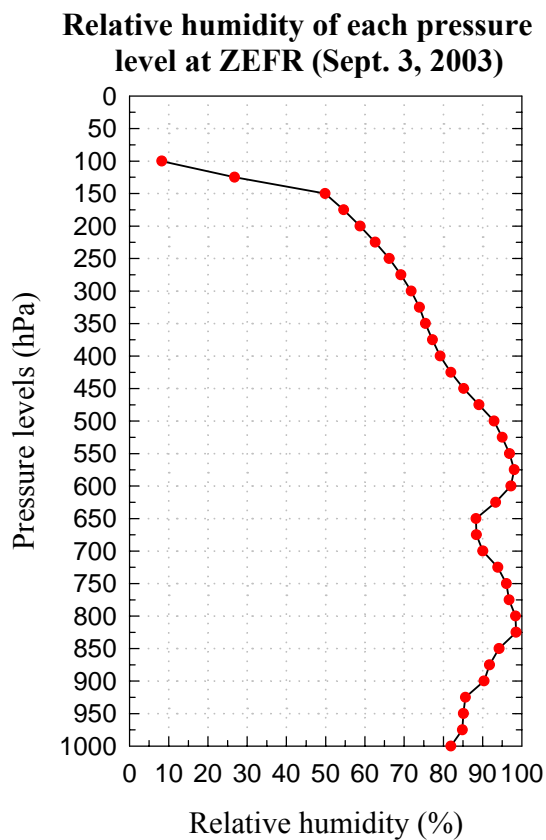


Figure 6.17: Relative humidity of each pressure level, at the ZEFR station

After determination of the density, each of the refractivity values is determined from the following equations:

$$\rho = \rho_d + \rho_w$$

$$\rho_d = (p - e) \frac{M_d}{R} \frac{1}{T}$$

$$\rho_w = e \frac{M_w}{R} \frac{1}{T}$$

$$N = (n - 1) \cdot 10^6 = N_h + N_w$$

$$N_h = k_1 \frac{M_d}{R} \rho \quad (6.1)$$

$$N_w = k_3 \frac{e}{T^2} + k_2' \frac{e}{T}$$

$$e = \frac{H_{rh}}{100} e^{-37.2465+0.213166T-0.000256908T^2}$$

where

$\rho$  : total density ( $\text{kg} \cdot \text{m}^{-3}$ )

$\rho_w$  : density of the wet component

$\rho_h$  : density of the hydrostatic component

$p$  : total pressure (hPa)

$R$  : gas constant

$M_w$  : specific gas constant of wet air

$M_d$  : specific gas constant of dry air

$H_{rh}$  : relative humidity (percentage)

$T$  : temperature (Kelvin)

$e$  : water vapor pressure (hPa)

After obtaining the interpolated values, one can calculate the refractivity for the hydrostatic and wet components using the above equations. Finally, the refractivity index,  $n$ , can be retrieved.

Then, each path delay for each layer can be integrated using equations (3.18) through (3.23), as described in Chapter 3.

### *Processing Options*

As shown in Figure 6.16, the MultiRef™ software package which was developed by the University of Calgary (Lachapelle et al 2000), is used for this research. Table 6.4 shows the processing options used in the software for each network and each scenario. Three different tropospheric delay models are implemented, namely the Modified Hopfield model, the NOAA real-time tropospheric corrections, and the ray tracing method. The ray-tracing is only applied for one scenario, FL1, for one day.

Table 6.4: Options used in MultiRef™, for each network, and each scenario

Software	MultiRef™			
Troposphere model	Modified Hopfield model	NOAA real-time tropospheric corrections	Ray-tracing	
Data Span	24 hours			
Processing interval	30 seconds			
Data Type	RINEX			
Ephemeris	Broadcast			
Mask Angle	15 degrees		5 degrees	
Constraints	-	-	Ele > 10 deg	5 deg < Ele < 10 deg
Mapping functions	-	Niell hydrostatic & wet mapping function	NOAA real-time tropospheric corrections & Niell mapping function	-
characteristic	-	-	Combined approach	
Frequencies Used	L1 & L2			
Ionosphere	Stochastic model (correlation time = 10 min applied)			
Output	Network corrections & double difference misclosures			

In each case, individual double difference misclosures are calculated over 24-hour periods using the NGS CORS network dual-frequency data, the wide-lane linear combination, the ionospheric-free linear combination, and the geometry-free linear combination. The data processing interval is 30 seconds and the data formatted as RINEX are used.

For the mask angle, 15 degrees is used for the Modified Hopfield model and the NOAA real-time tropospheric corrections. For the ray-tracing method, 5 degrees is applied. In this case, however, if the elevation of a satellite is over 10 degrees, the NOAA real-time tropospheric corrections are used and, if the elevation of a satellite is less than 10 degrees, the ray-tracing values are applied for the tropospheric delay model. The Neill hydrostatic mapping function and wet mapping function are used for the NOAA real-time tropospheric corrections. Dual frequencies are used with stochastic ionospheric modeling.

## CHAPTER 7

### PERFORMANCE ANALYSIS FOR EACH SCENARIO

The performance of the multiple reference station approach, for each scenario defined in Section 6.2, is evaluated for applying both the Modified Hopfield model and the NOAA real-time tropospheric model; the analysis is carried out in the observation domain. The reduction of measurement errors is shown for five different observations: the original L1 and L2 observations, the wide-lane linear combination, the ionospheric-free linear combination, and the geometry-free linear combination.

The wide-lane linear combination is often used in ambiguity resolution. Since a range of wavelengths of the wide-lane linear combination provides larger search space than a single frequency, for the purposes of ambiguity resolution, it is easier to resolve the L1 ambiguity once the wide-lane ambiguity is determined. The increase in the wavelength range helps to reduce some of the errors by over 70% (see Raquet 1998, Liu 2003) in units of cycles, such as those arising in the troposphere, ionosphere, satellite's orbits, and receiver position. For example, the ionospheric error in units of cycles is reduced to  $17/60$  of a wavelength due to the increase in the wavelength, resulting in a higher resistance to the ionospheric error. Therefore the wide-lane combination helps to resolve the ambiguity faster, while the noise in the combination is however dramatically increased to over four times that of the L1 measurement errors and these increased errors are reflected in the final results.

The ionospheric-free linear combination, a good indicator of the performance measure of residual error of the troposphere and orbit, is:

$$\Phi_{IF} = \Phi_{L1} - \frac{f_{L2}}{f_{L1}} \Phi_{L2} \text{ (cycles)} \quad (7.1)$$

When the ionospheric-free linear combination is combined with the DD technique, which allows the elimination or reduction of many of the correlated errors, most of the ionospheric errors will disappear. This is a very efficient method, which works for almost all cases, and gives a reliable solution. However, due to the loss of the integer characteristic of the ambiguity, as shown in Equation (7.1), an approach in combination with the wide-lane linear combination, called a cascade scheme, is often used to maximize the efficiency. Once the wide-lane ambiguities are resolved, then the L1 and L2 ambiguities can be sequentially determined, as shown in the equation below (Liu 2003, Hofmann-Wellenhof et al 1998). With the L1 and L2 ambiguities known, the results of the ionospheric-free linear combination can be determined by introducing ambiguities as integer values:

$$\Phi_{L1} - \frac{\lambda_{L1}}{\lambda_{L2}} \Phi_{L2} - \frac{\lambda_{L1}}{\lambda_{L2}} N_{WL} = \frac{\rho}{\lambda_{IF}} + \frac{\lambda_{L2} - \lambda_{L1}}{\lambda_{L2}} N_{L1} + \delta_{error} \quad (7.2)$$

where

$$N_{WL} = N_{L1} - N_{L2}$$

$\delta_{error}$  : error terms

The geometry-free linear combination is the difference between the L1 and L2 measurements, in units of length (metres in this case). This is typically used to show the error reduction in the ionosphere.

As a performance measure, the double difference (DD) misclosure is used in this research.

The DD misclosure can be defined by

$$\text{DD misclosure} = B_n \ell_n - \lambda \nabla \Delta N_n \quad (7.2)$$

where

$B_n$  : DD matrix

$\ell_n$  : measurement minus range measurement for the network

$\lambda$  : wavelength for L1 or L2

$\nabla \Delta N_n$  : DD ambiguity

Thus, the DD misclosures show the measurement errors, for fixed ambiguities and fixed station coordinates, and they can be computed for every epoch and for every satellite observed at the reference station. If it were not for model errors in the troposphere, ionosphere, broadcast ephemeris, satellite clock, receiver clock, and multipath, the misclosures would truly reflect the random measurement errors. Since the misclosures contain the effects of the remaining unmodelled errors, they are often used as a performance measure of the error reduction. Basically, this DD misclosure is used to gauge the level of improvement in the observation domain.

This chapter presents the analysis of each scenario in the observation domain. Section 7.1 gives the results, for each scenario, of the multiple reference station approach, based on the use of the Modified Hopfield model and the NOAA model, respectively. The results of the ray-tracing are given in Section 7.2, and a brief assessment of the performance of these methods is provided. As described before, the reduction of measurement errors is shown for the raw L1 and L2 observations, the wide-lane linear combination, the ionospheric-free linear combination, and the geometry-free linear combination. A detailed flow diagram is shown in Figure 6.16.

### **7.1 Results of the Multiple Reference Station Network Approach using the NOAA real-time Tropospheric Corrections**

Figure 7.1 shows a time series of the DD misclosures of the raw data which is a single reference station approach without any network correction, while Figure 7.2 shows the DD misclosures of the data corrected by the NOAA model, when combined with the network approach. Data on September 3, 2003 in the Florida region are used to analyze the effect of the network approach for those plots. The data used span 24 hours, at intervals of 30 seconds. The horizontal axis in both figures gives the time in seconds, and the vertical axis gives the DD misclosures in metres. The blue dots in the figures show the DD misclosures for both fixed and float ambiguities, and the green dots show the DD misclosures for fixed ambiguities only. From these two plots, it is clear that the unmodelled errors, which are mostly correlated errors, are efficiently reduced when using

the network approach. As a result, one can expect that this approach can also yield a better quality position solution.

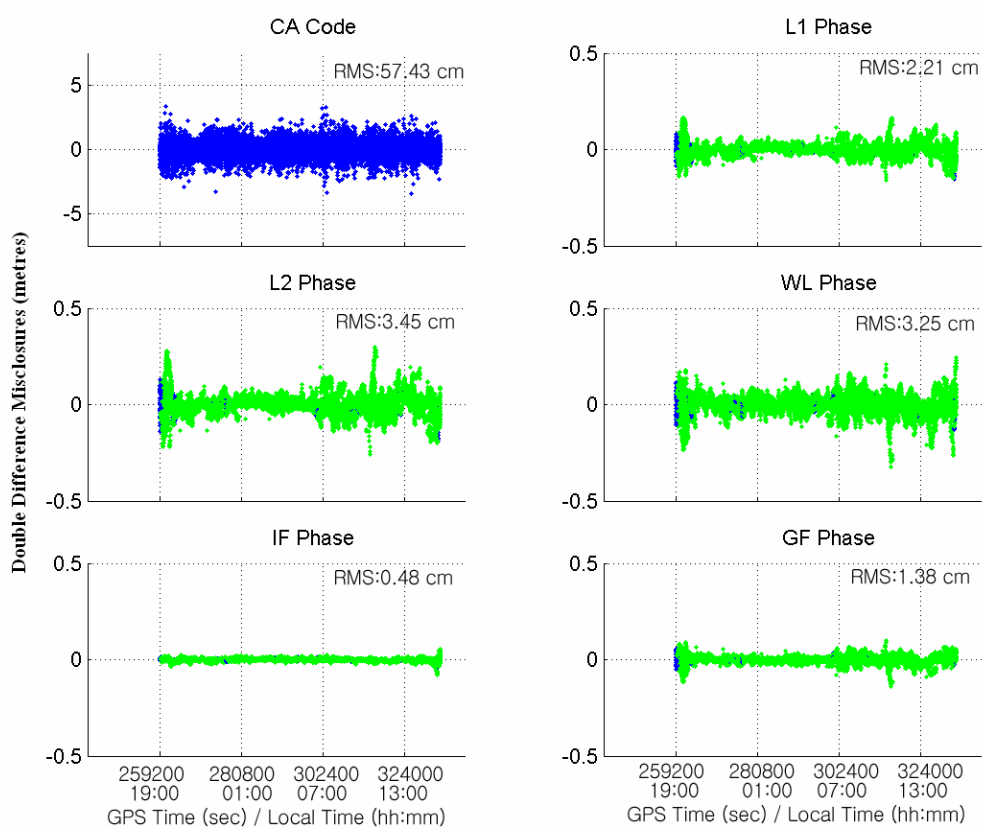


Figure 7.1: Raw data DD misclosures

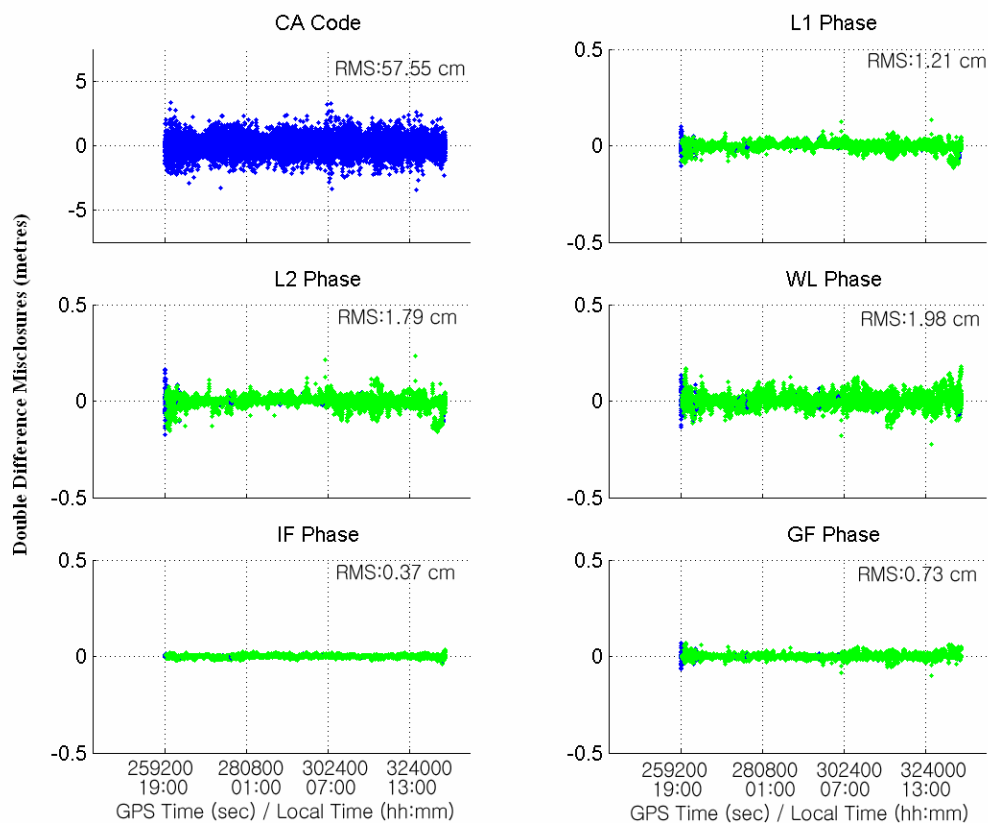


Figure 7.2: The DD misclosures of the data corrected by the NOAA model, when combined with the network approach

Instead of showing all the plots, the RMS of the DD misclosures, and their level of improvement for each scenario and for each of the three geographical locations, is given in Subsection 7.1.1.

### 7.1.1 Florida region

#### *Scenario FLI*

Figure 7.3 shows the results, in the observation domain, for the first scenario in the Florida region on September 3, 2003. This scenario, called FL1, is shown in Figure 6.2. As shown in Figure 7.3, there are four different RMS values of the DD misclosures, for each of four cases of five different observables:

- RMS values of the DD misclosures for the single baseline approach, using the raw observations and the Modified Hopfield model (represented as "Single-M.Hop" in Figure 7.3) for the troposphere.
- RMS values of the DD misclosures for the single baseline approach, using the raw observations and the NOAA model (Single-NOAA in Figure 7.3).
- RMS values of the DD misclosures for the network approach, using the multiple reference stations and the Modified Hopfield model (Network-M.Hop in Figure 7.3).
- RMS values of the DD misclosures for the network approach, using the multiple reference stations and the NOAA model (Network-NOAA in Figure 7.3).

Therefore, as shown in the Figure, there are 20 cases for each day and each scenario; i.e., 2 cases of RTK approaches (the single baseline approach or the network approach), 2 cases of tropospheric model (the modified Hopfield model or the NOAA model), and 5 cases of observables (L1, L2, WL, IF, or GF). This makes a total of  $2*2*5 = 20$  cases, altogether.

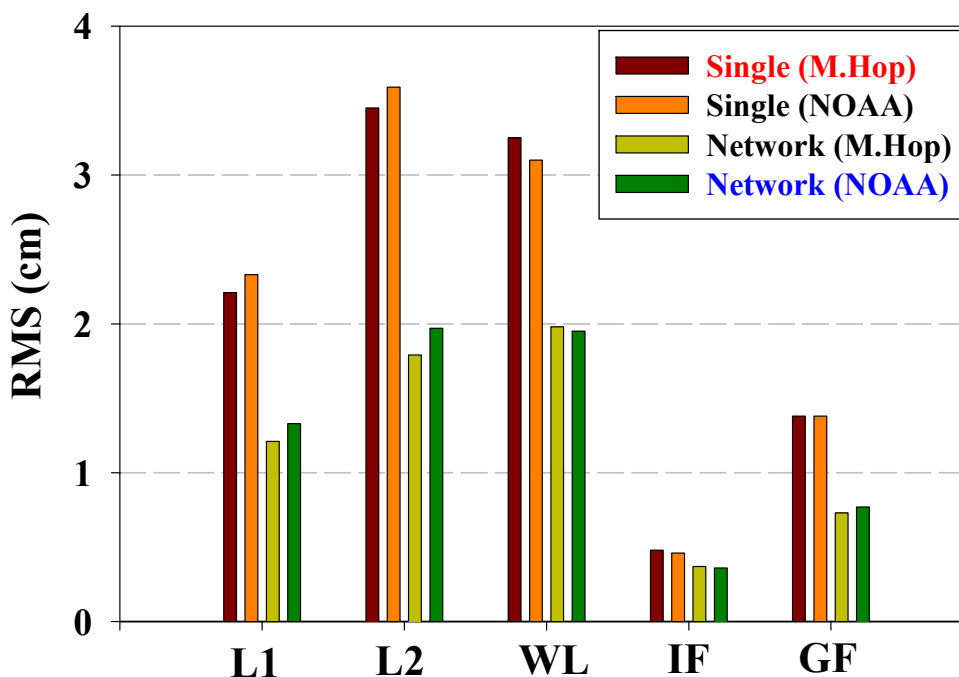


Figure 7.3: DD misclosures for FL1 scenario, 3 September 2003

In Figure 7.3, the vertical axis gives the RMS values of the DD misclosures, while the horizontal axis shows the various possible cases in choosing the frequency (i.e. single or multiple reference stations), the tropospheric model (i.e. Modified Hopfield or NOAA), and five different observables (i.e. L1, L2, wide-lane, ionospheric-free, or geometry-free). As is clear in Figure 7.3, the network approach shows a very good and consistent overall improvement.

Table 7.1 gives a summary of the observation domain results for scenario FL1, and the level of improvement with respect to the raw DD misclosures, as calculated for the "single baseline" approach, using the Modified Hopfield tropospheric model (this is given the label "Single baseline" in the Tables). The network approach is effective in reducing

the effect of measurement errors for the L1, L2, WL and GF observables; the level of improvement, when using the Modified Hopfield model integrated with the network approach, ranges from 22% to 48%, with an average of about 44%. An inspection of Figure 7.3 shows that the numerical improvement is of the order of 0.7 to 1.5 cm. The network approach also improves the IF results, namely by 23% and 24%. However the DD misclosures with the single reference station approach are already sub-cm and the numerical improvement is therefore very small. This is because the effect of the ionosphere dominates the measurement errors and the IF observables are the only derived observables that remove most of the ionospheric effect. The remaining residual tropospheric effect is obviously very small and network modeling cannot provide much improvement. This phenomenon is not uncommon and has been observed by other researchers (e.g. Dao et al 2004). The NOAA model also shows a consistent level of improvement, when combined with the network approach, ranging from 24% to 45%, with an average of about 39%. Using the NOAA model, we can see that the level of improvement of the ionospheric-free combination, which is typically used to show the error reduction for the tropospheric effect and orbit error, shows a slightly better performance than that of the Modified Hopfield model.

Table 7.1: Percentage of improvement (%) relative to the single baseline approach by the modified Hopfield model for scenario FL1, 3 September 2003

Improvement (%)		L1	L2	WL	IF	GF
Single baseline	NOAA	-5	-4	5	4	0
Network (Corrected)	M.Hop	45	48	39	23	47
	NOAA	43	45	37	24	44

Figure 7.4 shows the observation domain results of scenario FL1 on September 4, 2003. The results are generally consistent with those of the previous day. The results are summarized in Table 7.2; the level of improvement for the network approach ranges from 12 % to 28 %, with an average of about 18%, which is slightly lower than that of the previous day. The ionospheric-free combination, when using the NOAA model, however, shows a 28% improvement, which is a better performance than that of the Modified Hopfield model, and also better than any from the previous day. The numerical improvement in the latter case is still low however (less than 2 mm) due to the reason discussed earlier.

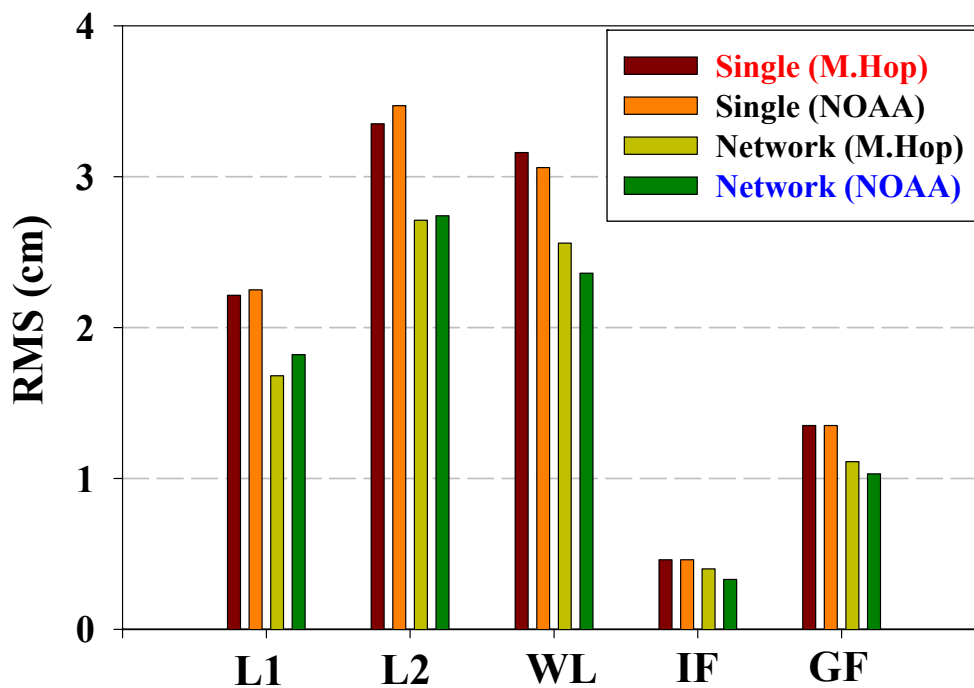


Figure 7.4: DD misclosures for FL1 scenario, 4 September 2003

Table 7.2: Percentage of improvement (%) relative to the single baseline approach by the modified Hopfield model for scenario FL1, 4 September 2003

Improvement (%)		L1	L2	WL	IF	GF
Single baseline	NOAA	-5	-3	3	0	0
	M.Hop	21	19	19	12	19
Network (Corrected)	NOAA	19	21	23	28	24

Figure 7.5 shows the level of improvement in the observation domain results for scenario FL1, for each observable over a period of 5 days. Both plots show the improvements achieved through using the network approach. These plots are made to assess whether or not there is a consistent improvement for different seasons and on consecutive days. The 5 selected days shown in Figure 7.5 are: September 3, 2003; September 4, 2003; January 18, 2004; January 19, 2004; January 20, 2004.

The left plot in Figure 7.5 shows the level of improvement in percent, as compared to the results for the single reference station approach using the Modified Hopfield model for the troposphere. The right plot shows the corresponding improvement achieved by using the NOAA model. In both these plots, the vertical axis gives the improvement in percent, the front horizontal axis shows five different observables, and the side horizontal axis gives the observation dates. As we can see in this figure, the level of improvement is very consistent for each observable, from day to day.

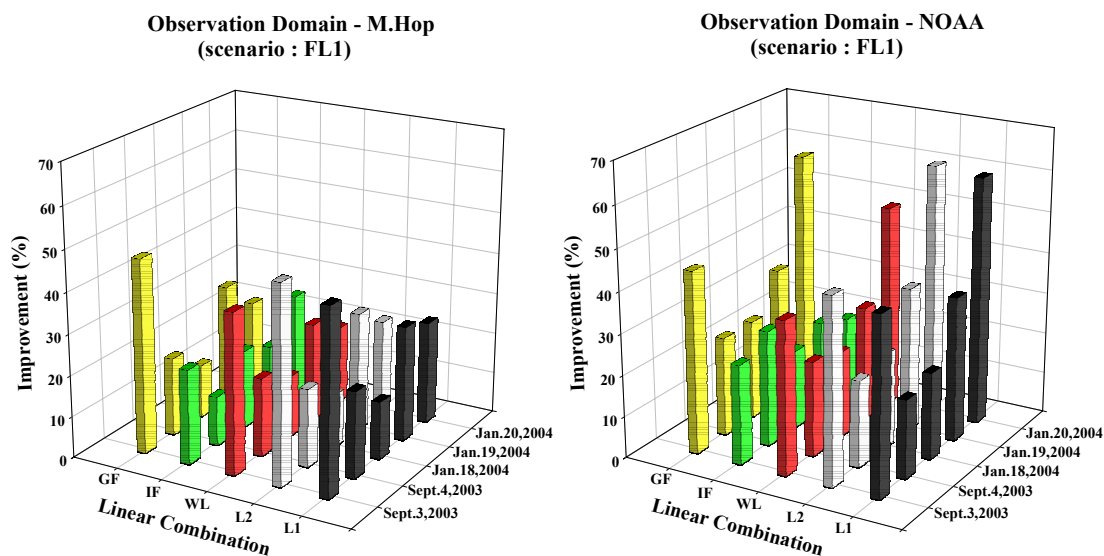


Figure 7.5: Levels of improvement in the observation domain results for scenario FL1, for five different observables, over five days in 2003 summer, and 2004 winter

Table 7.3 gives a summary of the statistics of overall performance in the observation domain results, for scenario FL1 over the 5 days, in terms of the level of improvement (%) achieved in using the Modified Hopfield model, and the NOAA model. Table 7.3 shows that the overall performance in using the network approach is very effective in reducing the measurement errors, regardless of which tropospheric model is used. Though the mean value of the improvement via the NOAA model is better than that of the Modified Hopfield model, the standard deviations of the improvement via the Modified Hopfield model are better than those using the NOAA model, except for the ionospheric-free linear combination case.

The mean level of improvement with the NOAA model ranges from 22% to 37%, with an average of about 33%, which is much better than that for the Modified Hopfield model, which ranges from 10% to 27%, with an average of about 16%. The ionospheric-free combination, when using the NOAA model, however, shows a 22% improvement with decreased standard deviation, which is a better performance than that of the Modified Hopfield model, and also better than any from the previous day. Whereas in this case, the ionospheric-free combination result shows that the NOAA model outperforms the Modified Hopfield model, which suggests that changes in the tropospheric effect are the dominant effects on that day, the standard deviations of the other observables do not show any improvement, as shown in Table 7.3, suggesting that the NOAA model overcompensated for the error.

Table 7.3: Statistics of the overall performance in the level of improvement (%) for scenario FL1, over the five days

	Level of improvement (%) compared to the raw DD misclosure									
Model	The Modified Hopfield model					NOAA real-time tropospheric corrections				
Obs.	L1	L2	WL	IF	GF	L1	L2	WL	IF	GF
Mean	26.6	10	23.2	19	25.8	35.6	37	31.6	22.4	36.6
Std	11.5	4.8	9.3	5.2	13.1	16.8	16.5	11.5	3.7	14.5
Min	14	5	15	12	13	19	21	21	19	24
Max	45	16	39	25	47	60	61	49	28	58

In summary, the level of improvement of the ionospheric-free combination, for both tropospheric models, reveals that the NOAA model is slightly more efficient in reducing the tropospheric errors than the Modified Hopfield model. When the corresponding mean

values and standard deviations of the improvement levels are compared with each other, it is clear that the mean values are higher when using the NOAA model. However, the standard deviations for the L1, L2, and WL observables are somewhat worse when using the NOAA model.

### *Scenario FL2*

This section gives the results in the observation domain for the scenario FL2, in which one more reference station is added into the FL1 network as shown in Figure 6.3. As expected, the level of improvement of both cases (i.e. the Modified Hopfield, and NOAA tropospheric models) shows very consistent results for the various observables. However, the improvement for FL2 when using the network and the NOAA correction is slightly lower than that for the FL1 network. One possible reason for this is that when MCD1 is analyzed, using a quality check program called TEQC provided by UNAVCO, Inc., this station had lower signal-to-noise ratio (SNR) measurements than any of the other reference stations. The SNR represents a measure of the quality of signals and typically the higher the SNR the more accurate GPS measurements will be. For all receiver formats which store the SNR in dBHz, the mapping of the SNR in dBHz to the RINEX SNR 0-9 flag is used. Figure 7.6 shows the RINEX SNR flag values for each elevation bin for scenario FL2 on September 3, 2003. All the reference stations except MCD1 had a RINEX SNR flag of over eight above 10 degrees elevation angle, while the SNR of MCD1 station has over 6.9 above the same elevation angle and has abnormal values during the day. This increased noise of MCD1 may be caused by the receiver itself due to

the random motion in thermal noise, by natural emissions, e.g., atmospheric radiation picked up by the antenna, or by interfering transmitters. Therefore, despite an additional reference station which is lower quality than any others, the station affects adversely on generation of the network correction.

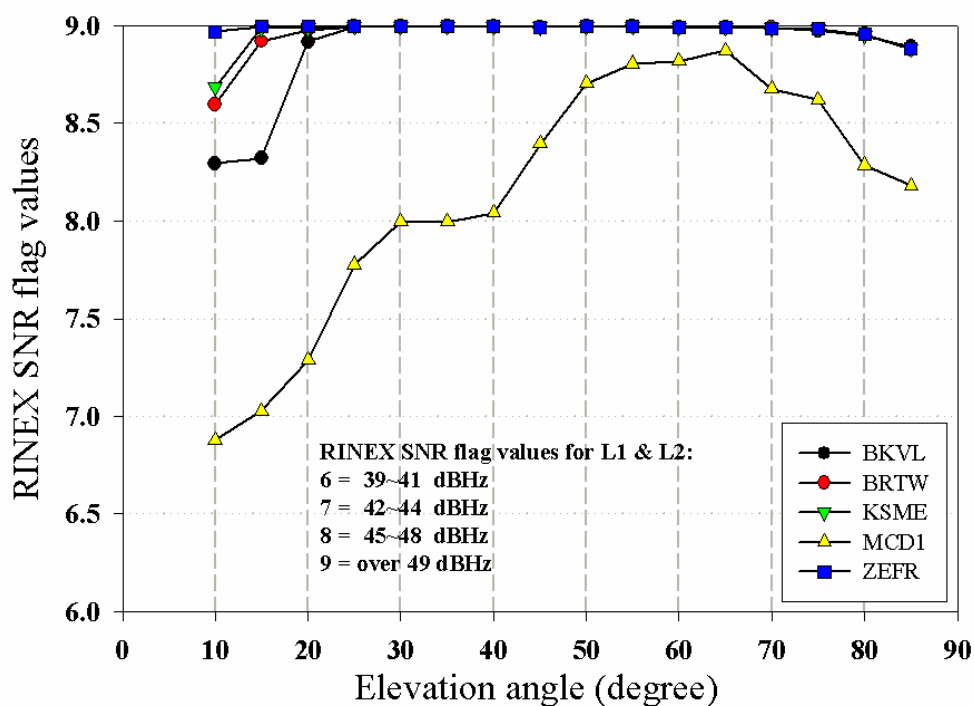


Figure 7.6: The RINEX SNR flag values for FL2 on 3 September 2003

Table 7.4 is a summary of the observation domain results for scenario FL2, on September 4, 2003. Similar to the FL1 scenario, the network approach is still somewhat effective in reducing the measurement errors for all observations, with levels of improvement ranging from 21% to 30%, with an average of about 27%, although the actual numerical improvement is in the mm range, as shown in Figure 7.7. The NOAA model also shows consistent improvement in this case, when combined with the network approach. Though

all observables, except for the ionospheric-free combination using the NOAA model, show worse performance than for the Modified Hopfield model, the ionospheric-free combination using the NOAA model shows very consistent performance whenever it is combined with the network approach. Since humidity was approximately 5% higher at MCD1 than at the other stations at the time of observations and the SNR had lower values as shown in Figure 7.6, this suggests that the addition of this corrupted station may affect the entire network correction generation.

Table 7.4: The level of improvement (%) of scenario FL2, on September 3, 2003

Improvement (%)		L1	L2	WL	IF	GF
Single baseline	NOAA	-5	-4	5	4	0
	M.Hop	30	30	24	21	28
Network (Corrected)	NOAA	26	23	13	21	18

Figure 7.7 shows the level of improvement for scenario FL2 on September 4, 2003 (the next day). Even though the first day of this scenario shows consistent improvement, relative improvements for the second day look quite low as is evident in Figure 7.7. As stated above, the MCD1 was noisier than any other reference stations used in this scenario which is the same as the previous day, shown in Figure 7.8. In addition, on September 4, 2003, the total number of the observations of MCD1 decreased about 20% relative to the previous day due to the loss of signal tracking.

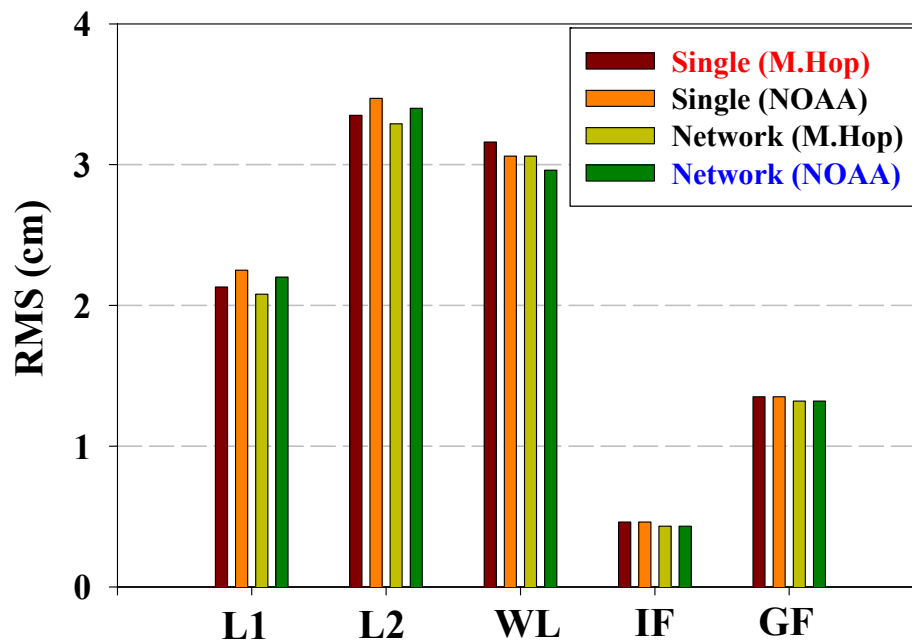


Figure 7.7: DD misclosures for FL2 scenario, 4 September 2003

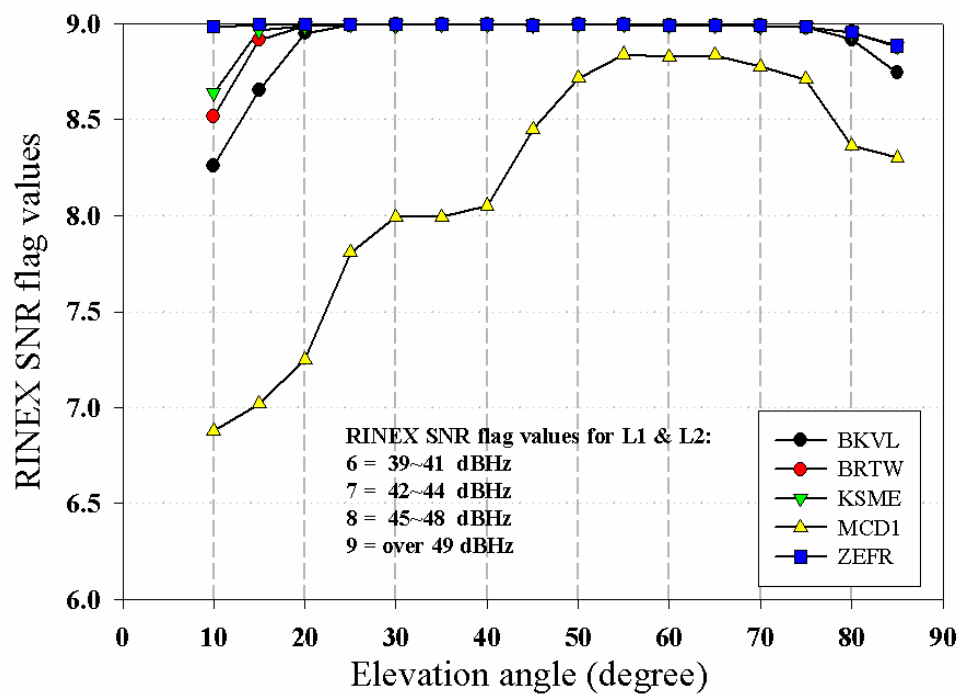


Figure 7.8: The RINEX SNR flag values for FL2 on 4 September 2003

In addition, when comparing the zenith wet delay estimates from the NOAA to those of the previous day, MCD1 shows more humidity on September 4 than on any of the neighboring days. Therefore, the errors contributing to this bias mentioned above are reflected in the measurement results from the FL2 network. Figure 7.9 shows the retrieved zenith wet delays by the NOAA model. Since the quality of MCD1 station is worse than any other stations as shown in Figure 7.8 and the station is much more humid than the previous day as shown in Figure 7.9, causing a loss of signal tracking for a few hours of the day, and an overall performance that is considerably degraded.

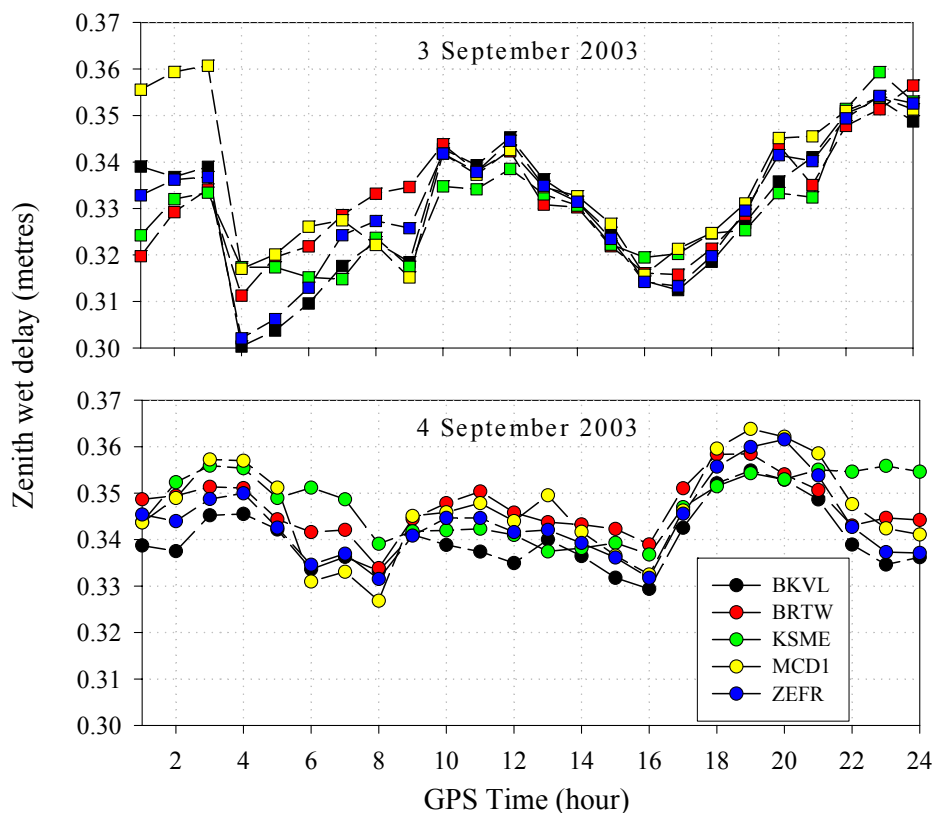


Figure 7.9: Retrieved NOAA real-time zenith wet delay for 3 and 4 September 2003 in the Florida region

Table 7.5 presents a summary of performance results for scenario FL2, on September 4, 2003. This Table shows that both approaches (i.e. single baseline vs. network approach) achieve little improvement, regardless of the observable used. In this case, the NOAA model does not show better performance than that of the Modified Hopfield model due to the problem discussed earlier.

Table 7.5: Percentage of improvement (%) relative to the single baseline approach by the modified Hopfield model for scenario FL2, 4 September 2003

Improvement (%)		L1	L2	WL	IF	GF
Single baseline	NOAA	-5	-4	3	0	0
	M.Hop	2	2	3	5	2
Network (Corrected)	NOAA	2	2	3	5	2

However, as shown in Figure 7.10, the overall performance over 5 days and two seasons shows that the network approach consistently reduces the errors, albeit by a small amount. This would translate into a position domain improvement. As to whether this improvement would be considered significant would depend on the application. However, given that in practice, an IF solution would be used given its superior performance, the position improvement would generally be at the level of a few mm, one can safely assume that it would generally be considered insignificant.

Adding one more station in the network does not always yield a significant improvement in GPS RTK performance, since this addition depends on the data quality and also on the location of the new reference station in the network. Alves et al. (2003) shows that, even

if one additional station is inserted into a network, the network approach may not yield better performance if the initial network configuration already has strong geometry.

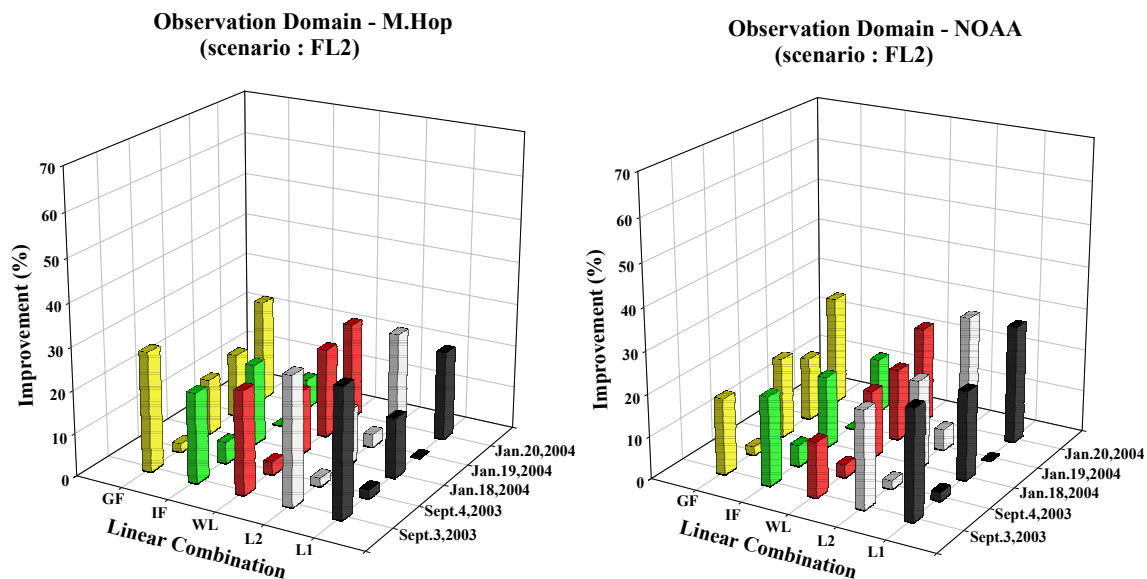


Figure 7.10: Levels of improvement in the observation domain results for scenario FL2, for five different observables, over five days in 2003 summer, and 2004 winter

Table 7.6 gives a summary of statistics of overall performance in terms of the percentage level of improvement, for scenario FL2 over the 5 days. It shows that the overall performance in using the network approach is effective in reducing the measurement errors, regardless of which tropospheric model is used. Both the mean values and standard deviations of the improvement via the NOAA model are somewhat better than those of the Modified Hopfield model, except for the wide-lane NOAA case where the ionospheric errors dominate the others. As is evident from this table, the standard deviations of the IF combination using the NOAA model show slightly better performance than that using the Modified Hopfield model. As described before, due to

the uncertainties related to the troposphere, especially near a weather front or stronger tropospheric disturbance, atmospheric changes are typically rapid. Under such severe weather conditions, it is more desirable to include or consider gradient effects or integrate the signal path using ray-tracing if one can access relevant information. Only in high-precision batch-type geodetic software are the gradient effects in the troposphere being considered, such as in: Bernese GPS software, GIPSY-OASIS, GAMIT, or OCCAM.

Table 7.6: Statistics of the overall performance in the level of improvement (%) for scenario FL2, over the five days

	Level of improvement (%) compared to the raw DD misclosure									
Model	The Modified Hopfield model					NOAA real-time tropospheric corrections				
Obs.	L1	L2	WL	IF	GF	L1	L2	WL	IF	GF
Mean	12.4	14.2	17.2	9.2	16.4	15.2	15.8	14.4	10.6	16.5
Std	14.1	12.2	8.6	11.0	10.1	13.7	11.5	7.3	9.6	8.8
Min	-5	2	3	-6	2	-1	2	3	-3	2
Max	30	30	24	21	28	28	28	23	21	26

Since the NOAA model is based on relatively advanced atmospheric physics, such gradient effects may be reflected in its generation. But one may lose this information by integrating vertically and then using a mathematical mapping function. The overall performance of the NOAA model in the Florida region, for all cases, is slightly better than that of the Modified Hopfield model.

### **7.1.2 North Carolina region**

As described in Section 6.2.2, each scenario is selected based on the same selection criteria as for the Florida region. In terms of the network size and spatial distribution, the North Carolina region is sparser than the Florida region. The average network size for Florida is less than 70 km, which is almost at the boundary for resolving ambiguities as integer values under very quiet ionospheric conditions; however, the average network size for North Carolina is over about 110 km, which is sparser, and the distance between the rover and the closest reference station is also longer than that in Florida. There are trade-offs in the error reduction for short baselines and long baselines. Typically, with an increase in differential errors, there is an increase in the spatial variation of the errors. Since this increased spatial variation can only be accurately measured with shorter reference station spacing, the reference stations must be spaced at short enough intervals to resolve the spatial frequencies of the errors. This requirement of being able to measure the atmospheric effects should be met, to ensure an optimal solution for the network approach. Therefore, even if some improvement from using the network approach is expected for the North Carolina scenarios, the level of improvement is expected to be less than for scenarios with shorter baselines (e.g. FL1 and FL2).

As with the previous scenarios, summaries of the performance results for each scenario are given separately, in the following sub-sections.

### *Scenario NC1*

Figure 7.11 gives an overall summary of the level of improvement in the observation domain results for the NC1 scenario, which is shown in Figure 6.4, for the 4 different cases, and for each observable: June 16, 2003; June 17, 2003; January 25, 2004; January 26, 2004; January 27, 2004. The overall performance shows that the network approach also achieves a relatively low but consistent error reduction for the longer North Carolina baselines when using the IF observables. Due to these longer baselines, as compared to the scenarios in Florida region, the level of improvement for NC1 is slightly less than those for FL1 and FL2. Therefore, to maximize the performance of the network approach, the reference stations would have to be located within the distance required for ambiguity resolution and better resolution of the atmospheric signal. In addition, the rover in NC1 is located outside the network, in which case it is expected that the correlated errors are not efficiently resolved.

As in previous figures, the left plot in Figure 7.11 shows the percentage level of improvement when using the Modified Hopfield tropospheric model, and the right panel shows the corresponding improvements for the NOAA model. The vertical axis gives the percentage improvements, the front horizontal axis shows five different observables, and the side horizontal axis gives the observation dates.

As we can see in Figure 7.11, both cases (i.e. the Modified Hopfield vs. NOAA model) show consistent improvement for each day by network approach, and the NOAA model

shows almost same performance than that of the Modified Hopfield model. Since the rover in NC1 is located outside the network as shown in Figure 6.4, the overall performance is not significant in this case.

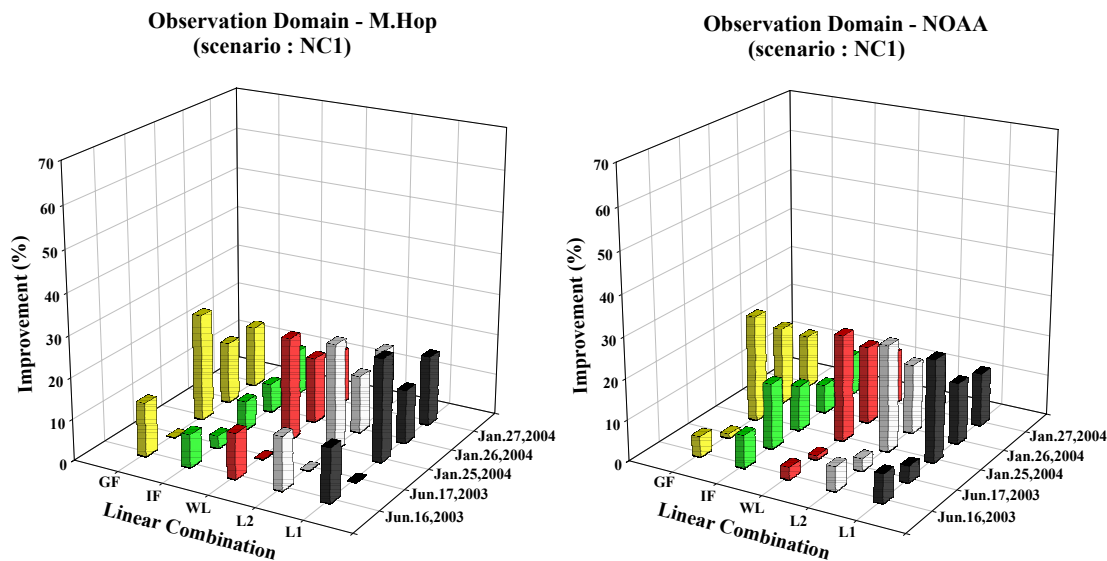


Figure 7.11: Levels of improvement in the observation domain results for scenario NC1, for five different observables, over five days in 2003 summer, and 2004 winter

Table 7.7 is a summary of the statistics in terms of the level of improvement (%) for both cases (i.e. the Modified Hopfield and the NOAA model). Regardless of which model is used, both are effective in reducing the measurement errors. The mean values and the standard deviations when using the NOAA model are slightly better than those of the Modified Hopfield model. Table 7.7 shows that the network approach is effective in reducing the effect of measurement errors on all observations, with mean improvement levels from 7% to 12%, with an average of 10 % when using the Modified Hopfield model, and ranging from 10% to 13%, with an average of 12%, when using the NOAA

model. On 17 June 2003, the improvement is quite low. A possible reason is that since the rover is located outside the network and the ionosphere effect is relatively high during that time as shown in Figure 7.12, the network correction may be overestimated at the rover, resulting in adverse effects on the network.

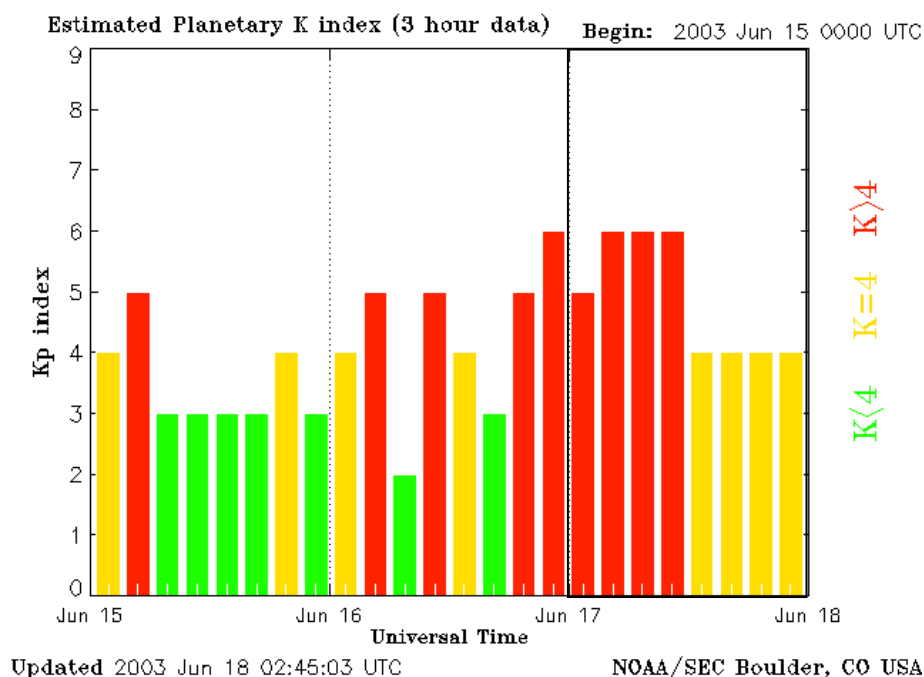


Figure 7.12: Kp index for 15~17 June 2003 (from NOAA 2005)

Table 7.7: Statistics of the overall performance in the level of improvement (%) for scenario NC1, over the five days

	Level of improvement (%) compared to the raw DD misclosure									
Model	The Modified Hopfield model					NOAA real-time tropospheric corrections				
Obs.	L1	L2	WL	IF	GF	L1	L2	WL	IF	GF
Mean	12.2	12.4	11.8	7.2	12.2	12.8	13	12.4	10.4	12.8
Std	11.7	12.0	11.3	2.8	12.3	8.1	9.2	10.5	3.5	10.2
Min	-7	-7	-6	3	-8	4	3	1	7	1
Max	25	26	25	11	26	25	26	26	16	26

### Scenario NC2

Figure 7.13 presents the overall summary of the scenario NC2. As described in Section 6.2.2, the main difference of NC2 compared to NC1 is that the NC1 rover, RALR, is located outside the network, but the NC2 rover, SNFD, is located inside the network; this suggests that the correlated errors will be mitigated more easily over time, and it is expected that the level of improvement would be better for NC2 than for NC1.

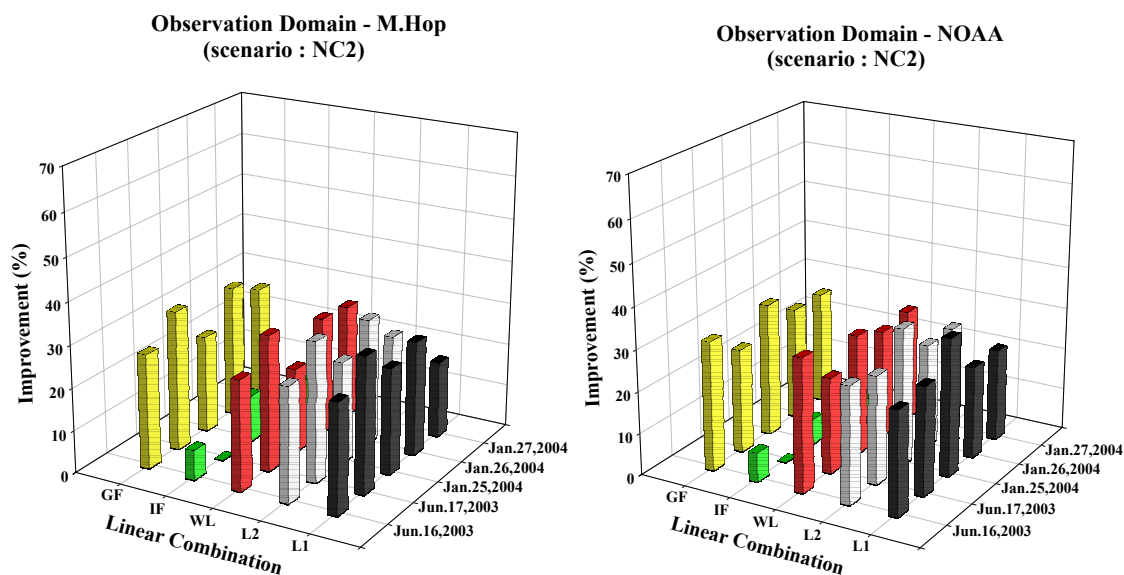


Figure 7.13: Levels of improvement in the observation domain results for scenario NC2, for five different observables, over five days in 2003 summer, and 2004 winter

Table 7.8 is a summary of the statistics of the NC2 scenario, and shows consistent levels of improvement, ranging from 2% to 28%, with an average of 22%, when using the Modified Hopfield model; and from 1% to 28%, with an average of 17%, when using the

NOAA model, which is better performance than for the NC1 scenario. As would be expected, the plots show that the network approach using multiple reference stations is consistent, in terms of the error reduction, over the 5 days, for both tropospheric models. Thus, it seems that to ensure a level of improvement which can be directly translated into a better positioning accuracy, additional reference stations should be placed at locations within the region to better model the spatially and temporally correlated errors.

Table 7.8: Statistics of the overall performance in the level of improvement (%) for scenario NC2, over the five days

	Level of improvement (%) compared to the raw DD misclosure									
Model	The Modified Hopfield model					NOAA real-time tropospheric corrections				
Freq.	L1	L2	WL	IF	GF	L1	L2	WL	IF	GF
Mean	25.6	27.2	26.6	2.2	28.2	25.6	27.4	27.4	1.2	28.4
Std	5.0	4.4	4.3	8.1	3.8	4.5	3.3	3.3	5.6	2.9
Min	18	22	20	-7	23	22	25	23	-6	25
Max	32	33	32	11	33	33	33	32	7	32

### 7.1.3 North Eastern region

As described in Section 6.2.2, each scenario is selected based on the same selection criteria as for previous scenarios. The chosen scenarios in the North Eastern region are sparser than those in the Florida region, but smaller than those in the North Carolina region. The average network size for this case is around 90 km, which is normally beyond the boundary size for resolving the ambiguities in a relatively short period of time as integer values for the network.

### Scenario NE1

This scenario is shown in Figure 6.6. Figure 7.14 presents the overall summary of the level of improvement in the observation domain results for four different cases, and five different observables over six days: August 1, 2003; August 2, 2003; August 3, 2003; June 7, 2003; June 8, 2003; June 9, 2003. The rover to be predicted in this case is located inside the reference station network, and the baseline length between the rover and the closest reference station is very short, which is useful to resolve ambiguities, and to measure the spatial variations of the atmospheric errors.

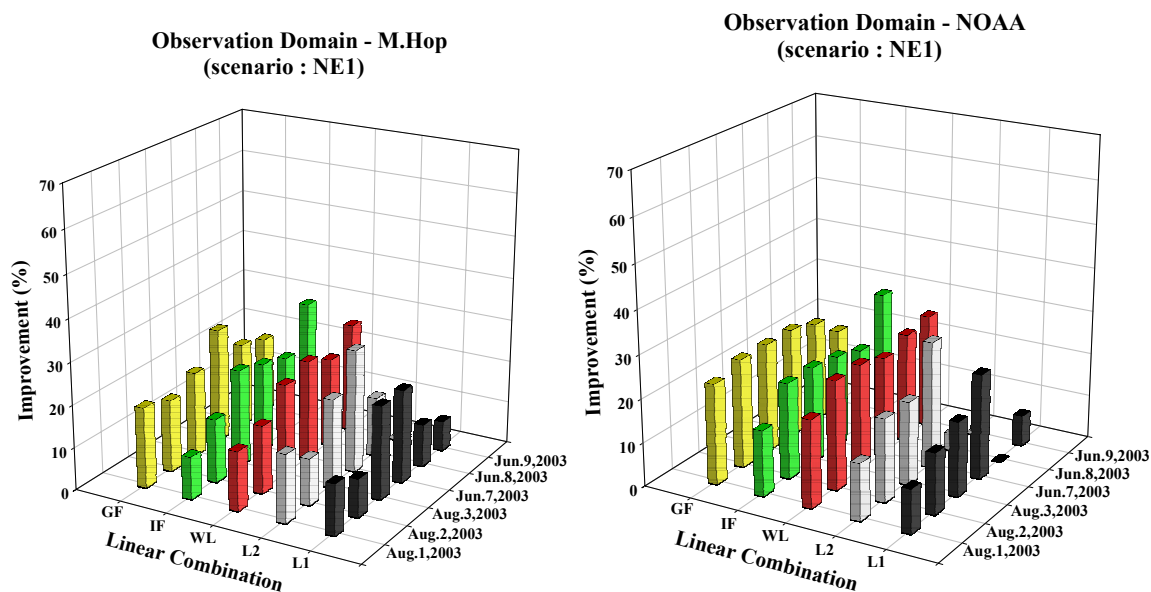


Figure 7.14: Levels of improvement in the observation domain results for scenario NE1, for four different cases and five different observables, over six days in 2003 summer and spring

Table 7.9 presents a summary of the statistics of scenario NE1, and shows consistent levels of improvement, ranging from 13% to 21%, with an average of 18%, when using the Modified Hopfield model, and from 11% to 24%, with an average of 19%, when using the NOAA model. As expected, the overall performance shows that the network approach consistently yields slightly better results. With an increase in differential errors, there is typically an increase in the spatial variation of the errors. As described before, this increased spatial variation can only be measured with shorter reference station spacing; that is, the environmental errors are a signal that should be sampled by the reference stations. Therefore, to measure the variations of the errors, the reference stations should be placed at short enough intervals to resolve their spatial variations. Table 7.9 shows that the NOAA model, when combined with the network approach, can significantly increase the level of improvement, showing better overall performance than that of the Modified Hopfield model.

Table 7.9: Statistics of the overall performance in the level of improvement (%) for scenario NE1, over the six days

	Level of improvement (%) compared to the raw DD misclosure									
Model	The Modified Hopfield model					NOAA real-time tropospheric corrections				
Obs.	L1	L2	WL	IF	GF	L1	L2	WL	IF	GF
Mean	13.6	15	20.5	19.5	20.1	10.8	13.8	24	21.3	23.2
Std	6.6	10.0	4.6	6.5	3.5	10.5	10.9	2.1	4.5	2.7
Min	7	-1	14	10	17	-7	-1	20	15	18
Max	22	29	26	29	27	24	29	26	29	25

### Scenario NE2

Figure 7.15 presents the overall summary of the results for scenario NE2. Similar to scenario NC1, the rover, which is a prediction point in the network approach, is located outside the network, which suggests that the correlated errors will be more reduced, and therefore it is expected that the level of improvement will be lower than for NE1.

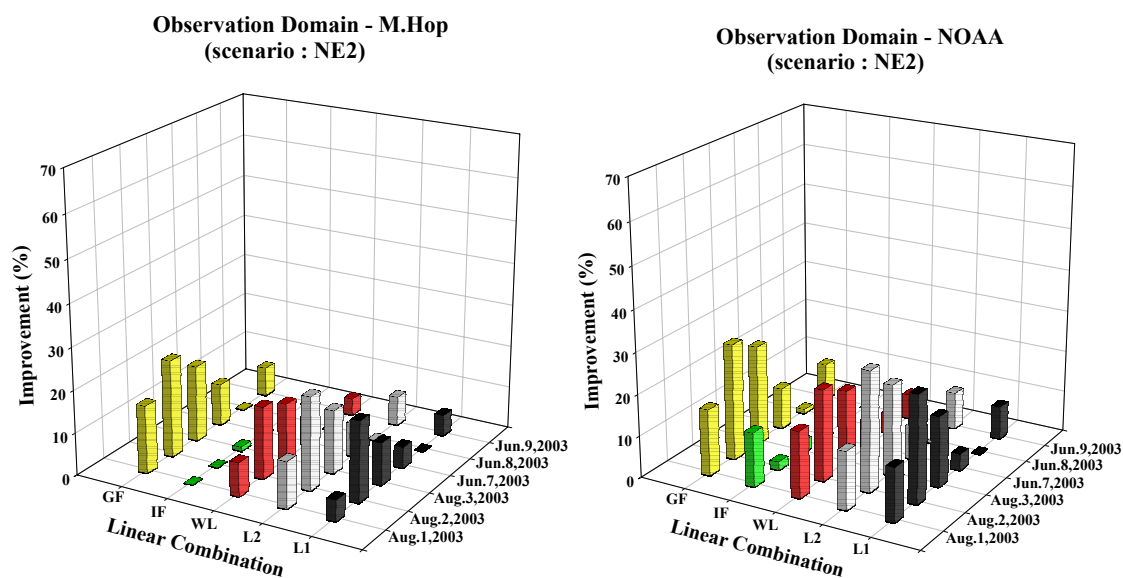


Figure 7.15: Levels of improvements in the observation domain results for scenario NE2, for four different cases and five different observables, over the 6 days in 2003 summer and spring

Table 7.10 presents a summary of the statistics, in terms of the percentage improvement, for scenario NE2 for all cases. The mean values of the NOAA model, for all observables, show better performance than those using the Modified Hopfield model. However, the

standard deviations of all cases using the NOAA model amplify slightly than those of the Modified Hopfield model.

Table 7.10: Statistics of the overall performance in the level of improvement (%) for scenario NE2, over the 6 days

	Level of improvement (%) compared to the raw DD misclosure									
Model	The Modified Hopfield model					NOAA real-time tropospheric corrections				
Freq.	L1	L2	WL	IF	GF	L1	L2	WL	IF	GF
Mean	5.8	9.3	8.3	-5.1	11.8	10.7	13.2	12.3	2.3	14.7
Std	9.0	9.6	6.2	5.1	9.2	10.5	11.3	7.2	6.9	10.1
Min	-9	-7	0	-13	-3	-4	-3	5	-6	1
Max	19	22	17	1	23	26	29	22	13	28

### *Summary*

Figure 7.16 represents the overall improvement in the observation domain results of all networks, for all observables, when using the Modified Hopfield tropospheric model; Figure 7.17 shows the corresponding improvements for the NOAA model. The grey blocks in Figures 7.16 and 7.17 correspond to the 95 percentile for each observable, and the solid line within each block gives the median, while the dashed line gives the mean improvement percentage. It is evident from both these figures that the network approach consistently shows a slight improvement for all three geographic regions (i.e., Florida, North Carolina, and the North Eastern region in the US) and all days tested, in terms of reducing the effect of the measurement errors on all observables, when using either the Modified Hopfield or the NOAA model for the troposphere.

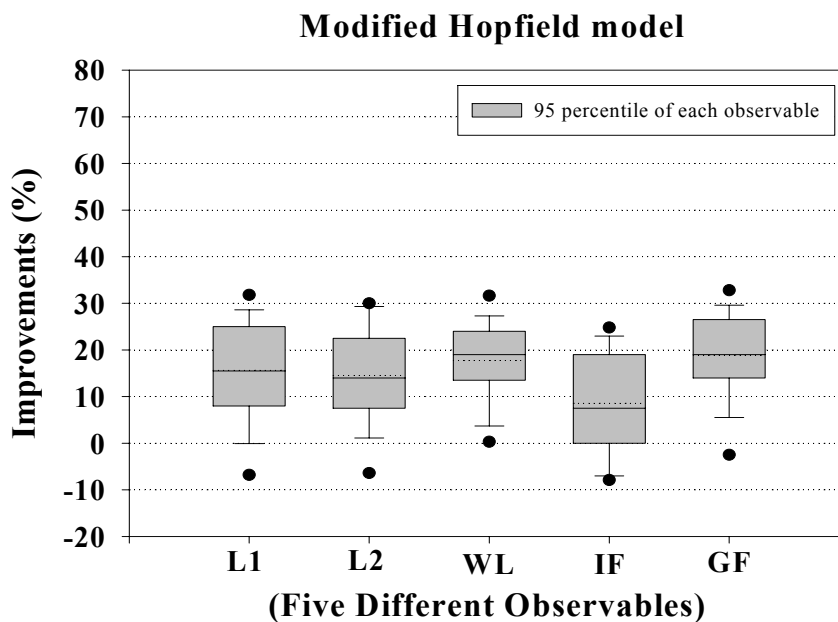


Figure 7.16: Summary of the levels of overall improvement for all scenarios, when using the Modified Hopfield tropospheric model.

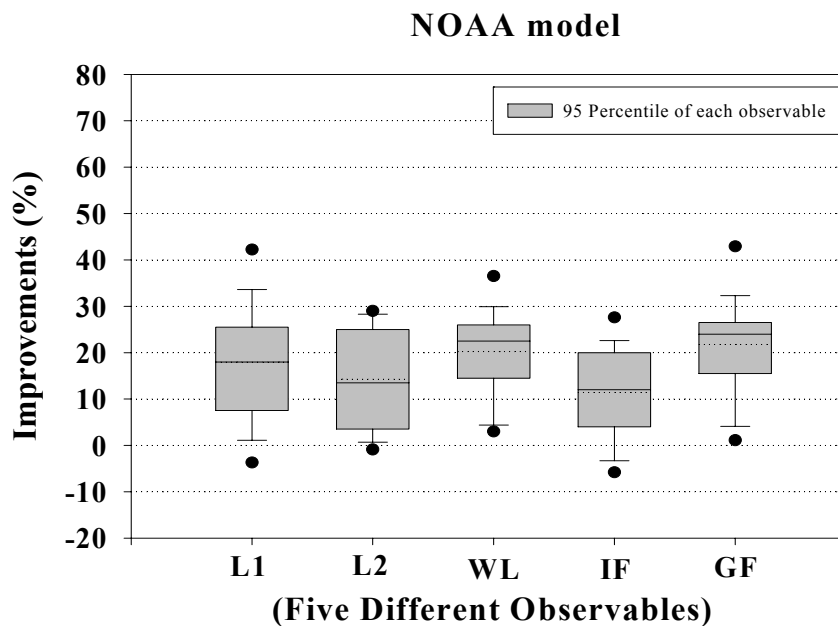


Figure 7.17: Summary of the levels of overall improvement for all scenarios, when using the NOAA tropospheric model

Table 7.11 is a summary of the statistics of the overall performance in the level of improvement (%) for the observation domain results for all scenarios, for both the Modified Hopfield and the NOAA tropospheric model. As is clear from Table 7.11, the overall performance improvement of the network approach is 10% for the IF observables, which is the most important. The improvement difference between the use of Modified Hopfield model and the use of NOAA corrections cannot be considered significant, based on these results.

Table 7.11: Statistics of the overall performance in the level of improvement (%) of the observation domain results for all scenarios, for both the Modified Hopfield and the NOAA model

	Level of improvement (%) compared to the raw DD misclosure									
Model	The Modified Hopfield model					NOAA real-time tropospheric corrections				
Obs.	L1	L2	WL	IF	GF	L1	L2	WL	IF	GF
Mean	15.7	14.6	17.8	8.6	18.9	18.0	19.7	20.2	11.4	21.8
Std	12.0	10.5	9.6	11.1	10.6	13.8	13.7	10.4	10.1	11.8
Min	-9	-7	-6	-13	-8	-7	-3	1	-6	1
Max	45	33	39	29	47	60	61	49	29	58

### ***Comparison between the Modified Hopfield model and NOAA model for FL1***

Figure 7.18 shows the difference of zenith hydrostatic delay and zenith wet delay between the NOAA model and the Modified Hopfield model of ZEFR station at Florida region on Sep. 3, 2003, suggesting that most of the differences are from the wet

component. Figure 7.19 represents the slant hydrostatic delay (SHD) and slant wet delay (SWD) for the Modified Hopfield model and for the NOAA model of ZEFR station at Florida region on Sep. 3, 2003. As expected, these plots show that there is significant difference between the wet delays of the two models. Last plot in the Figure 7.19 shows their differences with respect to the Modified Hopfield model. As described earlier, the NOAA model mostly improves the wet delay part, and is sensitive to the satellite elevation angle as shown in the figure.

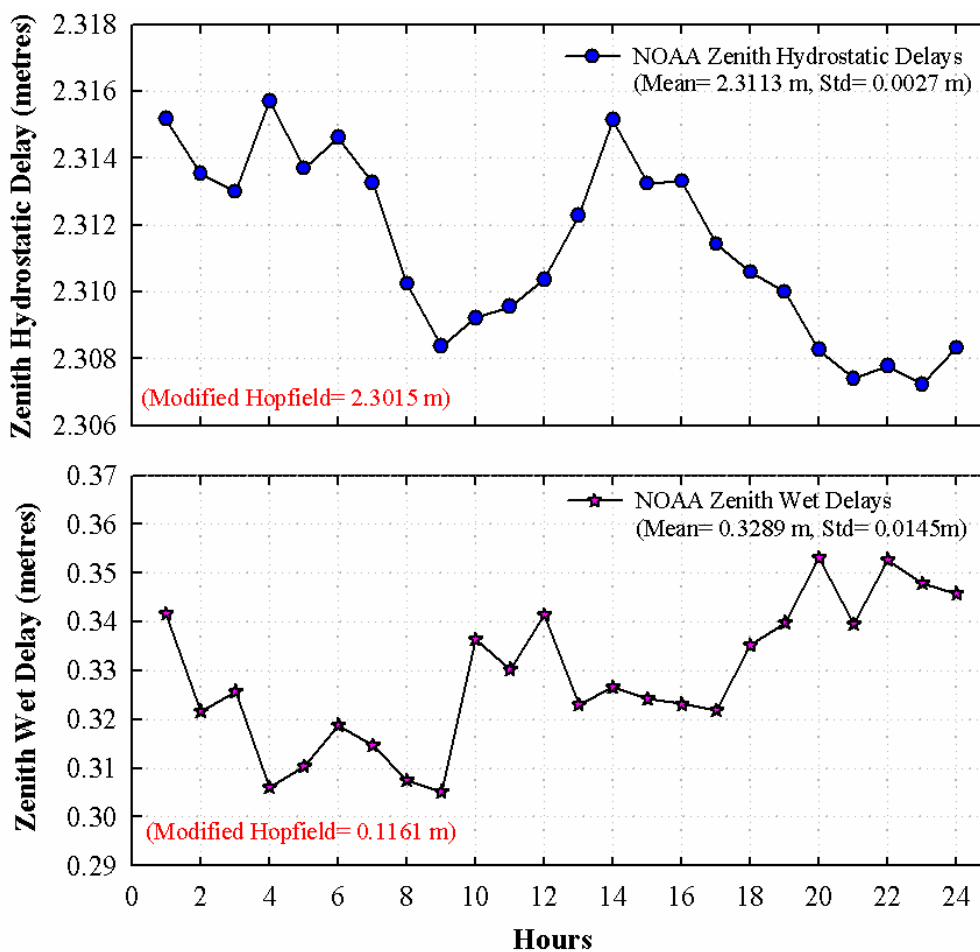


Figure 7.18: Zenith delays for the two tropospheric models

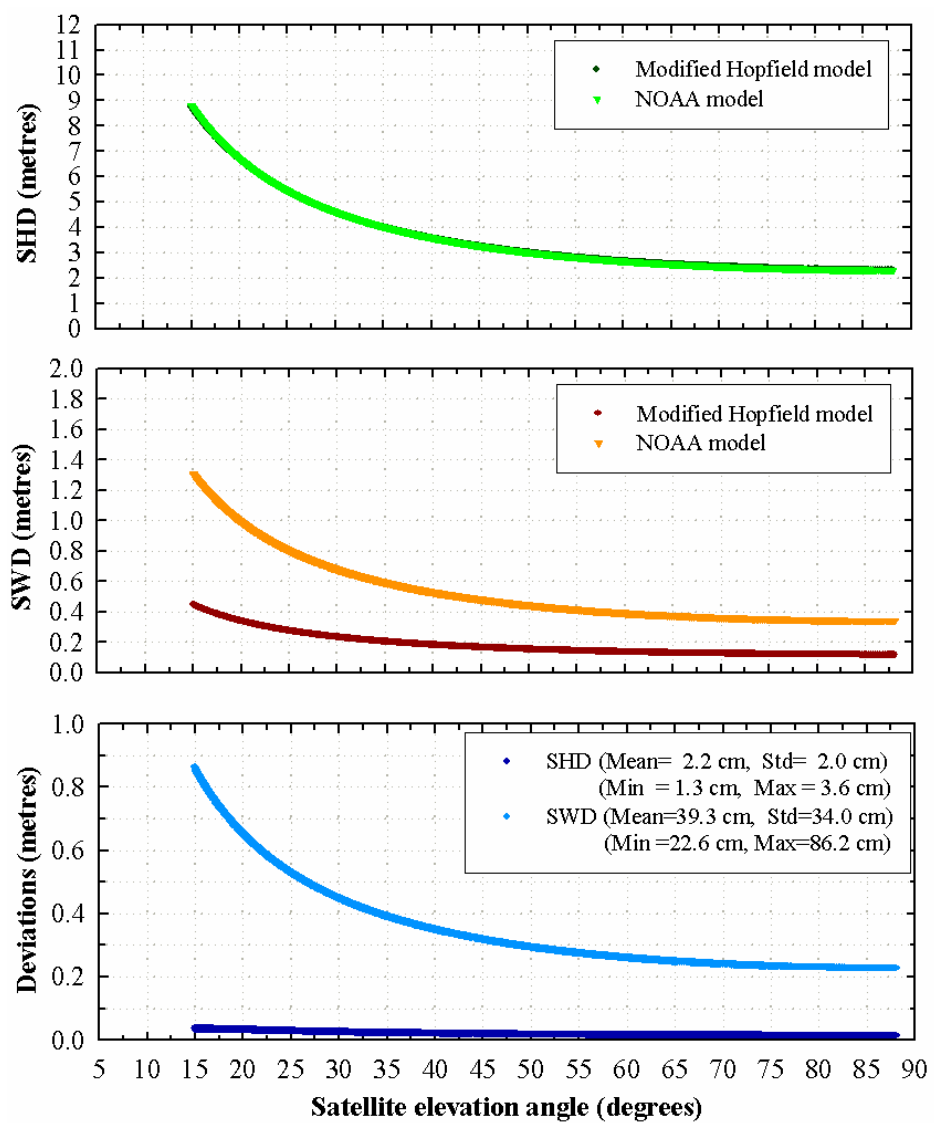


Figure 7.19: Slant delays for the two tropospheric models

## 7.2 Results of the Multiple Reference Stations Approach using Ray-tracing

Since RUC20 provides basic parameters for ray-tracing, e.g. pressure, geopotential height, relative humidity, and temperature, the refractivity for each of the hydrostatic and wet components can be estimated for each pressure level, using Equation (6.1).

A test of the ray-tracing was performed for the scenario FL1 in the Florida region, on September 3, 2003 since this network is relatively more humid than the other regions and the additional station, called MCD1, which is noisier as discussed before, does not need to be considered. The ZEFR station is used as a rover, and three reference stations, BKVL, BRTW, and KSME, are used to generate network corrections, as described in Section 6.2.1. In order to use ray-tracing, the parameters to be supplied to the ray-tracing should be estimated for each of the reference stations. However, since RUC20 has parameters only for the defined grids, we still need the parameters to be interpolated to the desired location. For this test, linear interpolation is horizontally performed, but not vertically. In addition, the RUC20 grid being considered has 37 isobaric levels up to 100 hPa, which is sufficient to model the hydrostatic component to the desired precision. However, the wet component is much more sensitive to variations than the hydrostatic component, and it is not sufficient for the hydrostatic component to use isobaric levels up to 100 hPa. Therefore, after the interpolation to get the parameters for the desired locations, using the nearest 4 horizontal grid points defined in RUC20, and then the retrieval of the wet refractivity for those locations for each pressure layer, the remaining

hydrostatic refractivity is extrapolated, and then these extrapolated values are used to calculate the range delays for the corresponding reference stations.

Based on the estimated parameters, e.g., total refractivity  $N$ , modified refractivity  $M$ , temperature, potential temperature, and specific humidity for the ZEFR station, the refractivities for wet and hydrostatic component were calculated. Figure 7.20 shows the wet and hydrostatic refractivity and refractivity index estimated for each of the pressure levels on 3 September 2003 for an hour. The vertical axis gives the geopotential heights and the horizontal axis the corresponding refractivity.

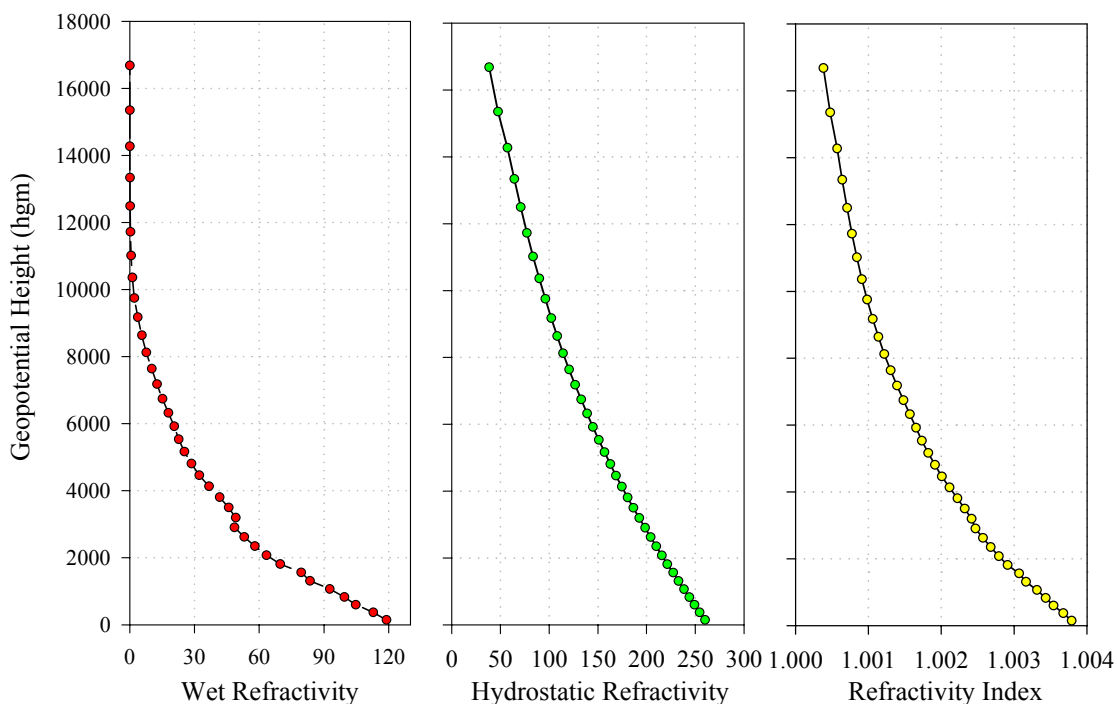


Figure 7.20: Refractivity and refractivity index for the ray-tracing at ZEFR location on 3 September 2003

The delay calculated by the ray-tracing is replaced of the NOAA model for elevation angles less than 10 degrees. As seen in Table 6.4, the overall mask angle for the ray-tracing of five degrees are used since all the receivers involved in FL1 were only recorded over five degrees cutoff angle. While there is no big difference for the hydrostatic component between NOAA model and ray-tracing value, the difference of the wet component is prominent. Figure 7.21 represents the slant wet delays of the ray-tracing at ZEFR location on 3 September 2003. To get slant delays, Neill mapping function is also used for NOAA model.

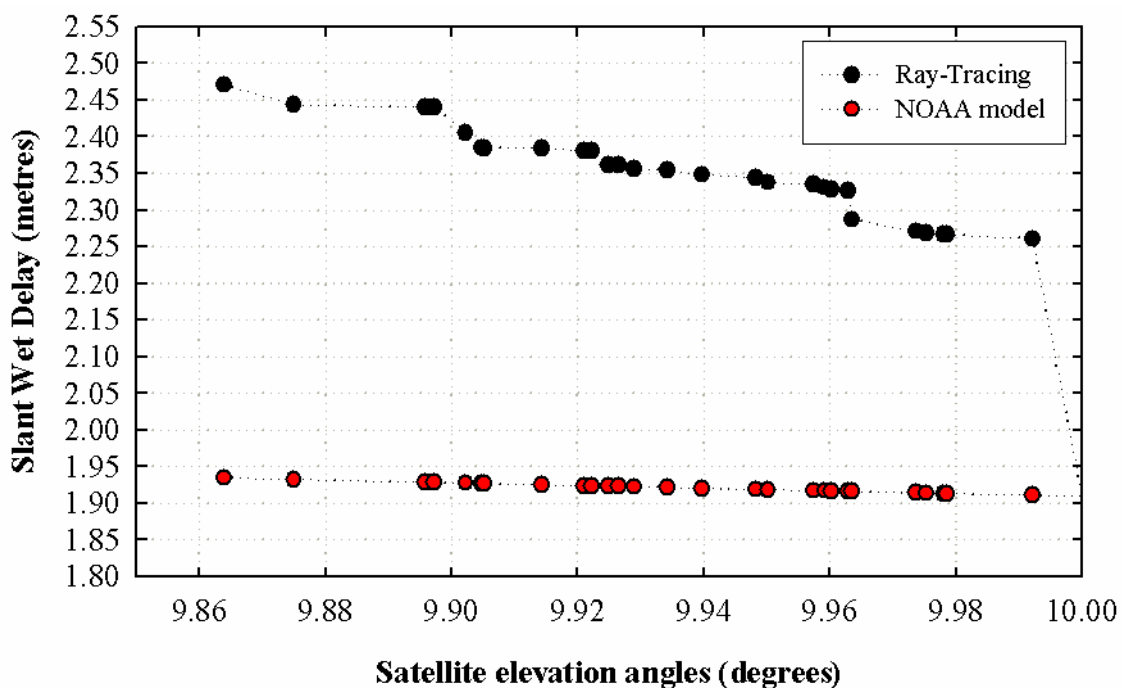


Figure 7.21: Slant wet delay of the ray-tracing at ZEFR location on 3 September 2003.

The ray-tracing is only applied for elevation angle below 10 degrees.

The ray-tracing is only applied for elevation angle below 10 degrees since the performance is dramatically degraded when the ray-tracing is applied entire elevation

angle. Since there are not many data below 10 degrees, the impact of the misclosures are small.

Table 7.12 is a summary of the combined results in the observation domain for the ray-tracing test. Since there are only few satellites available below 10 degrees, the result is shown for entire 24 hours to see the impact of the ray-tracing, instead of showing the difference of misclosures below 10 degrees. From this Table 7.12, even though the performance improvement is quite small, the ray-tracing when combined with the NOAA model at low elevation shows relatively better performance than that of the NOAA model only.

Table 7.12: Overall performance in the level of improvement (%) in the ray-tracing test for scenario FL1 on 3 September 2003 with respect to the network approach by the NOAA model

	NOAA model	Ray-tracing and NOAA model	Improvement (%)
L1	39.3	39.5	0.4
L2	41.7	41.9	0.4
WL	33.9	34.1	0.5
IF	20.6	20.9	1.2
GF	41.1	41.3	0.5

## **CHAPTER 8**

### **CONCLUSIONS AND RECOMMENDATIONS**

#### **8.1 Conclusions**

The main objective in this thesis was to evaluate the network approach, MultiRef™, developed by the University of Calgary, together with NOAA-derived and independently modeled tropospheric corrections, as applied to three geographic regions: Florida, North Carolina, and the North Eastern regions, within the NGS CORS network in the USA. In the analysis, either the NOAA or the Modified Hopfield tropospheric delay model was used for assessing GPS RTK performance. The evaluations were performed over periods of up to three consecutive days, for each of two seasons in 2003 and 2004, these days being chosen at times when the tropospheric effect was deemed relatively large. A total of six scenarios were evaluated and double difference misclosures for five different types of observables were used as a performance measure: the original L1 and L2 observables, the wide-lane linear combination, the ionospheric-free linear combination, and the geometry-free linear combination. A second thesis objective was to assess and compare the results, in terms of the level of improvement in the observation domain, from an analysis where a ray-tracing technique was used for the tropospheric delay model. This approach, based on RUC20 raw data, was only applied when the satellite elevation angle was below 10 degrees.

The analysis of the results presented in this thesis leads to the following conclusions:

- The overall level of performance for the three chosen geographical regions demonstrated that the network approach succeeded in making consistent improvements in reducing the effect of measurement errors on all observables, for both the Modified Hopfield and NOAA tropospheric delay models. The mean value of the level of improvement was consistently in the range of 9% to 22%.
- The level of performance of the ionospheric-free observables, the ones that are important for positioning and good measures of the residual tropospheric or orbital errors, revealed that the NOAA model was about 3% more effective than the Modified Hopfield model in terms of reducing the tropospheric errors. Therefore, although the tropospheric uncertainty, arising mainly in the wet component, is the ultimate limiting factor for high-accuracy GPS RTK positioning, this effect may be minimized when the NOAA model are combined with the network approach. However, no significant difference could be found between the Modified Hopfield and NOAA tropospheric delay models for GPS RTK performance, either for the single reference station or for the network approach.
- The ray-tracing technique studied herein showed slightly better performance than that of the NOAA model used alone (i.e., without any help from the ray-tracing).

- As a cautionary note, these results are valid for the reference station densities of the six scenarios evaluated herein, and may not necessarily apply to shorter or longer inter-station distances.

## **8.2 Recommendations**

The research presented in this thesis has shown that the network approach, as tested for various scenarios in the NGS CORS network, is beneficial in reducing the correlated errors. Also, the NOAA tropospheric delay model showed consistent but minor improvements in reducing the tropospheric effects. Based on this research, the following recommendations for future work may be made:

- Further tests on networks with other inter-station distances and a yet wider range of ionospheric and tropospheric conditions are required. The latter is most important to further assess the effect of the interplay between both atmospheric effects on their modeling and position accuracy. As this work showed little difference in the performances of the two tropospheric delay models in making corrections over the baseline distances evaluated herein, future studies of sparser networks may be required to more clearly see the relative performances of these tropospheric models.
- Investigation of the elimination of higher-order ionospheric effects is required. Even though the ionospheric-free linear combination eliminates the first-order

ionospheric effect, the higher-order effects may still marginally affect the final solution.

- Further investigation is required into the simultaneous improvement of both the positioning accuracy, and of the ability to resolve ambiguities faster, building on the positive results demonstrated by the reduction of the measurement errors in this work -- which can already be directly translated into positioning and ambiguity domain improvements.
- Evaluate the effect of introducing a new carrier frequency from GPS modernization or Galileo. If this new (unencrypted) frequency is made available, the corresponding measurement should be more precise than the L2 measurement, resulting in better resolution of the ionospheric errors and multipath which will make it easier to reduce the residual tropospheric errors.

## REFERENCES

- Alves, P., G. Lachapelle, M. E. Cannon, J. Liu, and B. Townsend (2001) Evaluation of Multiple-Reference DGPS RTK Using a Large Scale Network, *Proceedings of ION National Technical Meeting*, Long Beach, USA, pp. 665-671.
- Alves, P., Y.W. Ahn., and G. Lachapelle (2003) "The Effects of Network Geometry on Network RTK Using Simulated GPS Data", *Proceeding of ION GPS*, Portland, USA, pp. 1417-1427.
- Alves, P., Y.W. Ahn, J. Liu, G. Lachapelle, D. Wolfe, and A. Cleveland (2004a) Improvements of USCG RTK Positioning Performance Using External NOAA Tropospheric Corrections Integrated with a Multiple Reference Station Approach. *Proceedings of ION National Technical Meeting*, San Diego, USA, pp. 689-698.
- Alves, P., G. Lachapelle, and M.E. Cannon (2004b) In-Receiver Multiple Reference Station RTK Solution, *Proceedings of ION GPS*, Long Beach, USA, pp. 2840-2848.
- Alves, P. (2004c) *Development of two novel carrier phase-based methods for multiple Reference station positioning*. PhD Thesis, UCGE Report Number 20203, The University of Calgary.
- ARM (2004) Rapid Update Cycle (RUC) Model Data. webpage.  
URL <http://www.arm.gov/xds/static/ruc.stm>

- Baby, H.B., P. Gole and J. Lavergnat (1988) A model for the tropospheric excess path length of radio waves from surface meteorological measurements, *Radio Science*, Vol. 23, No. 6, pp. 1023-1038.
- Baltink, H.K., H. van der Marel and A.G.A. van der Hoeven (2002) Integrated atmosphere water vapor estimates from a regional GPS network, *Journal of Geophysical Research*, Vol.107, No.D3.
- Bassiri S. and G. A. Hajj (1993) Higher-order ionospheric effects on the Global Positioning System observables and means of modeling them. *Manuscripta geodaetica*, Vol.18, pp. 280-289.
- Bauersima, I. (1983) *NAVSTAR/Global Positioning System (GPS) II*, Astronomical Institute, University Berne, Switzerland.
- Behrend, D., L. Cucurull, E. Cardellach, A. Rius, M.J. Sedo, and A. Nothnagel (2001) The Use of NWP Products in Near Real-Time GPS Data Processing. *In Proceedings of ION GPS*, Salt Lake City, USA, pp. 2499-2506.
- Beutler, G., E. Brockmann, W. Gurtner, U. Hugentobler, L. Mervart, and M. Rothacher (1994) Extended Orbit Modeling Techniques at the CODE Processing Center of the International GPS Services for Geodynamics (IGS) : Theory and Initial Results, *Manuscripta Geodetica*, Vol.19, pp.367-386.
- Black, H. D., (1978) An easily implemented algorithm for the tropospheric range correction, *Journal of Geophysical Research*, Vol.83, No.B4, pp. 1825-1828.
- Boehm, J. and H. Schuh (2003) Vienna Mapping Functions, *16<sup>th</sup> Working Meeting on European VLBI for Geodesy and Astrometry*, Leipzig, pp. 131-143.

- Brevis, M, S. Brusinger, T.A. Herring, C. Rocken, R.A. Anthes, and R.H. Ware (1992) GPS meteorology : Remote sensing of atmospheric water vapor using the Global Positioning System, *Journal of Geophysical Research*, Vol, 97, No. D14, pp. 15787-15801.
- Cannon, M.E., G. Lachapelle, P. Alves, L.P Fortes. and B. Townsend (2001) GPS RTK Positioning Using a Regional Reference Network: Theory and Results, *Proceedings of the Fifth GNSS International Symposium*, Seville, USA.
- Cannon, M.E., G. Lachapelle, Y.W. Ahn, P. Alves, P. Lian, J. Liu, A. Morton, M. Petovello and J. Schleppe (2004) Improving the Existing USCG DGPS Service: Analysis of Potential System Upgrades and Their Effect on Accuracy, Reliability and Integrity. *Report prepared for the United States Coast Guard*, Portsmouth, VA, USA.
- Cappellari, J.O., C.E. Velez, and A.J. Fuchs (1976) Mathematical Theory of the Goddard Trajectory Determination System, *Technical Report X-582-76-77*, Goddard Space Flight Center.
- Chao, C. C. (1972) A model for tropospheric calibration from daily surface and radiosonde ballon measurement, *JPL Publication*, Pasadena, California, p.16.
- Dao, D., P. Alves and G. Lachapelle (2004) Performance Evaluation of Multiple Reference Station GPS RTK for a Medium Scaled Network. *Proceedings of the International Symposium on GPS/GNSS*, Sydney, Australia, 15 pages.
- Davis, J.L., T.A. Herring, I.I. Sharpiro, A.E.E. Rogers, and G. Elgerred (1985) Geodesy by radio interferometry: Effects of atmospheric modeling errors on estimates of baseline length, *Radio Science*, Vol. 20, No. 6, pp. 1593-1607.

- Dousa, J. (2001) The Impact of Ultra-Rapid Orbits on Precipitable Water Vapor Estimation Using Ground GPS Network, *Physics and Chemistry of the Earth(A)*, Vol.26, No.6-8, pp. 393-398.
- Elgered, G. (1993) *Tropospheric radio-path delay fromground-based microwave-radiometry. AtmosphericRemote Sensing by Microwave Radiometry*, M.Janssen, Ed., Wiley & Sons, pp. 215–258.
- Escobal, P. R. (1976) *Methods of Orbit Determination*, John Wiley & Sons, New York.
- Essen, L., and K. D. Froome (1951) The refractive indices and dielectric constants of air and its principal constituents at 24,000 Mc/s. *Proceedings of the Royal Society B*, Vol.64, pp. 862-875.
- Folopoulos, G. and M. Cannon (2000) Investigation of the Spatial Decorrelation of GPS Carrier Phase Errors Using a Regional Reference Station Network. *Proceedings of the World Congress of International Association*, San Diego, USA.
- Fortes, L. P., M. E. Cannon, and G. Lachapelle (2000a) Testing a Multi-Reference GPS Station Network for OTF Positioning in Brazil, *Proceedings ION GPS*, Salt Lake City, USA, pp. 1133-1142.
- Fortes, L. P., G. Lachapelle, M. E. Cannon, S. Ryan, G. Marceau, S. Wee, and J. Raquet (2000b) Use of a Multi-Reference GPS Station Network For Precise 3D Positioning in Constricted Waterways, *International Hydrographic Review*, Vol.1(1), pp. 15-29.
- Fortes, L. P., M. E. Cannon, S. Skone, and G. Lachapelle (2001) Improving a Multi-Reference GPS Station Network Method for OTF Positioning in the St. Lawrence Seaway, *Proceedings of ION GPS*, Salt Lake City, USA, pp. 404-414.

- Goad, C. C., and Goodman, L., 1974, A modified Hopfield tropospheric refraction correction model, *The American Geophysical Union*, CA, USA, 28 pages.
- Gutman S.I. and S.G. Benjamin (2001) The role of Ground-Based GPS Meteorological Observations in Numerical Weather Prediction. *GPS Solutions, Special issue for IGS Analysis Center Workshop 2000*, 10 pages.
- Gutman, S., T. Fuller-Rowell and D. Robinson (2003) Using NOAA Atmospheric Models to Improve Ionospheric and Tropospheric Corrections, *U.S. Coast Guard Differential GPS Symposium, June 2003, Portsmouth, USA* ([http://www.gpsmet.noaa.gov/jsp/downloads/NOAA\\_Atmospheric\\_Corrections.pdf](http://www.gpsmet.noaa.gov/jsp/downloads/NOAA_Atmospheric_Corrections.pdf)).
- Herring, T. A. (1992) Modeling atmospheric delays in the analysis of space geodetic data, *Proceedings of the Symposium on Refraction of Transatmospheric Signal in Geodesy*, Netherlands, Vol.36, pp. 157-164.
- Hofmann-Wellenhof. B., H. Lichtenegger and J. Collins (1998) *GPS Theory and Practice*. 4th Ed., Springer-Verlag, New York.
- Hopfield, H. S. (1969) Two quartic tropospheric refractivity profile for correcting satellite data, *Journal of Geophysical Research*, Vol.74, No.18, pp. 4487-4499.
- Hugentobler, U., S. Schaer and P. Fridez (2001) *Bernese GPS Software Version 4.2*, *Astronomical Institute*, University Berne, Switzerland.
- IGS (2004) IGS Tracking Network. webpage.  
URL <http://igs.cb.jpl.nasa.gov/network/netindex.html>

- Jensen, A.B.O. (2002) *Numerical Weather Prediction for Network RTK*. PhD Thesis, University of Copenhagen, Publication Series 4, Vol. 10, National Survey and Cadastre, Denmark.
- Jensen, A.B.O. (2004) Private Conversation.
- Klobuchar, J. (1996) *Global Positioning System: Theory and Applications*, Progress in Astronautics and Aeronautics, Vol.163, pp. 485-515.
- Kruse, L.P., B. Sierk, T. Springer, and M. Cocard (1999) GPS-meteorology : Impact of predicted orbits on precipitable water estimates, *Geophysical Research Letter*, Vol.26, pp. 2045-2048.
- Lachapelle, G., B. Townsend, P. Alves, L.P. Fortes, and M.E. Cannon (2000) RTK Positioning Using a Reference Network. *Proceedings of ION GPS*, Alexandria, VA, USA, pp. 1165-1171.
- Leick, A. (1995) *GPS Satellite Surveying*, 2<sup>nd</sup> Ed. John Wiley & Sons, New York.
- Liu, J. (2003) *Implementation and Analysis of GPS Ambiguity Resolution Strategies in Single and Multiple Reference Station Scenarios*, MSc Thesis, UCGE Report Number 20168, University of Calgary.
- Luo, N. (2001) *Precise Relative Positioning of Multiple Moving Platforms Using GPS Carrier Phase Observables*. PhD Thesis, UCGE Report Number 20147, University of Calgary.
- Marini, J. W. (1972) Correction of satellite tracking data for arbitrary tropospheric profile, *Radio Science*, Vol.7, No.2, pp. 223-231.

Mendes, V.B. and R.B. Langley (1994a) Modeling the tropospheric delay from meteorological surface measurements: comparison of models, *American Geophysical Union*.

Mendes, V.B. and R.B. Langley (1994b) A Comprehensive Analysis of Mapping Functions Used in Modeling Tropospheric propagation Delay in Space Geodetic Data, *Proceedings of KIS94*, Banff, Canada, pp. 87-98.

Mendes, V.B. and R.B. Langley (1995) Zenith Wet Tropospheric Delay Determination Using Prediction Model: Accuracy Analysis, *Cartografia e Cadastro*, Vol.2, pp. 41-47.

Montenbruck, O. and E. Gill (2000) *Satellite Orbits: Models, Methods, and Applications*, Springer-Verlag, New York.

Niell, A. E. (1996) Global mapping functions for the atmosphere delay at radio wavelengths, *Journal of Geophysical Research*, Vol.101, No.B2, pp. 3227-3246.

NGS (2004) CORS-Continuously Operating Reference Stations. webpage

URL <http://www.ngs.noaa.gov/CORS/>

NOAA (2001) NOAA/FSL Ground-Based GPS Integrated Precipitable Water Vapor Real Time Water Vapor Interface. webpage.

URL <http://www.gpsmet.noaa.gov/realtimeview/jsp/rti.jsp>

NOAA (2004) NOAA/FSL Ground-Based GPS Meteorology (GPS-Met). webpage.

URL <http://gpsmet2.fsl.noaa.gov/jsp/index.jsp>

NOAA (2005) Space Environment Center. webpage.

URL <http://www.sec.noaa.gov>

Pany, T., P. Peseq, and G. Stangl (2001) Elimination of Tropospheric Path Delays in GPS Observations with the ECMWF Numerical Weather Model. *Physics and Chemistry of the Earth(A)*, Vol.26, No.6-8, pp. 487-492.

Petrovski, I., S. Kawaguchi, H. Torimoto, B. Townsend, S. Hatsumoto, K. Fuji (2002) An Impact of High Ionospheric Activity on MultiRef RTK Network Performance in Japan, *Proceedings of ION GPS, Portland, USA*, pp.2247-2255.

Raquet, J. (1998) *Development of a Method for Kinematic GPS Carrier-Phase Ambiguity Resolution Using Multiple Reference Receivers*. PhD Thesis, UCGE Report Number 20116, University of Calgary.

Raquet, J., G. Lachapelle, and T. E. Melgard (1998) Test of a 400 km x 600 km Network of Reference Receivers for Precise Kinematic Carrier-Phase Positioning in Norway, *Proceedings of ION National Technical Meeting, Nashville, USA*, pp. 407-416.

Raquet, J., and G. Lachapelle (2000) Development and Testing of a Kinematic Carrier-Phase Ambiguity Resolution Method Using a Reference Receiver Network. *Navigation, The Institute of Navigation, Alexandria, VA, USA*, Vol.46, No.4, 283-295.

Remondi, B. W. (1984) *Using the Global Positioning System (GPS) phase observable for relative geodesy: modeling, processing, and results*, PhD Thesis, University of Texas at Austin.

Rocken, C., T.V. Hove and R. Ware (1997) Near real-time GPS sensing of atmospheric water vapor, *Geophysical Research Letter*, Vol. 24, No.24, pp. 3221-3224.

- Rothacher, M. and G. Beutler (2002), *Advanced Aspects of Satellite Positioning*, Lecture Notes of ENGO 699.80, University of Calgary.
- Rothacher, M., B. Beutler, E. Brockmann, S. Fankhauser, W. Gurtner, T. Springer, S. Botton, L. Mervart, A. Wiget, U. Wild (1992) Results of the Center for Orbit Determination in Europe, *Proceeding of the 7th International Symposium on Geodesy and Physics of the Earth*.
- Rothacher, M., T.A. Springer, S. Schaer, and G. Beutler (1997) Processing Strategies for Regional GPS Networks, *Proceedings of the IAG General Assembly in Rio*, Springer.
- Saastamoinen, J. (1972) Atmospheric correction for troposphere and stratosphere in radio ranging of satellites, Geophysical monograph, 15, *American Geophysical Union*, Washington, D. C., USA, pp. 247-252.
- Schaer, S. (1999) Mapping and Predicting the Earth's Ionosphere Using the Global Positioning System. *Geodatisch-geophysikalische Arbeiten in der Schweiz*, Vol.59, Schweizerische Geodatische Kommission.
- Schuler, T. (2001) *On Ground-Based GPS Tropospheric Delay Estimation*, PhD Thesis, University of Munchen.
- Skone, S. (1998) *Wide Area Ionospheric Grid Modelling in the Auroral Region*, PhD Thesis, University of Calgary.
- Skone, S. (2003) Atmospheric Effect on Satellite Navigation, Lecture Notes of ENGO 633, University of Calgary.
- Taff, L. G. (1985) *Celestial Mechanics*, John Wiley & Sons, New York.

- Thayer, G. D. (1974) An improved equation for the radio refractive index of air, *Radio Science*, Vol.9, No.10, pp. 803-807.
- Townsend, B., G. Lachapelle, L.P. Fortes, T. Melgard, T. Morbech, J. Raquet (1999) New Concepts for a Carrier Phase Based GPS Positioning Using a National Reference Station Network. *Proceedings of the National Technical Meeting*, San Diego, USA, pp. 319-326.
- Tsujii, T., J. Wang, L., Dai C. Rizos, M. Harigae, T.T. Inagaki, T. Fujiwara, and T. Kato (2001) A Technique for Precise Positioning of High Altitude Platforms System (HAPS) Using a GPS Ground Reference Network, *Proceedings of ION GPS*, pp. 1017-1026.
- Wells, D., N. Beck, D. Delikaraoglou, A. Kleusberg, E. Krakiwsky, G. Lachapelle, R. Langley, M. Nakiboglu, K. P. Schwarz, J. Tranquilla, and P. Vanicek (1987) *Guide to GPS Positioning*, 2<sup>nd</sup> Ed., Canadian GPS Associates.
- Zhang, J. (1999) *Investigation into the Estimation of Residual Tropospheric Delays in a GPS Network*, MSc Thesis, University of Calgary.